Design of Efficient Acoustic Interfaces for Quantum Emitters in Diamond

by

Hamza Hussain Raniwala

B.S., California Institute of Technology (2020)

Submitted to the Department of Electrical Engineering and Computer Science
in partial fulfillment of the requirements for the degree of

Master of Science

at the

MASSACHUSETTS INSTITUTE OF TECHNOLOGY

September 2022

Author .....
Department of Electrical Engineering and Computer Science
August 26, 2022

Certified by .....
Dirk Robert Englund
Associate Professor of Electrical Engineering and Computer Science
Thesis Supervisor

Accepted by .....
Leslie A. Kolodziejski
Professor of Electrical Engineering and Computer Science
Chair, Department Committee on Graduate Students

Design of Efficient Acoustic Interfaces for Quantum Emitters in Diamond

by

Hamza Hussain Raniwala

Submitted to the Department of Electrical Engineering and Computer Science
on August 26, 2022, in partial fulfillment of the
requirements for the degree of
Master of Science

Abstract

Solid-state atomic defects–known as quantum emitters–in diamond are a valuable technology for quantum networking and computing due to their optically active transitions that interface on-chip systems with flying photons as well as their long-lived spin transitions that function as quantum memories. These advantages motivate the development of quantum emitter interfaces that can allow other technologies, such as superconducting circuits, nanomechanical resonators, and telecom optical cavities to interact with quantum emitters. Here, we propose two devices that allow these systems to efficiently interact via spin-phonon interactions with Group IV Silicon vacancy (SiV^-) centers in diamond. First, we design and simulate a spin-optomechanical interface with ultrasmall mechanical and optical mode volumes ($V_{\mathrm{mech}}/\Lambda_{\mathrm{p}}^3 \sim 10^{-5}$ and $V_{\mathrm{opt}}/\lambda^3 \sim 10^{-3}$, respectively) to interface SiV^- centers with a telecom optical mode for quantum networking. Next, we design and simulate an electromechanical transducer that generates tripartite strong coupling from a superconducting circuit and SiV^- electron spin to an intermediary phonon mode (with ultra-high cooperativities ($\sim 10^3$ and $\sim 10^2$, respectively). Finally, we discuss the deployment of these two devices in quantum information protocols: heralded entanglement using our spin-optomechanical interface; and superconducting circuit-to-spin quantum transduction, information storage, and networking using our spin-electromechanical transducer.

Thesis Supervisor: Dirk Robert Englund
Title: Associate Professor of Electrical Engineering and Computer Science

Acknowledgments

I would like to thank my thesis advisor, Professor Dirk Englund, for his encouragement, support, and useful discussions pertaining to this research. I would also like to thank Dr. Matthew Trusheim for his invaluable patience and guidance that helped shape the body of this work. Furthermore, I would like to thank my labmates Ian Christen and Kevin Chen for their advice and intellectual contributions to this work. Finally, I would like to thank my parents for their immeasurable support.

The devices discussed in Chapter 4 of this work are being made possible by numerous collaborators. The electromechanical transducer fabrication is supported by Sandia National Laboratories. Diamond microchiplets used for 4 Kelvin characterization of quantum emitters were fabricated by Kevin Chen and Linsen Li. Finally, silicon hard masks were fabricated by Applied Nanotools, Inc. and processed by Dr. Jawaher Almutlaq Linsen Li.

This master's thesis is supported by the National Defense Science and Engineering Fellowship, as well as funding from the MITRE Corporation and the Center for Ultracold Atoms.

Contents

List of Figures

List of Tables

Chapter 1

Introduction

Quantum information systems are evolving at an incredible pace. Today, several different modalities hold promise for quantum computing and networking, including superconducting systems, trapped ions and neutral atoms, atomic defects and quantum dots in solid state, and flying photons. It is becoming increasingly clear that each "quantum modality" holds its own set of advantages and disadvantages in areas such as computing speeds, gate fidelities, coherence times, and networking capabilities. As such, there is great interest in the quantum information science community in interfacing different quantum modalities in hybrid quantum systems.

In this introduction, we will motivate the use of one bosonic carrier of quantum information–the acoustic phonon–as a method of transducing information from one quantum modality to another. In 1.1, we will explain the fundamentals of acoustic phonons including a direct analog to the math that describes photonic modes. In 1.2, we will then preface the methods by which phonons interact with various qubit modalities. Finally, in 1.3, we will outline the devices researched in this thesis, including their physical anatomy and operational protocols as intended for use in quantum systems.

1.1 Quantum information processing with acoustics

Acoustic phonons have been coined the "universal transducers" of quantum information for their ability to interact with a multitude of disparate quantum systems [135]. Phonons are the mechanical excitations of a system, analogous to photons which are the electromagnetic excitations of a medium. The word "phonon" may refer to the vibrational modes of an atomic or atom-like system, or it may refer to the resonant vibrations of a mechanical resonator or waveguide. In this paper, we will focus on the GHz-frequency phonons of mechanical resonators, which can interact with microwave superconducting circuits, atomic spin defects, and photonic crystals, among other systems.

Acoustic phonons can be understood by analogy to photons. The photonic modes of a system are determined by solving Maxwell's equations in a medium. By combining Faraday's law and Ampere's law, one can write an eigenmode equation for the electric field in a closed system as

$$\omega^2 \mathbf{H} = \boldsymbol{\nabla} \times \left(\frac{1}{\mu \bar{\bar{\epsilon}}} \boldsymbol{\nabla} \times \mathbf{H} \right), \tag{1.1}$$

where $\mathbf{H}$ is the eigenmode magnetic field and $\bar{\bar{\epsilon}}$ is the permittivity tensor of the system. Similarly, one can write an eigenmode equation for phonons in an elastic medium using the stress-strain relation and Newton's second law for a point in an elastic medium, respectively:

$$T_{ij} = c_{ijkl} S_{kl} = \frac{c_{ijkl}}{2} \left(\partial_k Q_l + \partial_l Q_k \right), \tag{1.2}$$

$$\rho \partial_t^2 Q_i = \partial_j T_{ji}. \tag{1.3}$$

Combining these equations gives an eigenvalue problem for the displacement eigenmode $\mathbf{Q}$ of an elastic medium,

$$\rho \partial_t^2 Q_i = \partial_j \left[\frac{c_{ijkl}}{2} \left(\partial_k Q_l + \partial_l Q_k \right) \right]. \tag{1.4}$$

A few features characterize the usefulness of phonons in quantum information processing. Firstly, phonons feature a dispersion ratio like photons, and can therefore be stationary or flying bosonic carriers of quantum signals. Secondly, phonons do not radiate into vacuum unlike photons, instead only dissipating into the bulk of a medium in which they are housed via coupling to an environmental phonon bath. Hence, at cryogenic temperatures where the occupancy of GHz phonons is low, and with appropriate bandstructure engineering, phonons are a long-lived carrier of quantum information on chip. Finally, as we will explain in the next section, phonons can nearly-universally interact with other qubits.

1.2 Interaction of phonons with other qubits

Because vibrations are essentially universally present in physical systems, the quantized vibrations of phonons can be used to interact with qubit modalities across the range of current quantum computing hardware. For instructive purposes, we delineate these interactions below for systems such as trapped ions, neutral atoms, flying photons, superconducting circuits, and atom-like emitters in solid state. In this thesis, we will proceed to focus on phonon interactions with optical cavities, superconducting circuits, and quantum emitters in dielectric and semiconducting media.

1.2.1 Trapped Ion- and Neutral Atom-Phonon Interactions

In trapped ion and neutral atom quantum systems, single ions or atoms are held at specified locations in vacuum using oscillating electric potentials [32] or optical tweezers [11, 65, 154]. As such, these individual atoms are relatively well-isolated from their surroundings, leading to long lifetime quantum bits. However, this isolation also makes it difficult to communicate between qubits through multi-qubit gates, which are essential for quantum information processing.

Phonons–in this case, the vibrational states of each ion ensemble–resolve this issue by allowing communication between these ions or atoms, as depicted in Fig. 1-1. The multi-qubit gates that result by coupling phonons across multiple ions or atoms to

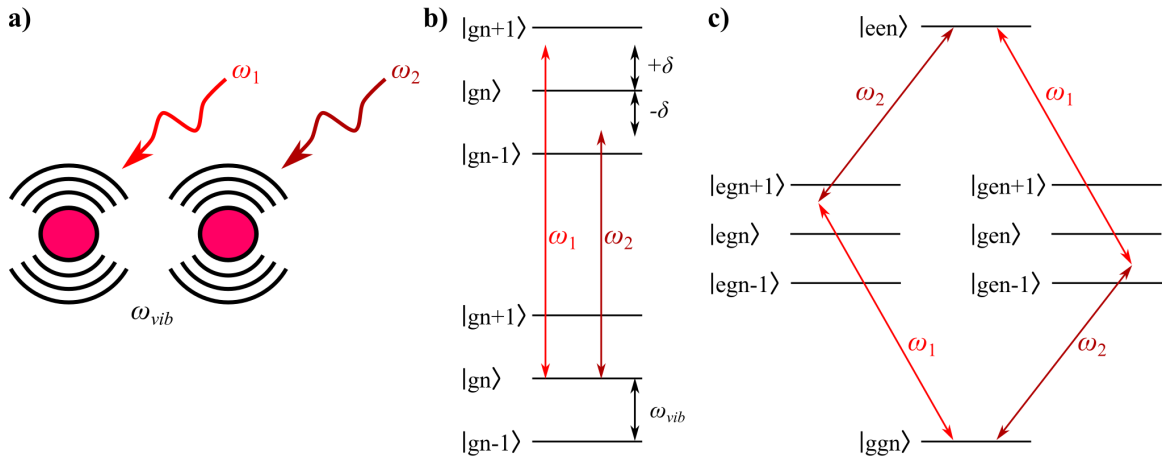

Figure 1-1: Molmer-Sorensen gate between two atoms [141]. (a) Illustration of laser addressing of two atoms at laser frequencies ω_1 and ω_2. (b) Energy level diagram of the atom's internal excitation states as well as the phonon number occupying the ensemble vibrational state. (c) Intefering transition paths utilizing the ensemble vibrational state.

their internal excitation states are known as Molmer-Sorensen gates [141]. These are described by the Hamiltonian

$$H = \hbar\omega_{vib}\left(\hat{a}^\dagger\hat{a} + \frac{1}{2}\right) + \hbar\omega_{eg}\sum_i \frac{\hat{\sigma}_{z_i}}{2} + \sum_i \frac{\hbar\Omega_i}{2}\left(\hat{\sigma}_+ e^{i\left(\eta_i\left(\hat{a}+\hat{a}^\dagger\right)+\omega_i t\right)} + \text{H.c.}\right), \quad (1.5)$$

where ω_{vib} is the vibrational frequency of the phonon, ω_{eg} is the internal excitation frequency of each atom or ion, ω_i and Ω_i are the frequency and Rabi frequency of the laser addressing the ith atom or ion, and η_i is the ith atom or ion's excitational-vibrational state interaction strength. This phonon-atom interaction has been used to develop a variety of multi-qubit operations in trapped ion [84, 54, 1, 137] and neutral atom [107, 98] quantum systems. The use of phonons as an information carrier in trapped ion and atom quantum gates is instructive as phononic architectures and algorithms for other systems develop.

1.2.2 Quantum Optomechanical Interactions

The interaction of light with solid matter via radiation pressure forces is a remarkable phenomenon whose discovery dates back to the 17th century [68, 12]. In recent years,

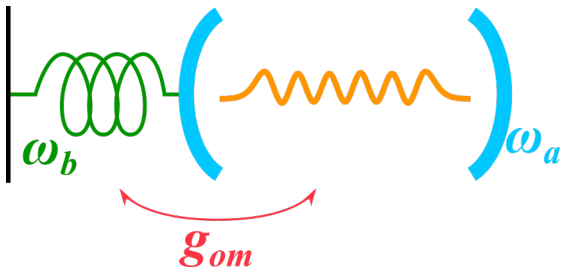

Figure 1-2: Canonical optomechanical interaction picture. An optical cavity formed by two mirrors is coupled to a spring via one moving mirror. The pressure of photons impinging on the cavity induces vibrations in the spring, causing the resonant optical cavity frequency to change.

these interactions have been pushed to the single quantum limit of cavity optomechanics. In this regime, single phonons perturb optical modes of micro- or nano-scale devices, resulting in a coupling between mechanical and optical displacement fields. The Hamiltonian describing this interaction, the canonical example of which is an optical cavity coupled to a spring (Fig. 1-2), can generally be written as

$$\hat{H} = \hbar\omega_a \hat{a}^\dagger \hat{a} + \hbar\omega_b \hat{b}^\dagger \hat{b} + \hbar g \alpha \left(\hat{a}^\dagger + \hat{a}\right)\left(\hat{b}^\dagger + \hat{b}\right), \tag{1.6}$$

where $\hat{a}$ and $\hat{b}$ are the creation and annihilation operators of the photonic and phononic modes of a closed system, respectively, and ω_a and ω_b are the respective resonant frequencies of these modes. The coefficient g represents the single-photon coupling between modes, governed by the refractive index change in a material due to phonon-induced strain (photoelastic effect) and the change in boundary conditions of an optical structure due to phonon-induced displacement (moving boundary effect) [42]. Finally, α reprsents the average photon number in the optical cavity. This description generalizes the canonical example to optomechanical structures with arbitrary geometry.

Cavity optomechanics has been proposed and implemented in a variety of applications in quantum information science, including cat state generation [4], sensing [57, 86], and energy transduction between microwave photons and optical photons [105, 161, 22]. We will describe the use of cavity optomechanics–a particular implementation of photon-phonon interactions in resonant structures–for quantum net-

working in Chapter 2 of this work.

1.2.3 Superconducting Circuit-Phonon Interactions

The coupling between microwave electronic circuits and mechanical waves is an old phenomenon dating back to the development of surface acoustic waves [126] in piezoelectric materials [25, 164]. With the development of superconducting microwave circuits, including nonlinear circuits used in superconducting qubits, this coupling between electric fields and acoustic modes has been pushed to the limit of a single superconducting circuit excitation driving or hybridizing with mechanical modes of on-chip systems [112, 96]. In the example of microwave electromagnetic resonators coupled to mechanical oscillators, the circuit-phonon interaction picture is described by the same Hamiltonian as the cavity optomechanical picture. In the case of a superconducting two-level system coupled to a mechanical oscillator, the Jaynes-Cummings Hamiltonian,

$$\hat{H}_{JC} = g\left(\sigma_+\hat{b} + \sigma_-\hat{b}^\dagger\right), \tag{1.7}$$

more accurately describes the interaction picture. Here, $\sigma_\pm$ are the ladder operators of a two-level system, and g describes the coupling between electric and mechanical modes.

Superconducting qubit-phonon interactions have been utilized in a multitude of demonstrations, including ground state cooling and single quantum control of a phonon mode [112], mechanical resonator tomography and entanglement [158], and quantum computing with mechanical memories [114]. They have found applications in bosonic quantum information schemes and proposals [55, 163] as well as the microwave-to-optical transduction efforts cited above. In this work, we will focus on the use of superconducting qubit-phonon transduction as an intermediary step towards spin-phonon coupling.

1.2.4 Phonon-Spin Interactions in Quantum Emitters

Typically, phonon interactions with solid-state quantum emitters are an unavoidable dephasing mechanism that decreases the lifetime of solid-state quantum bits [35, 46, 118]. Phonon excitations result in fluctuations and strains in the crystal environment surrounding emitters such as nitrogen vacancy (NV^-) centers, Group IV color centers, and other emitters in diamond, silicon, etc. These fluctuations change the interatomic distances between the atoms defining emitters, coupling emitters to the phonon bath and leading to decoherence.

However, if a particular mechanical mode is engineered to strongly interact with the spin degree of freedom of a quantum emitter, then undesirable phonon coupling can become an advantage that can be leveraged in quantum information protocols. Quantum emitters interact with mechanical modes via spin-strain coupling, in which the strain generated by mechanical displacement strongly interacts with the spin energy levels of quantum emitters via their spin-strain susceptibilities. The interaction Hamiltonian that describes this picture is the Jaynes-Cummings Hamiltonian between a true two-level system and a bosonic mode, shown above [111].

Mechanical interfaces with spins have been used for quantum control of diamond emitters [49, 50, 95, 94] and probing the physical properties of quantum emitters in probing experiments [102], but the general area of research is still rapidly growing. In this work, we will describe one possible implementation of a spin-mechanical interface in the form of a nanoscale mechanical resonator embedded with a quantum emitter.

1.3 Devices Discussed in this Work

In this work, we focus on implementing three of the above phenomena in two different devices and protocols. In Chapter 2, we discuss the implementation of spin-mechanical coupling in and optomechanical coupling in a spin-optomechanical interface. We will describe the concept, design, and simulation of this device and outline its use in quantum networking protocols.

In Chapter 3, we describe a spin-electromechanical transducer that implements

spin-phonon and superconducting circuit-phonon coupling in a direct quantum transduction protocol. We propose the use of this device and protocol in a quantum memory register and in an optical interface with integrated node memory for superconducting quantum processors.

Chapter 2

Spin-Optomechanical Interfaces

We propose a coherent mechanical interface between defect centers in diamond and telecom optical modes. Combining recent developments in spin-mechanical devices and optomechanical crystals, we introduce a 1D diamond nanobeam with embedded mechanical and electric field concentrator with mechanical and optical mode volumes $V_{\mathrm{mech}}/\Lambda_{\mathrm{p}}^3 \sim 10^{-5}$ and $V_{\mathrm{opt}}/\lambda^3 \sim 10^{-3}$, respectively. By placing a Group IV vacancy in the concentrator we demonstrate exquisitely high spin-mechanical coupling rates approaching 40 MHz, while retaining high acousto-optical couplings. We theoretically show that such a device, used in an entanglement heralding scheme, can provide high-fidelity Bell pairs between quantum repeaters. Using the mechanical interface as an intermediary between the optical and spin subsystems, we are able to directly use telecom optics, bypassing the native wavelength requirements of the spin. As the spin is never optically excited or addressed, we do not suffer from spectral diffusion and can operate at higher temperatures (up to 40 K), limited only by thermal losses. We estimate that based on these metrics, optomechanical devices with high spin-mechanical coupling will be a useful architecture for near-term quantum repeaters.

2.1 Background and Motivation

The interaction of light with solid matter via radiation pressure forces is a remarkable phenomenon whose discovery dates back to the 17th century [68, 12]. In re-

cent decades, progress on understanding and engineering this light-matter interaction has produced groundbreaking experiments in cavity optomechanics, including laser feedback cooling [10], parametric light-matter processes in kg-scale [34] and picogram-scale [42, 41, 29] optomechanical systems, and laser cooling of mechanical modes to their ground state [156, 29]. These quantum optics-like experiments have paved the way for optomechanical devices to be used in quantum transduction [150, 105, 45, 60, 161] and entanglement [129, 165].

Solid-state vacancy-defect complexes are a developing technology that is complementary to cavity optomechanics. These complexes are atomic defects in dielectric media, such as diamond, can be intentionally implanted into a dielectric lattice [30, 56]. The free electron spin or nuclear spin of the resulting vacancy centers in the lattice can be coherently controlled as solid state quantum bits [30]. Additionally, research efforts demonstrating acoustic control of spin centers has opened the door to multi-modality quantum systems, such as spin-optomechanical interfaces [131, 95, 136]. These complex coupled systems can potentially allow for dark-state operation of spin centers, optical-to-spin quantum transduction, and new architectures for quantum repeaters in a quantum network.

Here, we propose an ultra-small mode volume spin-optomechanical interface in diamond for strong coupling between the mechanical mode of an optomechanical resonator and an embedded group IV defect-vacancy complex. Our device introduces an optical resonance to previous ultra-small mechanical cavities for spin interfacing [134], while also improving previous mechanical mode volumes. We show that this device can be used to interact with a vacancy without optically exciting the spin at its native wavelength, operating at the cavity wavelength instead through a optomechanically mediated interaction. Hence, we explore the use of this spin-optomechanical interface in entanglement protocols in a quantum network.

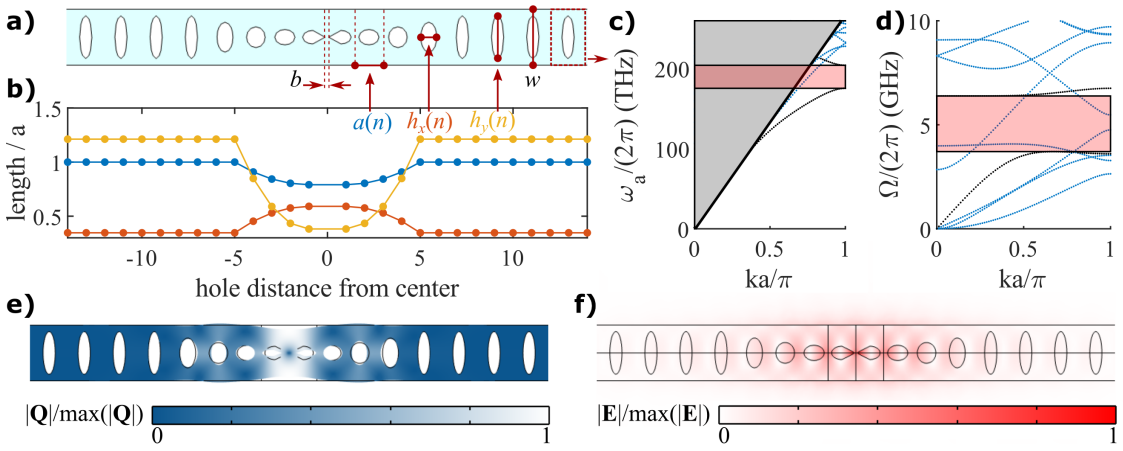

Figure 2-1: Diamond 1D nanobeam OMC with embedded concentrator, drawing from previous examples in silicon [42, 29] and diamond [23, 24, 95] as well as ultrasmall mode volume photonic and phononic crystals [31, 134]. (a) Diagram of the nanobeam photonic crystal. Free parameters include taper width b; unit cell period as a function of cell number n, $a(n)$; unit ellipse width $h_x(n)$ and height $h_y(n)$; and beam width w alongside beam thickness t. (b) Plot of quadratically varying $a(n)$, $h_x(n)$, and $h_y(n)$ on either side of the beam center. This characterizes the cavity with parameters $(a, a_d, h_x, h_{x_d}, h_y, h_{y_d}, w, t, b) = (577.5, 456.75, 200, 341.25, 700, 220.5, 913.5, 250, 60)$ [nm]. (c) optical and (d) mechanical bandstructure for the mirror unit cell of the cavity, providing a 28.7 THz bandgap around and a 2.41 GHz mechanical bandgap. (e) mechanical displacement and (f) electric field norm profiles of the 5.34 GHz mechanical mode and 197.5 THz optical mode of the cavity.

2.2 Theory of Spin-Optomechanical Coupling

A spin-optomechanical interface accomplishes two effects. First, it couples the photonic mode of a photonic crystal cavity to the phononic modes of the crystal in a pump-driven interaction. Next, it couples the spin transition of a solid-state color center to the same phononic modes. Let us denote the operating frequency of the photonic mode as ω_a, the spin transition frequency as ω_σ, and the pump beam frequency as ω_p. Without loss of generality, we assume only a single phononic mode Ω is nearly resonant with the pump detuning, such that $\Delta = \omega_\mathrm{p} - \omega_\mathrm{a} \approx \Omega$. Then we can simplify the system Hamiltonian by considering only a single phononic mode. In this picture, the unperturbed Hamiltonian $\hat{H}_0$ can be written as

$$\hat{H}_0 = \hbar\omega_\mathrm{a}\hat{a}^\dagger\hat{a} + \hbar\Omega\hat{b}^\dagger\hat{b} + \frac{\hbar\omega_\sigma}{2}\hat{\sigma}_\mathrm{z}. \tag{2.1}$$

Here, $\hat{a}^\dagger, \hat{a}$ and $\hat{b}^\dagger, \hat{b}$ are the ladder operators of the photonic and phononic modes, respectively, and $\hat{\sigma}_j$ is the spin qubit's j-Pauli operator.

Additionally, the parametric coupling between the mechanical and optical resonators takes the form $\hat{H}_{\rm om} = \hbar g_{\rm om} \hat{a}^\dagger \hat{a} \left(\hat{b}^\dagger + \hat{b} \right)$, i.e., an optical resonance shift dependent on the position of the mechanical resonator. To linearize this interaction, we drive the optical cavity with a pump $\omega_{\rm p} = \omega_{\rm a} + \Delta$. By applying the rotating wave approximation and rewriting the photon ladder operators around a mean population $\overline{a}$ as $\hat{a} \to \overline{a} + \hat{a}$, we arrive at the typical optomechanical interaction Hamiltonian in the blue-detuned regime,

$$\hat{H}_{\rm om} = \hbar g_{\rm om} \overline{a} \left(\hat{a}^\dagger \hat{b}^\dagger + \hat{a} \hat{b} \right). \tag{2.2}$$

Next we consider the spin-mechanical interaction. In a spin-strain interaction picture, this is generated by deformation-induced strain causing a level shift in the spin qubit transition energy. This level shift is described by the spin-mechanical interaction Hamiltonian

$$\hat{H}_{\rm sm} = \hbar g_{\rm sm} \left(\hat{\sigma}_+ \hat{b} + \hat{\sigma}_- \hat{b}^\dagger \right). \tag{2.3}$$

Here, $g_{\rm sm}$ is the strain-induced coupling by the zero-point fluctuation of the mechanical resonator and $\hat{\sigma_\pm} = \frac{1}{\sqrt{2}} (\sigma_{\rm x} \pm i \sigma_{\rm y})$. As such, any phonon excitation will induce zero-point coupling between the spin qubit and resonator phonon and vice versa. Then the full system Hamiltonian is

$$\hat{H} = \hat{H}_0 + \hat{H}_{\rm om} + \hat{H}_{\rm sm}. \tag{2.4}$$

To devise an efficient spin-optomechanical interface, we maximize $g_{\rm sm}$ and mechanical quality factor $Q_{\rm mech}$ while maintaining high $g_{\rm om}$. We review a device design that achieves parameters below.

2.3 Device Design and Simulations

2.3.1 Design Summary

At the core of our proposal is a strain concentrator embedded in a one-dimensional optomechanical crystal (1D OMC) (Fig.2-1a). The 1D OMC consists of a nanobeam with periodically etched ellipses that are adiabatically morphed into a defect cell. We then modify the central unit cells by tapering to a width b using a hyperbolic curve. By COMSOL finite element method (FEM) simulation, we predict an optical mode of frequency $\omega_{\mathrm{a}}/(2\pi) \approx 197.5$ THz and $Q_{\mathrm{opt}} \approx 3.6 \times 10^4$ (Fig. 2-1(f)), which lies in the mirror cells' 28.7 THz optical bandgap from 175.28 THz to 203.98 THz (Fig. 2-1(b)). We predict an acoustic resonance around $\Omega = 5.34$ GHz (Fig. 2-1(e)) between the 2.41 GHz acoustic bandgap from 4.96 GHz to 7.37 GHz (Fig. 2-1(d)). In optomechanical crystals, single photon-to-single phonon coupling between a photonic cavity mode and a mechanical resonant mode arises due to the cavity frequency shift induced by the acoustic displacement profile, normalized to the zero-point fluctuation [62, 132]

$$g_{\mathrm{om}} = \frac{\partial \omega}{\partial \mathbf{q}} x_{\mathrm{zpf}}. \tag{2.5}$$

Note here that the cavity zero-point fluctuation can be approximated using the resonator's effective mass m_{eff} as

$$x_{\mathrm{zpf}} = \sqrt{\frac{\hbar}{2 m_{\mathrm{eff}} \Omega}}, m_{\mathrm{eff}} = \frac{\int_V d\mathbf{r} \mathbf{Q}^*(\mathbf{r}) \rho(\mathbf{r}) \mathbf{Q}(\mathbf{r})}{\max(|\mathbf{Q}(\mathbf{r})|^2)}. \tag{2.6}$$

Here, $\mathbf{Q}(\mathbf{r})$ is the mechanical displacement profile and $\rho(\mathbf{r})$ is the density profile (either ρ_{diamond} or 0).

This consists of two explored effects: the moving boundary effect (shift due to moving vacuum-dielectric boundary conditions resulting from mechanical displacement) and the photoelastic effect (frequency shift due to the sum of strain-induced local refractive index changes in the crystal). The vacuum moving boundary coupling g_{mb} can be written as [42, 62]

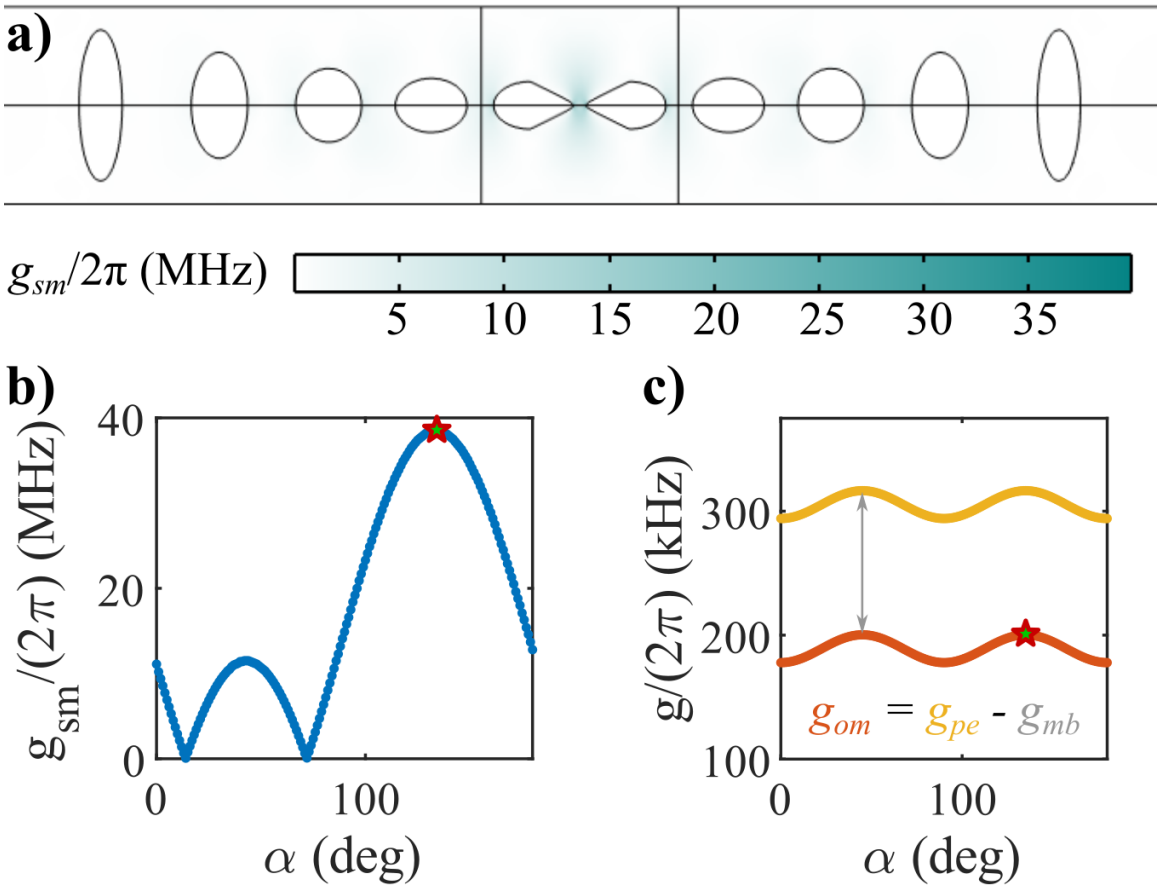

Figure 2-2: Spin-mechanical coupling profile in the nanobeam. (a) xy slice of spin-mechanical coupling. (b) g_{sm} as a function of Euler angle α where the preferred crystal orientation is starred. (c) g_{om} as a function of α where the preferred crystal orientation is starred.

$$\frac{g_{\mathrm{mb}}}{x_{\mathrm{zpf}}} = -\frac{\omega_{\mathrm{a}}}{2}\frac{\int_S (\mathbf{Q}(\mathbf{r})\cdot\mathbf{n})\left(\Delta\boldsymbol{\varepsilon}\left|e^{\parallel}\right|^2 - \Delta(\boldsymbol{\epsilon}^{-1})\left|\bar{d}^{\perp}\right|^2\right)dA}{\max(|\mathbf{Q}|)\int \boldsymbol{\varepsilon}(\mathbf{r})|\mathbf{e}(\mathbf{r})|^2 d^3\mathbf{r}}. \tag{2.7}$$

The photoelastic coupling g_{pe} can be expressed as [132]

$$\frac{g_{\mathrm{pe}}}{x_{\mathrm{zpf}}} = -\frac{\omega_{\mathrm{a}}}{2}\frac{\int_V \mathbf{e}\cdot\boldsymbol{\delta\epsilon}\cdot\mathbf{e}d^3\mathbf{r}}{\max(|\mathbf{Q}|)\int_V \boldsymbol{\epsilon}(\mathbf{r})|\mathbf{e}(\mathbf{r})|^2 d^3\mathbf{r}}. \tag{2.8}$$

Here, $\mathbf{e}(\mathbf{r})$ is the cavity electric field profile. Expanding the integrand in the

numerator of (2.8), we can write that as [28]

$$\mathbf{e}\cdot\boldsymbol{\delta\epsilon}\cdot\mathbf{e} = \mathbf{e}\cdot\left(\varepsilon^2\frac{\mathbf{pS}}{\varepsilon_0}\right)\cdot\overline{e} \tag{2.9}$$

$$= \mathbf{e}\cdot\left(\epsilon_0 n^4 p_{ijkl}(\alpha)S_{kl}\right)\cdot\mathbf{e}. \tag{2.10}$$

Here, we note that p_{ijkl} is a function of the diamond crystallographic orientation relative to the device geometry, which runs along $\hat{x}$ in the xy-plane. Parametrized by α (the angle between the [100] crystal axis and the longitudinal axis of the nanobeam), the rotated p_{ijkl} is given by [28]

$$p_{ijkl}(\alpha) = R(0,\alpha)_{iq}R(0,\alpha)_{jr}R(0,\alpha)_{ks}R(0,\alpha)_{lt}p_{qrst}, \tag{2.11}$$

where

$$R(\theta,\phi) = \begin{bmatrix} \cos\phi & \sin\phi & 0 \\ -\cos\theta\sin\phi & \cos\theta\cos\phi & -\sin\theta \\ -\sin\theta\sin\phi & \sin\theta\cos\phi & \cos\phi \end{bmatrix}. \tag{2.12}$$

In our simulations, we used $(p_{11}, p_{12}, p_{44}) = (-0.25, 0.043, -0.172)$ [83]. As shown in Fig. 2-2(c), we find that the anisotropic nature of the photoelastic tensor yields a variation in g_{PE} of about 7% with α, maxing out at $g_{\mathrm{pe}}/(2\pi) = 316$ kHz for $\alpha = \pi/4, 3\pi/4$ rad. Summing with $g_{\mathrm{mb}}/(2\pi) \approx -116$ kHz, we find a total vacuum coupling rate $g_{\mathrm{om}}/(2\pi) = 200$ kHz.

The ultimate spin-phonon coupling is a function of the strain-induced g_{sm} profile (Fig. 2-2(a)). We use g_{sm} to indicate the effective spin-orbital coupling resulting from a change in SiV^- transition frequency as a function of displacement-induced strain [111],

$$g_{\mathrm{sm}}(\mathbf{r}) = d\frac{(\epsilon_{xx}(\mathbf{r}) - \epsilon_{yy}(\mathbf{r}))}{max(|\mathbf{Q}|)}x_{\mathrm{zpf}}. \tag{2.13}$$

Here, $d \approx 1$ PHz/strain is the strain-susceptibility parameter describing the mixing of SiV^- orbitals, and ϵ_{xx} and ϵ_{yy} describe the strain tensor components of the SiV^-. [56, 102, 111]. The SiV^- $\{x, y, z\}$-axis is offset from the diamond $\{x_0, y_0, z_0\}$ axis by polar angle $\theta = \arcsin\sqrt{2/3}$ rad and azimuthal angle $\phi = \pi/4$ rad [56]. So, to get ϵ_{xx} and

ϵ_{yy} of the SiV^- from crystal tensor components, we apply the rotation operation

$$\epsilon_{ijkl} = R(\theta,\phi)_{iq}R(\theta,\phi)_{jr}R(\theta,\phi)_{ks}R(\theta,\phi)_{lt}\epsilon_{0qrst}(\alpha). \tag{2.14}$$

2.3.2 FEM Simulations of Optomechanical Crystal

The diamond optomechanical crystal was designed and simulated using the finite element method (FEM) in COMSOL Multiphysics 5.4. Simulations began with the analysis of a nanobeam unit cell. Mechanically, we simulate the eigenmodes of the unit cell with Floquet boundary condition defined by

$$\mathbf{Q}(x) = \mathbf{Q}(x)e^{ik_x x}, \tag{2.15}$$

where $\mathbf{Q}(x)$ is the mechanical displacement profile at a given x and $k_x \in \{0, \frac{\pi}{a}\}$. Similarly, the simulate the electromagnetic eigenmodes using the Floquet boundary equation

$$\mathbf{e}(x) = \mathbf{e}(x)e^{ik_x x}, \tag{2.16}$$

where $\mathbf{e}(x)$ is the electric field at a given x. Bandstructures for these simulations are shown in Fig. 2-1c-d in the main text. After locating optical and mechanical bandgaps, the unit cells were varied by changing unit cell parameters $\{a, h_x, h_y\}$ to their "defect unit cell" values of $\{a_d, h_{x_d}, h_{y_d}\}$ to re-simulate mechanical and optical bandstructures at the Γ point (for the mechanical breathing mode) and the X point (for the electromagnetic confined mode). Finally, the central two unit cells were modified to add the concentrating taper. A rectangular section of length $2a_d$ and height $2h_{y_d}$ was subtracted from the center of the crystal, connecting the two central ellipses. Next, the central taper was filled according to the intersection of the rectangular top and bottom lines with two hyperbolic curves following the (right hand side) equation (mirrored on the left-hand side)

$$x(y) = \frac{c_1}{c_2}\sqrt{c_2^2 + y^2}, c_1 = \frac{b}{2}, c_2 = \frac{bh_{y_d}}{2a_d}. \tag{2.17}$$

This resulted in the geometry shown in Fig. 2-1a. The completed nanostructure was then simulated using the Solid Mechanics and Electromagnetic Waves, Frequency Domain (ewfd) physics modules and Eigenmode solver in COMSOL. The introduction of a central taper necessitated further modifying of the defect unit cell parameters, so $\{a_d, h_{x_d}.h_{y_d}\}$ were varied slightly to induce optical and acoustic modes that were near the center of the optical and acoustic band gaps, respectively, of the mirror unit cells.

The mechanical (clamping) and optical Qs (Fig. 2-4) were calculated as a function of central bridge width b for the high-g_{om}-and-g_{sm} breathing mode (Fig. 2-1).

From these simulations, we find that Q_{mech} will likely not limit the overall mechanical quality factor. Q_{opt} can likely be tuned for each b according to radiation cancellation [31], but for our heralded entanglement protocol, Q_{opt} primarily dictates the detection rate of a photon-phonon pair generation event. This leakage rate should be greater than the rate of phonon decay (i.e. $\kappa_{opt} \equiv \frac{\omega_a}{Q_{opt}} > \frac{\Omega}{Q_{mech}} \equiv \kappa_{mech}$) to ensure the acoustic phonon is not lost by the time the accompanying photon is detected. Hence, it is not important (nor necessarily favorable) for us to optimize Q_{opt} in this paper.

2.3.3 Calculation of Spin-Phonon Coupling

Spin-phonon coupling was calculated using FEM simulations in COMSOL. The Euler angle α representing the in-plane rotation of the diamond crystal orientation relative to the x-axis of the nanobeam was swept as $0° \leq \alpha \leq 180°$. For the subsequent calculations of g_{sm}, we assume that the diamond crystal z-axis is oriented along the high-symmetry axis of the defect [111], x along $[\bar{1}\bar{1}2]$, and y along $[\bar{1}10]$, such that the SiV^- experiences [111]

$$\epsilon_{xx} - \epsilon_{yy} = \frac{1}{3}\Big(- \epsilon_{11} - \epsilon_{22} + 2\epsilon_{33} + 2(\epsilon_{12} + \epsilon_{21}) - (\epsilon_{13} - \epsilon_{31}) - (\epsilon_{23} + \epsilon_{32})\Big). \quad (2.18)$$

The g_{sm} for each b was calculated by taking the coupling at the middle of the right-edge of the central taper at ten slices from $z = t_d$ to $z = 0$. This was done

to reduce numerical noise in the FEM simulation that resulted from extremely small elements experiencing dramatic deformation without increasing the mesh density to untenable levels.

We note here that there is a distinction between the strain-orbital coupling $d = \epsilon_{xx} - \epsilon_{yy}$ and the spin-strain coupling g_{sm} dependent on the applied magnetic field. However, based on Appendix A in [123], the spin-strain coupling can become comparable to the strain-orbit coupling when the vector magnetic fields reach values of ~ 2 T. This is achievable with commercially available vector magnets that can be added to cryostats. The plot of increasing magnetic field–including the required longitudinal and transverse components to maintain a spin transition frequency of 5.34 GHz, are shown in Fig. 2-11.

2.3.4 Spin-Phonon and Optomechanical Coupling Trends

Note that g_{sm} varies by location in the cavity; as such, we have plotted the location of maximum g_{sm} in our cavity for each mechanical mode in Fig. 2-2(b). We find that g_{sm} is maximized at an angle $\alpha = 3\pi/4$ rad, with a maximum value $g_{\mathrm{sm}}/(2\pi) \approx 41$ MHz, owing to phase matching between $\epsilon_{0_{yy}}$ and $(\epsilon_{0_{xy}} + \epsilon_{0_{yx}})$ terms (see Appendix B).

We note here the impact of changing b: as b is decreased, the optical and acoustic mode profiles become more strongly influenced by the concentrator, whereas for larger b the modes are spread across the neighboring defect cells. Mechanically, a smaller b (Fig. 2-3(a) left) can be interpreted as a weakening spring constant in the central bridge between the masses of the walls surrounding the bridge. Hence, as b decreases, Ω decreases and x_{zpf} increases (Fig. 2-3(b)-(c)). For a decreasing "spring constant" and increasing x_{zpf}, we expect the strain in the central cavity to increase, boosting g_{sm}. Indeed, we observe this effect in simulation (Fig. 2-3(d)).

Another interpretation of the increase in g_{sm} with decreasing b is that of mechanical mode volume [134]: as b decreases, the strain energy density of the mechanical mode becomes more highly concentrated in the taper, thereby decreasing the mechanical mode volume V_{mech} dramatically. We estimate through FEM that $V_{\mathrm{mech}}/\Lambda_{\mathrm{p}}^3$

and $V_{\mathrm{mech}}/\Lambda_{\mathrm{s}}^3$ drop from $\sim 10^{-4}$ and $\sim 10^{-3}$, respectively, to $\sim 10^{-6}$ and $\sim 10^{-5}$, respectively, as b decreases from 100 nm to 20 nm (Fig. 2-3d). Here, Λ_{p} and Λ_{s} are the longitudinal and shear wave velocities in bulk diamond [134]. As V_{mech} decreases, g_{sm} increases, which also increases the "mechanical Purcell enhancement." $V_{\mathrm{opt}}/\lambda^3$ or $V_{\mathrm{opt}}/(\lambda/n)^3$ similarly decrease from $\sim 10^{-2}$ and $\sim 10^{-1}$, respectively, to $\sim 10^{-4}$ and $\sim 10^{-3}$, respectively, with decreasing b (Fig. 2-3e)–a beneficial effect for simultaneously concentrating the cavity mechanical and optical modes. Here, λ is the free space cavity wavelength, and n is the refractive index of diamond.

With decreasing optical mode volume, we expect the cavity optical energy density to be more confined in the concentrator for decreasing b [31], which leads to two potentially competing effects. The first is that any photoelastic- or moving boundary-based contributions to g_{om} within the concentrator will be magnified; but the second is that the effective volume of dielectric over which these magnified effects manifest decreases. We see that, based on these competing effects, a bridge width of $b = 60$ nm optimizes g_{om} for our design (Fig. 2-3(g)). Making b as small as possible optimizes g_{sm} (Fig. 2-3f), but we assume a lower bound of $b = 60$ nm for ease of fabrication. We observe here that placing the emitters as close to the edge of the taper as possible will maximize g_{sm}. This proximity to dielectric walls normally imposes a limitation on the optical coherence of an emitter, but because our scheme interacts with the emitter non-optically, we can circumvent this obstacle.

In Fig. 2-7, we test the idea that the coupling mode of interest is sufficiently spaced from other mechanical modes in frequency. By plotting the profiles of all modes of $g_{\mathrm{sm}} > 10$ MHz within 2 GHz of $\Omega = 5.34$ GHz, we find that these "high g_{sm}" modes are at least 400 MHz apart from the mode of interest and feature at most half as high $\max(g_{\mathrm{sm}})$ over the mode profile. Parasitic spin-mechanical coupling to these modes can be modeled as a loss channel of the primary mechanical mode alongside the intrinsic mechanical loss κ, with loss to mode i given by

$$\kappa_i \approx g_{\mathrm{sm}_i} \left(\frac{g_{\mathrm{sm}_i}^2}{g_{\mathrm{sm}_i}^2 + \Delta_i^2} \right)^2 \tag{2.19}$$

From the closest mode at 4.91 GHz, which has a similar profile to the mode of interest, we find that $\max_i\{\kappa_i(2\pi)\} \approx 50$ kHz. This corresponds to an effective quality factor $Q_i \approx 3 \times 10^6$. From FEM simulations, we find that mechanical quality factors are higher than this parasitic coupling-induced Q (see Appendix A), indicating that external resonances will limit the cavity phonon lifetime. However, this is only true when our quantum emitter is implanted precisely in the concentrated coupling region of the parasitic mode, which from Fig. 2-7 is visually more compact than the mode of interest. If our emitters are implanted at a distance from the dielectric boundary, then these parasitic loss channels become weaker. We also note that, in the event that multiple emitters are implanted in the cavity, one can tune a single emitter into resonance by modifying the external magnetic field to vary the Zeeman splitting of each emitter. This can also allow for addressing multiple emitters individually via the same optomechanical cavity.

Another limiting loss channel is thermal losses, which can be characterized as phonon-phonon interactions using the Akhiezer or Landau-Rumer loss models [2, 82, 159, 146]. At higher temperatures, these losses will dominate due to the greater presence of thermal phonons in the cavity. At lower temperatures, other losses–including clamping losses, parasitic coupling, and material losses–will likely dominate.

2.4 Remote Entangling Protocols

The controlled opto-mechanical two-mode squeezing represented by Eq. 2.2 enables us to herald the creation of single phonons in the mechanical resonator. Such excitations can then be deterministically transferred to the spin for long term storage. Crucially, if we employ the Duan, Lukin, Cirac, and Zoller's [39, 76] entangling protocol, we can herald an entangled $|01\rangle \pm |10\rangle$ state in two remote mechanical resonators. Each of the two mechanical resonators can then deterministically swap its content with their embedded spins, leading to two remote entangled long-lived spins for use in quantum networking.

The DLCZ protocol is, at its core, two single-phonon heralding experiments run-

ning in parallel as seen in Fig. 2-8. However, the detector triggering the heralding is placed after a "path erasure apparatus", e.g. a simple 50-50 beamsplitter. Therefore, when a phonon is heralded by the detection of a photon, the phonon is in an equal superposition of being in the left or in the right node. This results in the two mechanical resonators being in the state $|01\rangle \pm |10\rangle$, with the phase depending on which detector clicked. For details on this path erasure consult [39, 77].

Below we study the fidelity and success probability of the single-phonon heralding protocol, as its performance directly affects the performance of the overall entanglement protocol. In this process, when writing down kets, we will use the Fock basis of the optical and mechanical modes, written down in that order, e.g., $|01\rangle$ is zero photons and one phonon. Two processes are involved in the single-phonon heralding: the two-mode squeezing in Eq. 2.2 which leads to the mapping $|00\rangle \to |00\rangle + \varepsilon|11\rangle + \mathcal{O}(\varepsilon^2)$; and the leakage into a waveguide and subsequent detection of the photon, which projects on the $\varepsilon|11\rangle + \mathcal{O}(\varepsilon^2)$ branches. To properly derive the dynamics we will use a stochastic master equation and we will track the most-probable quantum trajectories manually. The dynamics is governed by the equation

$$\hat{H}_{\text{stoch}} = \hat{H}_0 + \hat{H}_{\text{om}} + \hat{H}_{\text{sm}} - \frac{i}{2} \sum_{c \in \{a, b, b^\dagger\}} \gamma_c \hat{c}^\dagger \hat{c}, \tag{2.20}$$

where the the sum over jump operators $\hat{c}$ provides a way to track the chance for discontinuous jumps. If $|\psi(t)\rangle$ is the state obtained after evolving $|00\rangle$ under $\hat{H}_{\text{stoch}}$, then the probability density for a jump $\hat{c}$ is $\text{pdf}_c(t) = \gamma_c \frac{\langle\psi(t)|\hat{c}^\dagger \hat{c}|\psi(t)\rangle}{\langle\psi(t)|\psi(t)\rangle}$. The operator $\hat{a}$ represents the chance of photon leakage at rate $\gamma_a = \frac{\omega_a}{Q_{\text{opt}}}$ with Q_{opt} the optical quality factor; $\hat{b}$ corresponds to a phonon leaking to the heat bath at rate $\gamma_b = \frac{\gamma_m(n_{\text{th}}+1)}{2}$, where $\gamma_m = \frac{2\Omega}{Q_{\text{mech}}}$ with Q_{mech} the quality factor of the mechanical resonator (notice the different convention leading to a factor of 2 difference); lastly $\hat{b}^\dagger$ corresponds to receiving a phonon from the bath at rate $\gamma_{b^\dagger} = \frac{\gamma_m n_{\text{th}}}{2}$, where $n_{\text{th}} = \frac{k_b \tau}{\Omega}$ is the average number of phonons in the bath, k_b is the Boltzman constant, and τ is the temperature of the bath. Solving for the dynamics and the probability densities of various jumps, as done in details in the interactive supplementary materials [75] leads to:

1. To zeroth order, no jump occurs.

2. To first order, a photon-phonon pair is heralded. The probability of that event is $P_a = \int_0^T \mathrm{d}t\, \mathrm{pdf}_a(t)$.

3. To second order, a photon-phonon pair is heralded and then followed by any other event, for an overall of probability $P_{a*} = 1 - \langle\psi(T)|\psi(T)\rangle$.

4. Also to second order, a b event at time τ is followed by an a event, happening with $P_{ba} = \int_0^T \mathrm{d}\tau\ \mathrm{pdf}_b(\tau) \int_\tau^T \mathrm{d}t\ \mathrm{pdf}_{ba}(t)$.

5. Similarly for $b^\dagger$ followed by a we have probability $P_{b^\dagger a}$.

Above, T is the duration of the pump pulse. These are all the branches of the dynamics that have a chance of triggering a heralding event (to leading order). The total chance for heralding is $P = P_a + P_{ba} + P_{b^\dagger a}$, while the fidelity of the heralded single phonon is $F = \frac{P_a - P_{a*}}{P_a + P_{ba} + P_{b^\dagger a}} f_0$, where $f_0 = \langle 1|\rho_a|1\rangle$ is the fidelity of "good heralding" branch of the dynamics. ρ_a is the density matrix for the state conditioned on only one a event having happened during the pump pulse of duration T.

After simplifying and taking into account that the decay of the optical cavity is much faster than the optomechanical interaction ($T_a = \gamma_a^{-1} \ll (\alpha g_{OM})^{-1}$), we obtain:

$$P = 4\alpha^2 g_{\mathrm{om}}^2 T_a T, \tag{2.21}$$

$$1 - F = 8\alpha^2 g_{\mathrm{om}}^2 T_a T + \frac{3}{4}\gamma_m T_a T\,(3n_{\mathrm{th}} + 1)\,. \tag{2.22}$$

Notice the term in the infidelity that scales exactly as the heralding probability: This is due to the $(O)(\varepsilon^2)$ next-to-leading-order effect in the two-mode squeezing, leading to a proportionally larger chance of more-than-one excitations being heralded. There is also a second term, purely related to the detrimental effects of the thermal bath on the mechanical resonator. As long as $k_b\tau \ll Q_{\mathrm{mech}}\alpha^2 g_{\mathrm{om}}^2$ we can neglect the bath heating term, however this can be difficult to quantify as Q_{mech} strongly depends on τ. This transition between leading sources of infidelity can be seen in Fig. 2-9.

These are the heralding probability and fidelity of a single phononic excitation. The heralding probability and fidelity for the complete entangling protocol, in which two nodes are pumped in parallel and the photon is looked for only after "path-information erasure" differ. To leading order, the probability $P_e = 2P$ is twice as high as either node can produce a photon, and the infidelity scales the same.

For long term storage, we coherently swap the phononic excitation into the spin. The swap gate contributes an additional infidelity of $n_{\text{th}}\gamma_m/g_{\text{sm}}$ which is much lower than other sources of infidelity.

These results, given the design parameters of the previous section, are detailed in Fig. 2-9. Of note is that Q_{mech} is very strongly dependent on the bath temperature due to scattering processes among the thermal phonons. At low temperatures, only clamping losses due to the design of the resonator are of importance, but as the temperature increases, Akhieser and then Landau-Rumer processes become important [47, 40, 79, 97]. The typical dependence for our design and material parameters can be seen in Fig. 2-10. The Akhieser limited quality factor is $Q_A = \frac{1}{\Omega\tau}\frac{\rho c^4}{2\pi\gamma^2\kappa}$, where ρ is density, c is speed of light, γ is the Grüneisen coefficient, and κ is the thermal conductivity. Only κ depends strongly on temperature, and we use the values reported in [147, 119, 17, 113, 14, 52]. At even higher temperature the Landau-Rumer processes dominate with $Q_{LR} = \frac{2\rho c^2}{\pi\gamma^2 C_v \tau}$, where C_v is the diamond heat capacity as reported in [127, 33].

Thus, with our design we can theoretically achieve single-phonon generation at tens of kHz and infidelity lower than 10% at temperature $\tau = 40K$, number of photons in the pump mode $\alpha^2 = 1000$, pump pulse duration $T = T_a$. At lower temperatures the performance significantly improves, giving limiting infidelities far below 1%.

Possible improvements to the protocol include (1) spectral and spatial multiplexing (2) use of a Dicke state of multiple nearby color centers to enhance g_{sm} (3) use the nuclear registers for even longer storage times (4) entanglement purification with the nuclear registers which greatly increase the entanglement fidelity while only marginally decreasing the entanglement rate.

2.5 Discussion

In this paper, we bring the idea of a self-similar concentrator from photonic crystal devices [31] to a 1D optomechanical crystal and explore the usage of the resulting cavity in spin-optomechanical interfacing. This system poses the advantages afforded by highly concentrated optical and mechanical modes: high strain in a central region while retaining optomechanical coupling in diamond relative to previously proposed and demonstrated devices [23], and thus strong spin-phonon interactions. From FEM simulations, we demonstrate that this spin-optomechanical interface can achieve 200 kHz single photon-phonon coupling alongside 40 MHz spin-phonon coupling to a Group IV spin. The strength of this spin-phonon interaction is such that we can effectively ignore losses incurred when swapping a quantum between a cavity phonon and the spin state.

We explore implementation of our interface in an optically heralded entanglement protocol [39, 77]. In this scheme, identical cavities are entangled via heralding, and the resulting entangled phonons are swapped into their respective coupled spins. This entanglement procedure completely circumvents standard issues related to spin-addressing, including the need to operate at the emitter's optical transition wavelength (we define the optical wavelength with a telecom photonic mode) and concerns related to spectral diffusion of emitters (we never optically excite the emitter). Additionally, this scheme places no strong requirements on the optical quality factors required by other works to accomplish spin-mechanical addressing [59, 48]–instead operating with low optical Qs to increase the rate of heralding–and requires on-chip devices that are well within fabricable parameters.

Our spin-optomechanical architecture applies to other material platforms besides diamond. For example, silicon (Si) and silicon carbide (SiC) have been used for optomechanics [42, 29, 128, 91, 93, 92] and have quantum emitters including carbon-based T-centers, phosphorus vacancies, and boron impurities [16, 131]. In particular, Si with B:Si acceptor impurities has been considered for operating spin-phonon coupled systems as an acoustic alternative to circuit-cavity QED [131]. Here, we have

Defect	Mat.	$g_{sm_{proj}}$	$\sim T_1$ (@T)	$\sim T_2$(@T)
SiV^-	Dmd	40MHz	0.1ms@40mK[15]	0.2ms@40mK[15]
SnV^-	Dmd	∼3.5MHz	10ms@3K[148]	0.3ms@1.7K[36]
NV^-	Dmd	∼30Hz	100s@20K[58]	0.6s@77K[13]
B:Si	Si	∼20MHz	5ms@25mK[72]	0.9ms@25mK[72]
P:Si	Si	$\sim$ 45MHz	0.3s@7K[149]	60ms@7K[149]
V:Si	SiC	$\sim$ 20Hz	10s@17K[140]	20ms @17K[140]

Table 2.1: Spin defect candidates for optomechanical interfacing. The defects and their host materials, projected couplings $g_{sm_{proj}}$, and measured T_1 and T_2 at different operating temperatures are listed. The $g_{sm_{proj}}$ of the SnV^-, NV^-, and V:Si were estimated by modifying parameters in the SiV^- coupling formula [148, 155]. The B:Si and P:Si $g_{sm_{proj}}$ were estimated by substituting our $b = 60$ nm mode volume into the formulae in [131] and [142], respectively.

shown that with an intentionally designed optomechanical cavity, one can achieve g_{sm} much larger than previously proposed–which should be the case irrespective of the material, whether diamond, silicon, or another alternative–alongside respectable g_{om}, such that the full spin-optomechanical interface's performance can be evaluated (see Table 2.1). We have analyzed this interface assuming a SiV^- spin, which has well-documented spin-strain parameters [56, 102]; however this spin is indistinguishable above single-Kelvin temperatures [148]. As such, future works may use this spin-optomechanical framework while selecting a suitable combination of material platform and temperature-robust, highly strain-tunable spin defect. The ability to separately engineer quantum memories and spin-photon interfaces, while retaining efficient interfacing between them even at moderate temperatures up to 40 K, will provide much-needed design freedom in applications from quantum networks to computing to sensing.

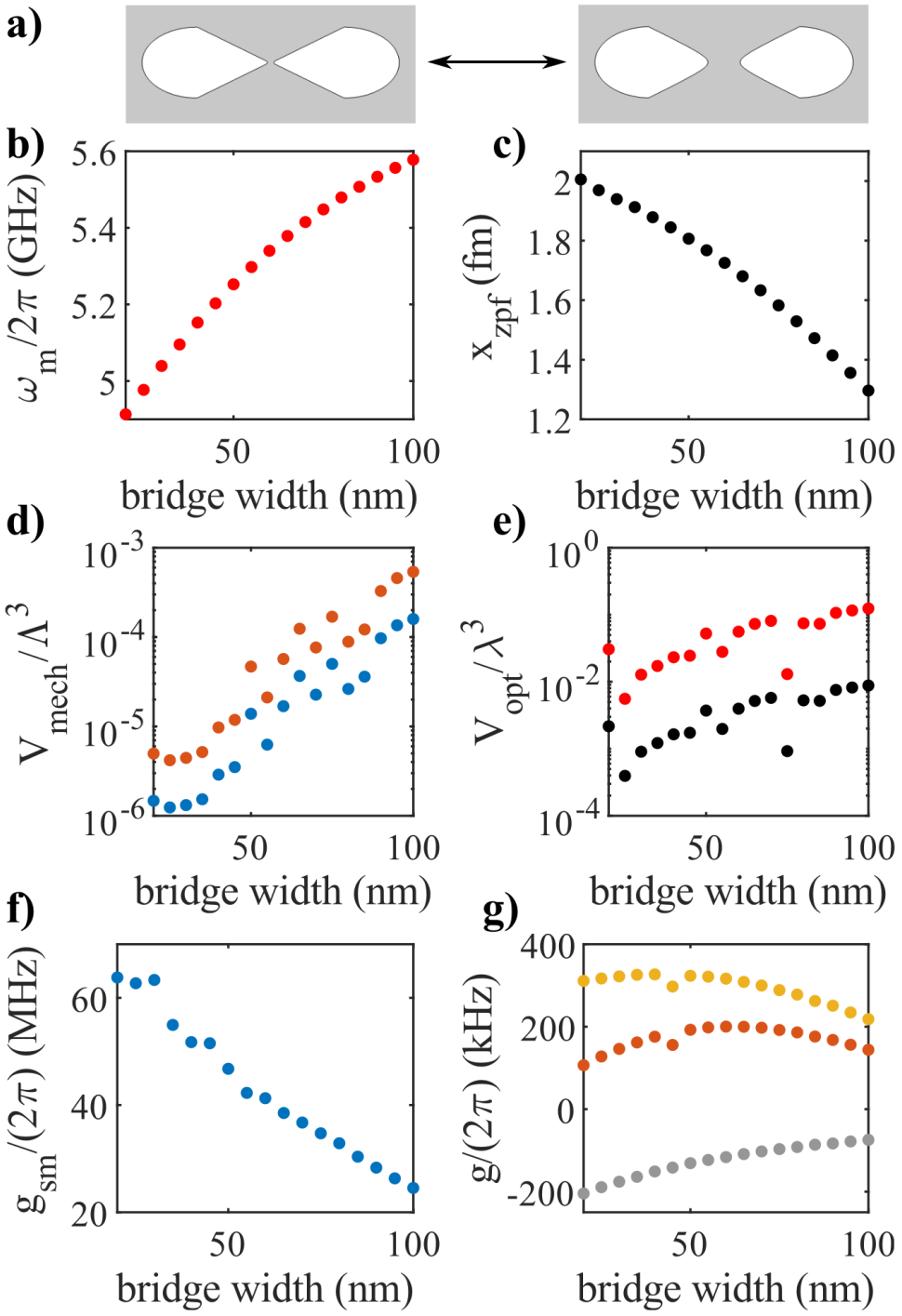

Figure 2-3: Effect of bridge width on device performance. (a) Depiction of bridge width change from 20 nm to 100 nm, followed by plots of bridge width versus (b) mechanical resonant frequency, (c) zero-point fluctuation, (d) mechanical mode volume ($V_{\mathrm{mech}}/\Lambda_{\mathrm{p}}^3$ in blue, $V_{\mathrm{mech}}/\Lambda_{\mathrm{s}}^3$ in orange) (f) maximum g_{sm}, (e) optical mode volume ($V_{\mathrm{opt}}/\lambda^3$ in black, $V_{\mathrm{opt}}/(\lambda/n)^3$ in red), and (g) optomechanical coupling (g_{pe} in yellow, g_{mb} in gray, g_{om} in orange).

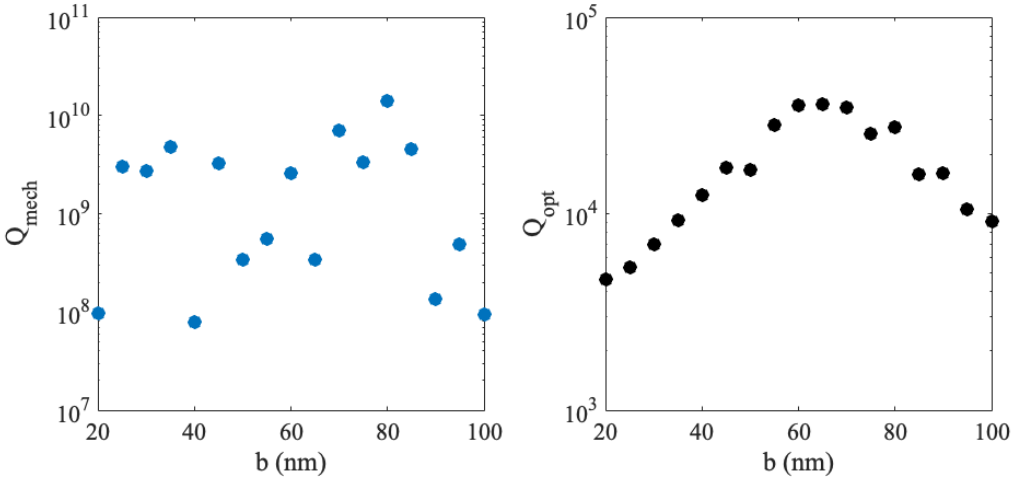

Figure 2-4: Plot of (left) mechanical and (right) optical quality factors as a function of b.

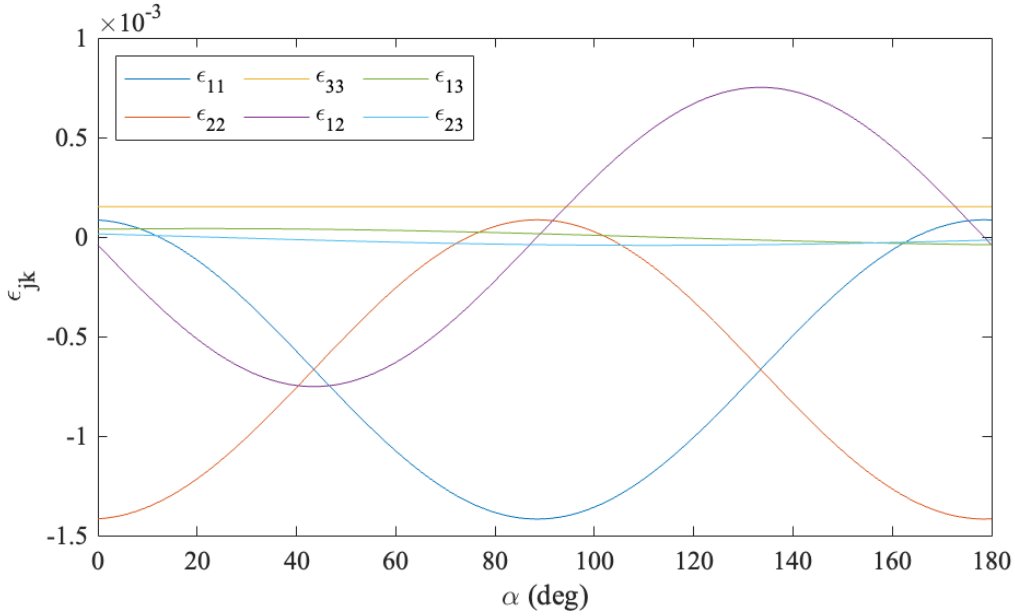

Figure 2-5: Sweep of the diamond crystal orientation strain tensor elements ϵ_{jk} with respect to α. These tensor components were calculated at the middle of the top-right edge of the central taper for the 5.34 GHz acoustic mode ($b = 60$ nm).

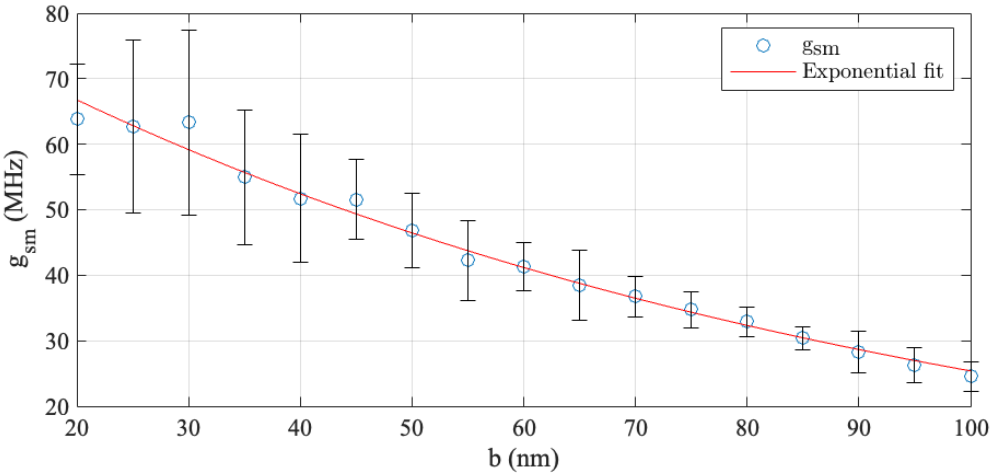

Figure 2-6: Plot of g_{sm} against increasing b.

g_{sm} profile	f (GHz)	Q_{mech}	$g_{sm}/2\pi$ (MHz)
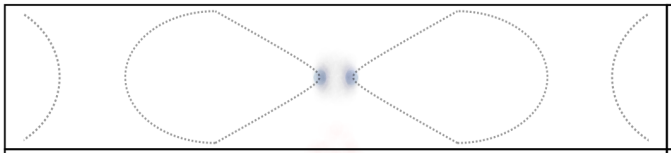	4.91	4.6×10^8	20
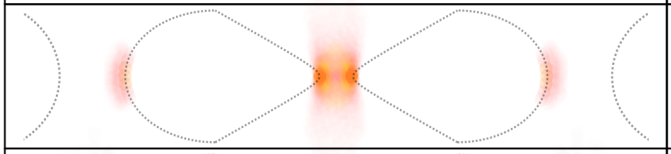	5.34	2.5×10^9	40
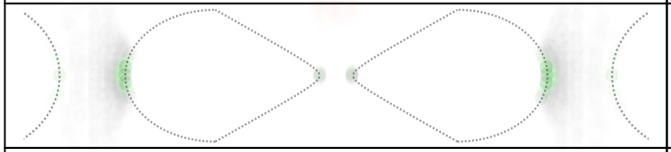	5.79	1.6×10^9	12
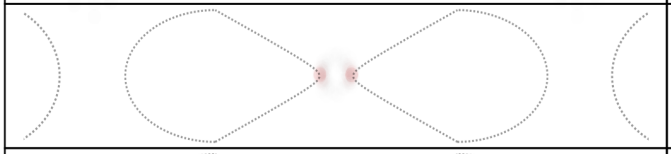	5.85	3.7×10^7	16
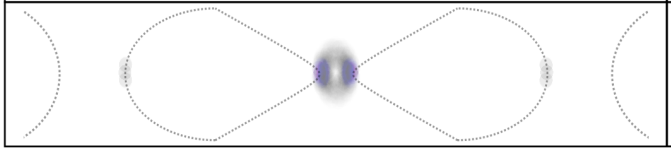	5.95	1.5×10^7	20

Figure 2-7: Locations of high g_{sm} coupling for various mechanical modes. For a given mechanical mode we give its frequency, quality factor, and maximal spin-mechanical coupling g_{sm}. On the left we pictorially represent the locations of maximized g_{sm}. We see that we can select the preferred mode to interact with by its spectral or spatial properties. The thin lines in the plots represent the diamond walls.

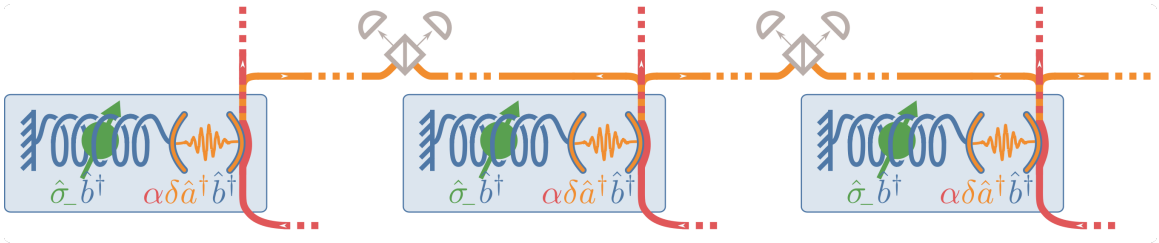

Figure 2-8: Pictorial depiction of the entangling setup. Each node contains an optical resonator (orange cavity) coupled to a mechanical resonator (blue), with an embedded color center (green). A pump (red) is used to induce a two-mode squeezing in the opto-mechanical system. The leakage of an optical photon (orange waveguide) and its detection (gray detector) herald the creation of a single mechanical phonon. A beamsplitter (in gray) can be used to "erase" the knowledge of which is the original source of the photon, leading to the heralding of an entangled state $|10\rangle \pm |01\rangle$ between two neighboring nodes. The phase depends on which of the two detectors clicked.

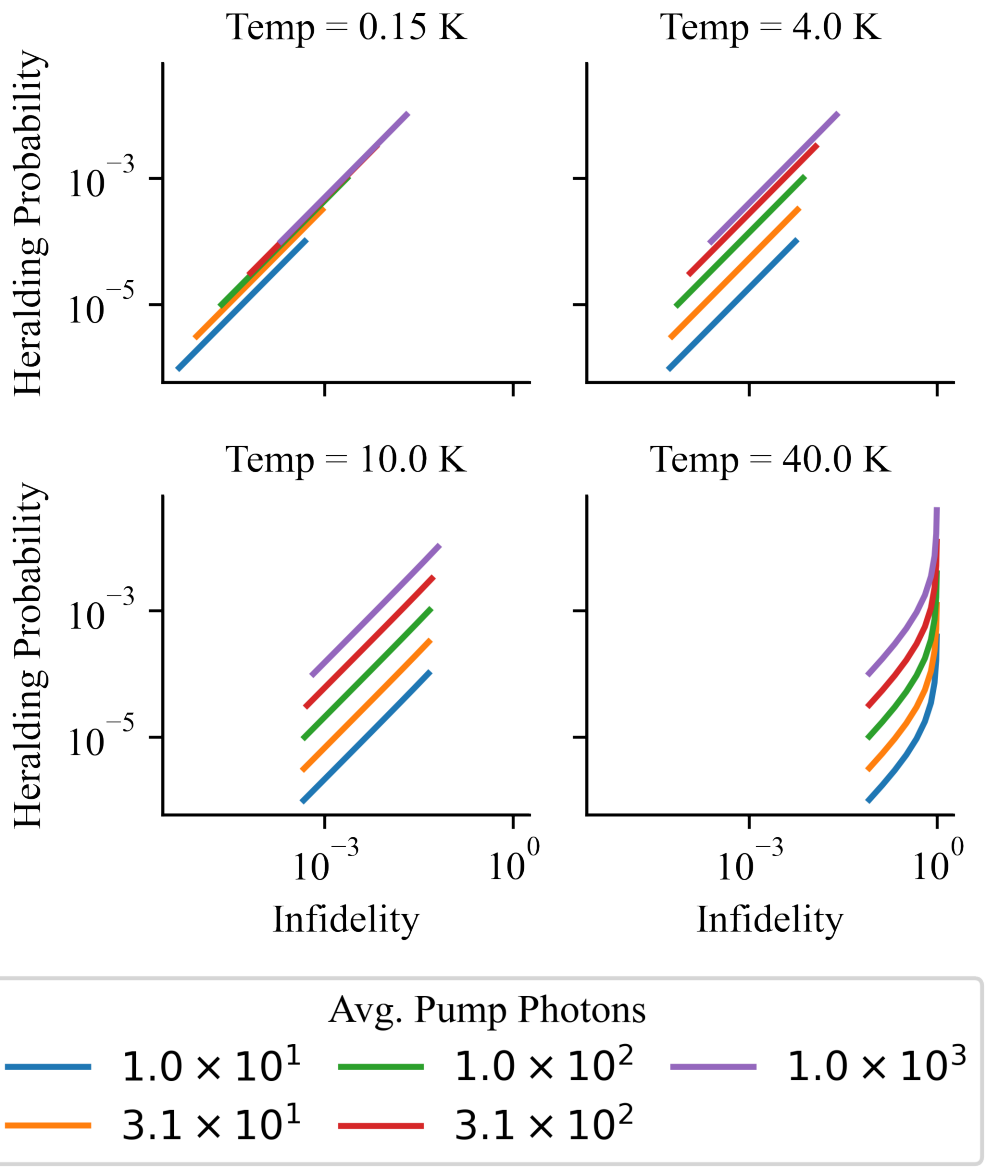

Figure 2-9: Heralding probability and single-phonon infidelities as a function of temperature (facet) and pump power (color), parameterized by pump pulse duration (each line spans $T = T_a$ to $T = 10^3 T_a$). Shorter pulses have lower probability and infidelity. However, the rate of heralding is independent of T as the shorter the pulse (the higher the repetition rate), the lower the heralding probability for that attempt is. Therefore short pump pulses are preferable as that leads to lower infidelity. In this particular setup, at $\tau = 40K$, $\alpha = \sqrt{1000}$, and $T = T_a$, we can theoretically achieve rates of successful single-phonon heralding in the tens of kHz at infidelity lower than 10%. The performance is even better at lower temperatures. At around $4K$ we see that the detrimental effects from the bath of the mechanical resonator become negligible compared to the infidelity due to multi-phonon excitations.

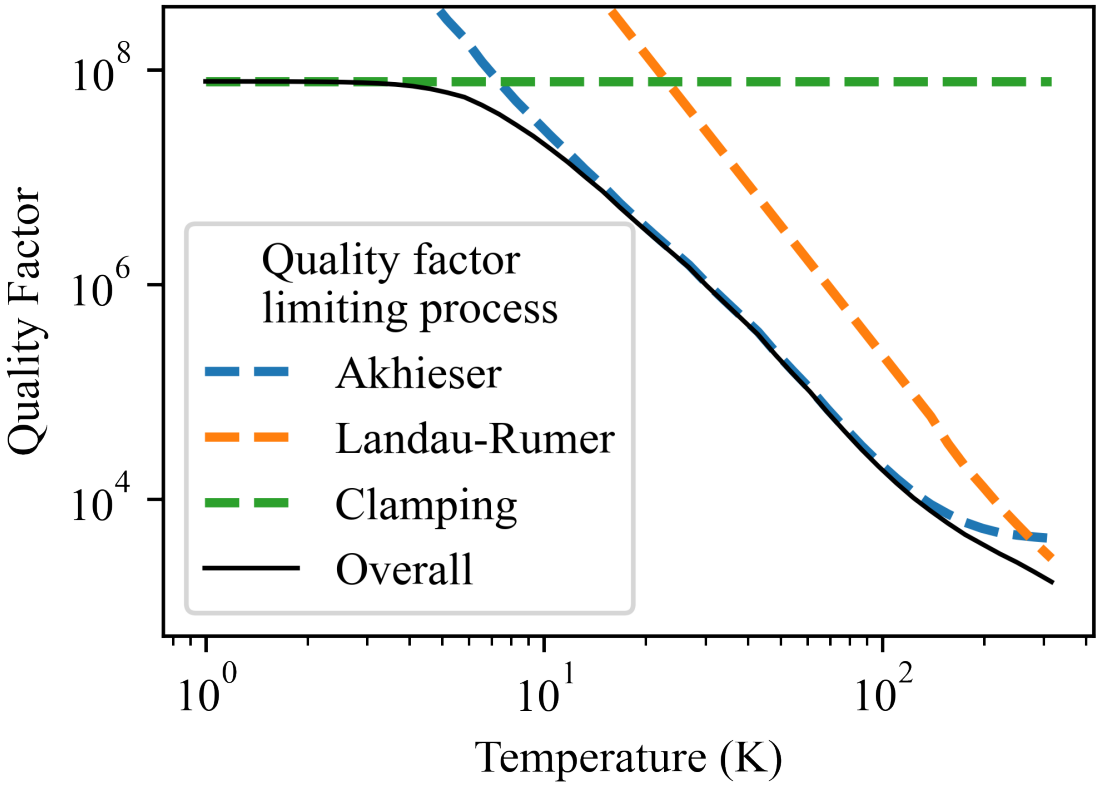

Figure 2-10: The processes limiting the quality factor of a mechanical resonator. At low temperature only clamping losses matter (green), but past a certain temperature Akhieser (blue) and Landau-Rumer (orange) processes dominate. These estimates depend on thermal properties of bulk diamond as reported in the literature. Thin-sheet diamond, as used in our devices, can have slightly differing properties.

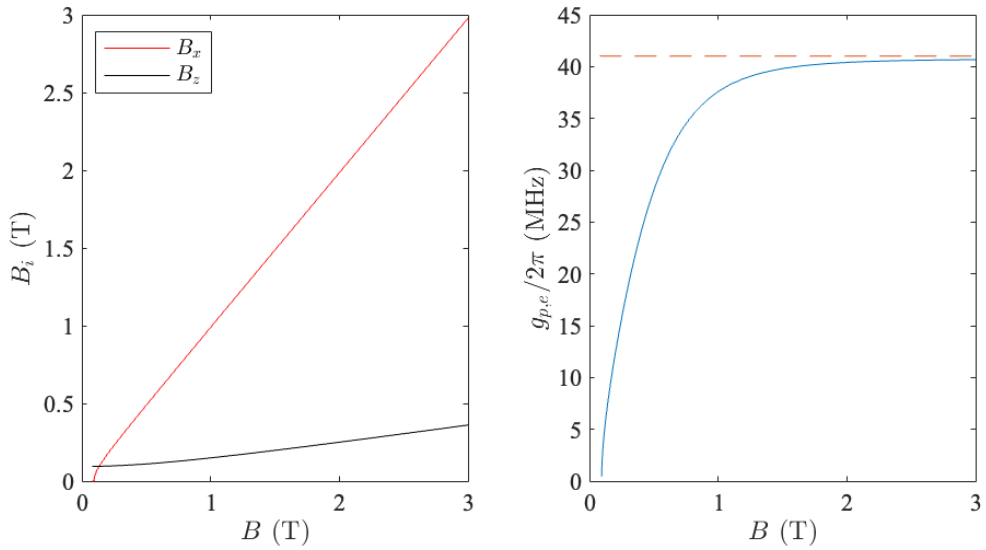

Figure 2-11: Effect of changing magnetic field on the spin-phonon coupling $g_{p,e}$. Change in the necessary magnetic field components to bring the spin transition in resonance with the phonon mode as a function of total magnetic field magnitude (left), and resulting change in $g_{p,e}$ as a function of changing magnetic field magnitude (right). The dotted red line indicates g_{orb} for the spin-optomechanical interface.

Chapter 3

Spin-Electromechanical Transduction

We introduce a hybrid tripartite quantum system for strong coupling between a semiconductor spin, a mechanical phonon, and a microwave excitation of a superconducting circuit. Consisting of a piezoelectric resonator with an integrated diamond strain concentrator, this system achieves microwave-acoustic and spin-acoustic coupling rates ∼MHz or greater, allowing for simultaneous ultra-high cooperativities ($\sim 10^3$ and $\sim 10^2$, respectively). From finite-element modeling and master equation simulations, we estimate superconducting circuit-to-spin quantum state transfer fidelities exceeding 0.97 based on separately demonstrated device parameters. We anticipate that this device will enable hybrid quantum architectures that leverage the advantages of both superconducting circuits and solid-state spins for information processing, memory, and networking.

3.1 Background and Motivation

Solid-state quantum systems based on superconductors and spins are leading platforms that offer complementary advantages in quantum computing and networking. Superconducting quantum processors enable fast and high-fidelity entangling gates [63, 9], but challenges remain in quantum memory time and long-distance networking. Conversely, atom-like emitters in solid-state have demonstrated long spin coherence time, efficient spin-photon interfaces for long-distance entanglement, and high read-

out fidelity [143, 130, 148, 19, 117, 110]. Coupling these modalities is therefore an exciting direction in quantum information science.

Previous studies using magnetic coupling between microwave (MW) photons and spins have been limited to multi-spin ensemble interactions [124, 162, 78, 166, 138, 53, 38] due to low spin-magnetic susceptibility and the low magnetic energy density of MW resonators [26, 121, 5]. Alternate experiments and proposals rely on coupling via intermediate acoustic modes [135, 111, 95], which have experimentally demonstrated large coupling to superconducting circuits [112, 6, 8, 7, 115] and are predicted to have large coupling to diamond quantum emitters [81, 87, 153, 122, 85, 61, 123]. However, designing a device that strongly couples one phonon to both one MW photon and to one spin – enabling an efficient MW photon-to-spin interface – remains an outstanding challenge.

Here we address this problem through the co-design of a scandium-doped aluminum nitride (ScAlN) Lamb wave resonator with a heterogeneously-integrated diamond thin film. This structure piezoelectrically couples a MW photon and acoustic phonon while concentrating strain at the location of a diamond quantum emitter. Through finite-element modeling, we predict photon-phonon coupling ~ 10 MHz concurrent with phonon-spin coupling ~ 3 MHz. These rates yield photon-phonon and phonon-spin cooperativities of order 10^4 assuming demonstrated lifetimes of spins, mechanical resonators, and superconducting circuits [71, 37]. We explore state transfer protocols via quantum master equation (QME) simulations and show that this device can achieve photon-to-spin transduction fidelity $F > 0.97$ with conservative hardware parameters. We find that performance of these schemes is likely limited by two-level system (TLS) loss in current piezoelectrics. An improvement in piezoelectric TLS loss rates to that of silicon will pave the way towards SC-spin state transduction with $F > 0.99$.

3.2 Theory of Superconducting Circuit-Phonon-Spin Coupling

We consider a coupled tripartite system consisting of a superconducting circuit (SC) transmon, acoustic phonon, and Group-IV electron spin. First, we must consider each individual modality in the system (i.e. the transmon, the phononic mode, and the electron spin). Then, we treat the electromechanical and spin-mechanical interaction terms in the system. Finally, we describe the necessary conditions to simplify the system to a transmon and spin coupled to a single phononic mode.

3.2.1 Defining Modalities

We begin by considering a transmon architecture, which consists of a SQUID loop with combined Josephson energy E_J and capacitance C_J in parallel with a shunt capacitor C_S. For the sake of constructing only the coupled system, we omit the transmon readout resonator, which typically consists of a quarter wave resonator coupled in parallel to the transmon. The transmon's Josephson and charging energies are $E_J(\phi) = \frac{I_C \Phi_0}{\pi} \cos(\phi_{ext}) = E_J \cos(\phi_{ext})$ and $E_C = \frac{e^2}{2(C_S + C_J)}$ (I_C is the Josephson junction critical current). Note here that the total charging energy for $\hat{n}$ Cooper pairs will be $4E_C\hat{n}$, where $\hat{\phi}$ is the conjugate variable of $\hat{n}$. Then the transmon Hamiltonian is given by

$$\hat{H}_{transmon} = 4E_C\hat{n} + E_J(\hat{\phi}) \tag{3.1}$$

$$= 4E_C\hat{n} + E_J\left(\hat{\phi} + \frac{1}{2}\hat{\phi}^2 + \frac{1}{6}\hat{\phi}^3 + \frac{1}{12}\hat{\phi}^4 + ...\right) \tag{3.2}$$

$$\approx \left(\sqrt{8E_JE_C} - E_C\right)\hat{a}^\dagger\hat{a} - E_C(\hat{a}^\dagger\hat{a}^\dagger\hat{a}\hat{a}). \tag{3.3}$$

In the last step, we have rewritten in terms of the ladder operators. If we approximate the transmon as a two-level system, then we can simply write $\hat{H}_{transmon}$ as

$$\hat{H}_{transmon}/\hbar = \frac{\omega_{sc}}{2}\hat{\sigma}^z_{sc}. \tag{3.4}$$

Here, the SC frequency ω_{sc} is defined by the transmon Josephson and shunt capacitances as $\omega_{sc} \approx \frac{1}{\hbar}\left(\sqrt{8E_J E_C} - E_C\right)$.

Next, we make note of the Hamiltonian of the electromechanical resonator. Sans coupling, the resonator modes can each be approximated as harmonic oscillators with energy $\hbar\omega_{p,k}$, where $\omega_{p,k}$ is the resonant frequency of the kth resonator mode, plus vacuum energy terms. Ignoring these terms, the Hamiltonian H_{res} is

$$\hat{H}_{res}/\hbar = \sum_k \omega_{p,k}\hat{a}^\dagger_{p,k}\hat{a}_{p,k}. \tag{3.5}$$

Finally, we consider the Hamiltonian of the Group IV electron spin. The full Hamiltonian of Group IV color centers has been discussed at length in [56], but for the purposes of this paper we consider the system under an off-axis (transverse and longitudinal) magnetic field (discussed in [111]). In these conditions, the Group IV Hamiltonian can be written as a sum of the spin-orbit Hamiltonian $\hat{H}^{\mathrm{SO}}$ and a Zeeman perturbation $\hat{H}^{\mathrm{Z}}$ (in the $\{|e_x\uparrow\rangle, |e_y\uparrow\rangle, |e_x\downarrow\rangle, |e_y\downarrow\rangle\}$ basis),

$$\hat{H}_{\mathrm{spin}} = \hat{H}^{\mathrm{SO}} + \hat{H}^{\mathrm{Z}} \tag{3.6}$$

$$= \begin{bmatrix} 0 & 0 & -i\lambda_g & 0 \\ 0 & 0 & 0 & i\lambda_g \\ i\lambda_g & 0 & 0 & 0 \\ 0 & -i\lambda_g & 0 & 0 \end{bmatrix} + \begin{bmatrix} \gamma_s B_z & \gamma_s B_x & iq\gamma_L B_z & 0 \\ \gamma_s B_x & -\gamma_s B_z & 0 & -iq\gamma_L B_z \\ -iq\gamma_L B_z & 0 & \gamma_s B_z & \gamma_s B_x \\ 0 & iq\gamma_L B_z & \gamma_s B_x & \gamma_s B_z \end{bmatrix} \tag{3.7}$$

$$= \begin{bmatrix} \gamma_s B_z & \gamma_s B_x & -i\lambda & 0 \\ \gamma_s B_x & -\gamma_s B_z & 0 & i\lambda \\ i\lambda & 0 & \gamma_s B_z & \gamma_s B_x \\ 0 & -i\lambda & \gamma_s B_x & \gamma_s B_z \end{bmatrix}. \tag{3.8}$$

$$\tag{3.9}$$

Here, we use $\lambda \equiv \lambda_g - q\gamma_L B_z$ [56]. Solving the eigensystem of this Hamiltonian gives

us the eigenvectors

$$|\psi_1\rangle = C_-\Bigg[\left(-i\left(\lambda_- + \sqrt{\gamma_s^2 B_x^2 + (\lambda_-)^2}\right)\right)|e_x\uparrow\rangle + i\,|e_x\downarrow\rangle \\ - \left(\lambda_- + \sqrt{\gamma_s^2 B_x^2 + (\lambda_-)^2}\right)|e_y\uparrow\rangle + |e_y\downarrow\rangle\Bigg], \quad (3.10)$$

$$|\psi_2\rangle = C_-\Bigg[-i\left(\frac{\lambda_- - \sqrt{\gamma_s^2 B_x^2 + (\lambda_-)^2}}{\lambda_- + \sqrt{\gamma_s^2 B_x^2 + (\lambda_-)^2}}\right)|e_x\uparrow\rangle + i\,|e_x\downarrow\rangle \\ - \left(\frac{\lambda_- - \sqrt{\gamma_s^2 B_x^2 + (\lambda_-)^2}}{\lambda_- + \sqrt{\gamma_s^2 B_x^2 + (\lambda_-)^2}}\right)|e_y\uparrow\rangle + |e_y\downarrow\rangle\Bigg], \quad (3.11)$$

$$|\psi_3\rangle = C_+\Bigg[-i\left(\frac{\lambda_+ - \sqrt{\gamma_s^2 B_x^2 + (\lambda_+)^2}}{\lambda_+ + \sqrt{\gamma_s^2 B_x^2 + (\lambda_+)^2}}\right)|e_x\uparrow\rangle + i\,|e_x\downarrow\rangle \\ - \left(\frac{\lambda_+ - \sqrt{\gamma_s^2 B_x^2 + (\lambda_+)^2}}{\lambda_+ + \sqrt{\gamma_s^2 B_x^2 + (\lambda_+)^2}}\right)|e_y\uparrow\rangle + |e_y\downarrow\rangle\Bigg], \quad (3.12)$$

$$|\psi_4\rangle = C_+\Bigg[\left(-i\left(\lambda_+ + \sqrt{\gamma_s^2 B_x^2 + (\lambda_+)^2}\right)\right)|e_x\uparrow\rangle - i\,|e_x\downarrow\rangle \\ + \left(\lambda_+ + \sqrt{\gamma_s^2 B_x^2 + (\lambda_+)^2}\right)|e_y\uparrow\rangle + |e_y\downarrow\rangle\Bigg]. \quad (3.13)$$

These eigenvectors are associated with the eigenvalues

$$\nu_1 = -\sqrt{\gamma_s^2 B_x^2 + (\lambda_-)^2}, \quad (3.14)$$

$$\nu_2 = \sqrt{\gamma_s^2 B_x^2 + (\lambda_-)^2}, \quad (3.15)$$

$$\nu_3 = -\sqrt{\gamma_s^2 B_x^2 + (\lambda_+)^2}, \quad (3.16)$$

$$\nu_4 = \sqrt{\gamma_s^2 B_x^2 + (\lambda_+)^2}. \quad (3.17)$$

Here, we use

$$\lambda_- = \lambda_g - q\gamma_L B_z - \gamma_s B_z, \tag{3.18}$$

$$\lambda_+ = \lambda_g - q\gamma_L B_z + \gamma_s B_z \tag{3.19}$$

$$C_- = \left(\frac{1}{2\sqrt{\gamma_s^2 B_x^2 + (\lambda_-)\left(\lambda_- + \sqrt{\gamma_s^2 B_x^2 + (\lambda_-)^2}\right)}} \right), \tag{3.20}$$

$$C_+ = \left(\frac{1}{2\sqrt{\gamma_s^2 B_x^2 + (\lambda_+)\left(\lambda_+ + \sqrt{\gamma_s^2 B_x^2 + (\lambda_+)^2}\right)}} \right). \tag{3.21}$$

Note that, in the limit where $B_x \to 0$, these eigenvectors and eigenvalues simplify as $\{|\psi_1\rangle, |\psi_2\rangle, |\psi_3\rangle, |\psi_4\rangle\} \to \{|e_+ \uparrow\rangle, |e_+ \downarrow\rangle, |e_- \downarrow\rangle, |e_- \uparrow\rangle\}$ from [56].

The spin frequency ω_e is given by the Zeeman splitting of the electron spin states $ket\psi_1$ and $|\psi_3\rangle$, and the acoustic frequencies $\omega_{p,k}$ are defined by the acoustic resonator geometry. Generally, SCs feature $\omega_{sc} \sim 4 - 6$ GHz [74]. Electron spin resonance frequencies can be arbitrarily set by an external magnetic field; to match this frequency range, fields ~ 0.1 T are required [56].

3.2.2 Physical Motivation of Coupling terms

The coupling coefficient $g_{sc,p}$ is physically governed by the piezoelectric effect, whereby a strain field produces an electric response and vice versa (Fig. 3-2(d)). This interaction is described by the strain-charge equations

$$S_{ij} = s_{ijkl} T_{kl} + d_{kij} E_k, \tag{3.22}$$

$$D_i = d_{ijk} T_{ij} + \epsilon_{ik} E_k, \tag{3.23}$$

where s_{ijkl} and d_{ijk} are the elastic and piezoelectric coefficient tensors of the resonator's piezoelectric material, S_{ij} and T_{ij} are the stress and strain fields, and E_i and D_i are the electric and displacement fields. Given a spatial electric field profile

$\mathbf{E}_{IDT}(\mathbf{r})$ produced by some arbitrary voltage V_{app} across the IDT, the normalized single quantum electric field is [106]

$$\mathbf{e}_{sc}(\mathbf{r}) = \sqrt{\left(\frac{\hbar\omega_{sc}}{\left(C_S + C_J + C_{IDT}\right) V_{app}^2/2}\right)}\mathbf{E}_{IDT}(\mathbf{r})e^{-i\omega_{sc}t}, \tag{3.24}$$

where the capacitances are indicated in Fig. 3-2. Since C_S is typically much larger than C_{IDT} and C_J for transmon qubits, the MW photon energy is largely contained in C_S. Similarly, for a strain profile $\mathbf{T}_p(\mathbf{r})$ produced by an arbitrary mechanical displacement, the normalized single phonon strain field is [106]

$$\mathbf{t}_p(\mathbf{r}) = \sqrt{\left(\frac{\hbar\omega_p}{\int_V dV\ \mathbf{s}(\mathbf{r})|\mathbf{T}_p(\mathbf{r})|^2/2}\right)}\mathbf{T}_p(\mathbf{r})e^{-i\omega_p t}, \tag{3.25}$$

where $\mathbf{s}(\mathbf{r})$ is the elastic tensor at position $\mathbf{r}$. Following (3.23), $\mathbf{t}_p(\mathbf{r})$ will produce an electric displacement field given by $\mathbf{d}\cdot\mathbf{t}_p(\mathbf{r})$, where $\mathbf{d}$ is the piezoelectric coefficient tensor. Then the coupling $g_{sc,p}$ will be determined by the overlap integral between $\mathbf{e}_{sc}(\mathbf{r})$ and $\mathbf{d}\cdot\mathbf{t}_p(\mathbf{r})$ [167],

$$g_{sc,p} = \frac{1}{2\hbar}\int_V dV\left(\mathbf{t}_p^*(\mathbf{r})\cdot\mathbf{d}^T\cdot\mathbf{e}_{sc}(\mathbf{r}) + \mathbf{e}_{sc}^*(\mathbf{r})\cdot\mathbf{d}\cdot\mathbf{t}_p(\mathbf{r})\right). \tag{3.26}$$

The coupling rate $g_{p,e}$ between the lowest lying states $|\psi_1\rangle$ and $|\psi_3\rangle$ can be calculated as

$$\frac{g_{p,e}}{2\pi} = \left|\langle\psi_3| M^{-1}H_{strain}M |\psi_1\rangle\right|, \tag{3.27}$$

where

$$H_{strain} = \begin{bmatrix} \alpha & 0 & \beta & 0 \\ 0 & \alpha & 0 & \beta \\ \beta & 0 & -\alpha & 0 \\ 0 & \beta & 0 & -\alpha \end{bmatrix} \tag{3.28}$$

and M is the matrix that transforms the eigenvectors ψ_i to the strain basis, such that

$$M\hat{H}_{\text{spin}} = M \begin{bmatrix} \nu_1 & 0 & 0 & 0 \\ 0 & \nu_2 & 0 & 0 \\ 0 & 0 & \nu_3 & 0 \\ 0 & 0 & 0 & \nu_4 \end{bmatrix}. \tag{3.29}$$

In SiV^- centers in diamond, β is more than ten times smaller than α [102], so we can simplify H_{strain} to the case where $\beta \to 0$ and $\alpha \to \chi_{eff}(\epsilon_{xx} - \epsilon_{yy})$. Then for a known g_{orb} and a maximum magnetic field magnitude $|B|$, we can plot out the required B_z and B_x alongside the projected $g_{p,e}$ (Fig. 3-1).

It is clear from Eq. 3.27 how the spin-phonon coupling $g_{p,e}$ results from the spin-strain susceptibility χ_{spin} of quantum emitters in a strain field [56, 101, 102]. Then for a single-phonon strain profile $\mathbf{t}_p$, the resulting coupling is $g_{spin}(\mathbf{r}) = \chi_{spin} \cdot \mathbf{t}_p(\mathbf{r})$. In Group IV emitters in diamond, χ_{spin} depends on the spin-orbit mixing, which increases monotonically with an off-axis magnetic field and primarily interacts with transverse strain in the emitter frame [56]. Therefore, for the rest of this analysis, we set this expression to be

$$g_{p,e}(\mathbf{r}) = \chi_{eff}(t'_{xx}(\mathbf{r}) - t'_{yy}(\mathbf{r})), \tag{3.30}$$

where $\mathbf{t}'(\mathbf{r})$ is the single-phonon strain profile in the coordinate system of the emitter and $\chi_{eff} \approx 0.28$ PHz/strain [102].

3.2.3 Conditions for Mode Isolation

Now, we must consider the coupling between the superconducting circuit and the electron spin to all acoustic modes supported by the piezoelectric resonator. The Hamiltonian of describing this interaction can be written as

$$\begin{aligned} \frac{\hat{H}}{\hbar} &= \frac{\omega_{sc}}{2}\hat{\sigma}^z_{sc} + \sum_k \omega_{p,k}\hat{a}^\dagger_{p,k}\hat{a}_{p,k} + \frac{\omega_e}{2}\hat{\sigma}^z_e \\ &+ \sum_k g_{sc,p;k}\left(\hat{\sigma}^+_{sc} + \hat{\sigma}^-_{sc}\right)\left(\hat{a}_{p,k} + \hat{a}^\dagger_{p,k}\right) + \sum_k g_{p,e;k}\left(\hat{\sigma}^+_e + \hat{\sigma}^-_e\right)\left(\hat{a}_{p,k} + \hat{a}^\dagger_{p,k}\right). \end{aligned} \tag{3.31}$$

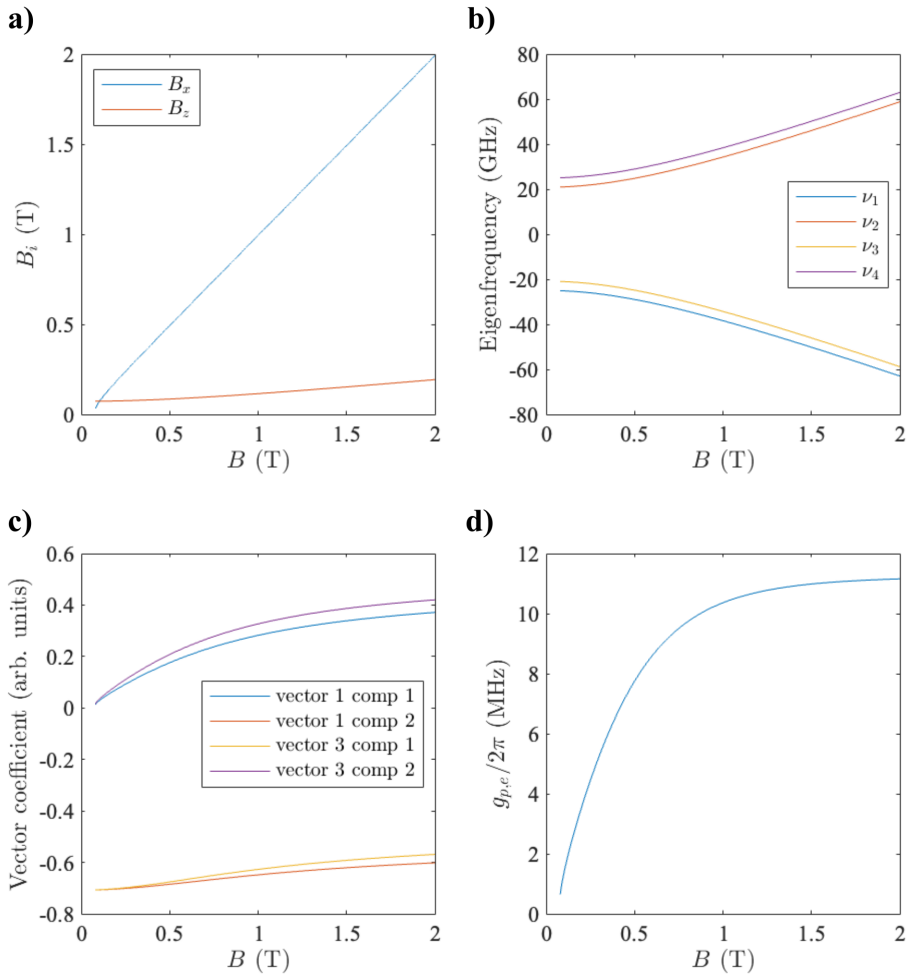

Figure 3-1: Effect of the maximum applicable magnetic field on various parameters of the system. (a) Evolution of the B_x and B_z required to maintain 4.31 GHz spin splitting as a function of $|B|$. (b) Change in eigenfrequencies as a function of $|B|$, where ν_1 and ν_3 are the eigenfrequencies of $|\psi_1\rangle$ and $|\psi_3\rangle$ are the ground state qubit levels of interest. (c) Change in the components of $|\psi_1\rangle$ and $|\psi_3\rangle$ with $|B|$, indicating greater spin-orbit mixing as the maximum applicable magnetic field increases. (d) projected $g_{p,e}$ vs $|B|$ as determined by Eq. (3.27).

where the index k labels each acoustic mode and $\omega_{p,0}$ is the frequency of the resonator mode of interest. We can shift into a interaction picture by applying the transformation $\hat{H}' = \hat{U}\hat{H}\hat{U}^\dagger + i\dot{\hat{U}}\hat{U}^\dagger$, where $\hat{U} = \exp\left[i\left(\frac{\omega_{sc}}{2}\hat{\sigma}_{sc}^z + \sum_k \omega_{p,k}\hat{a}_{p,k}^\dagger\hat{a}_{p,k} + \frac{\omega_e}{2}\hat{\sigma}_e^z\right)t\right]$. This transformation gives

$$\begin{aligned}\frac{\hat{H}'}{\hbar} = &\sum_k g_{sc,p;k}\left(e^{i(\omega_{sc}-\omega_{p,k})t}\hat{\sigma}_{sc}^+\hat{a}_{p,k} + e^{-i(\omega_{sc}-\omega_{p,k})t}\hat{\sigma}_{sc}^-\hat{a}_{p,k}^\dagger\right) \\ &+ \sum_k g_{p,e;k}\left(e^{i(\omega_e-\omega_{p,k})t}\hat{\sigma}_e^+\hat{a}_{p,k} + e^{-i(\omega_e-\omega_{p,k})t}\hat{\sigma}_e^-\hat{a}_{p,k}^\dagger\right),\end{aligned} \tag{3.32}$$

We would like to determine the conditions in which we can neglect all resonator modes except the mode of interest, which we will call k_0 with frequency ω_{p,k_0}. Let us first ignore the spin-phonon coupling and focus on the superconducting circuit-phonon coupling. In the interaction Hamiltonian in Eq. 3.32, we can see that when $\omega_{sc} = \omega_{p,k_0}$ (the frequency of the acoustic resonator mode of interest), Rabi oscillations will be induced between the two modes. We would also, however, like to consider the oscillations induced between the superconducting circuit and the other resonator modes. Let us select a different transformation $\hat{H}_2' = \hat{U}_2\hat{H}\hat{U}_2^\dagger + i\dot{\hat{U}}_2\hat{U}_2^\dagger$, where $\hat{U}_2 = \exp\left[i\left(\frac{\omega_{sc}}{2}\hat{\sigma}_{sc}^z + \sum_k(\omega_{p,k}+\Delta_{p,k})\hat{a}_{p,k}^\dagger\hat{a}_{p,k}\right)t\right]$, where $\Delta_{p,k} \equiv \omega_{sc} - \omega_{p,k}$, and ignore the electron spin-related terms. The resulting interaction Hamiltonian is

$$\frac{\hat{H}_2'}{\hbar} = -\sum_k \Delta_{p,k}\hat{a}_{p,k}^\dagger\hat{a}_{p,k} + \sum_k g_{sc,p;k}\left(\hat{\sigma}_{sc}^+\hat{a}_{p,k} + \hat{\sigma}_{sc}^-\hat{a}_{p,k}^\dagger\right). \tag{3.33}$$

The Heisenberg equations of motion for $\hat{\sigma}_{sc}$ and $\hat{a}_{p,k}$ are

$$\dot{\hat{\sigma}}_{sc}^- = -\frac{i}{\hbar}\left[\hat{H}_2', \hat{\sigma}_{sc}^-\right] \tag{3.34}$$

$$= -\frac{\kappa_{sc}}{2}\hat{\sigma}_{sc}^- - ig_{sc,p;k_0}\hat{a}_{p,k_0} - i\sum_{k\neq k_0} g_{sc,p;k}\hat{a}_{p,k}, \tag{3.35}$$

$$\dot{\hat{a}}_{p,k} = -\frac{i}{\hbar}\left[\hat{H}_2', \hat{a}_{p,k}\right] \tag{3.36}$$

$$= \left(-i\Delta_{p,k} - \frac{\kappa_{p,k}}{2}\right)\hat{a}_{p,k} + ig_{sc,p;k}\hat{\sigma}_{sc}^- \tag{3.37}$$

where $g_{sc,p;k_0}$ is the desired acoustic mode's electromechanical coupling. In matrix

form, this becomes

$$\begin{bmatrix} \dot{\hat{\sigma_{sc}}} \\ \dot{\hat{a_{p,1}}} \\ \dot{\hat{a_{p,2}}} \\ \vdots \\ \dot{\hat{a_{p,N}}} \end{bmatrix} = \begin{bmatrix} -\frac{\kappa_{sc}}{2} & -ig_{sc,p;1} & -ig_{sc,p;2} & \dots & -ig_{sc,p;N} \\ ig_{sc,p;1} & (-i\Delta_{p,1} - \frac{\kappa_{p,1}}{2}) & 0 & \ddots & 0 \\ ig_{sc,p;2} & 0 & (-i\Delta_{p,1} - \frac{\kappa_{p,1}}{2}) & \ddots & 0 \\ \vdots & \ddots & \ddots & \ddots & \vdots \\ ig_{sc,p;N} & \dots & \dots & \dots & (-i\Delta_{p,N} - \frac{\kappa_{p,N}}{2}) \end{bmatrix} \begin{bmatrix} \hat{\sigma_{sc}} \\ \hat{a_{p,1}} \\ \hat{a_{p,2}} \\ \vdots \\ \hat{a_{p,N}} \end{bmatrix}. \tag{3.38}$$

This is equivalent to inducing Rabi oscillations of various frequencies and suppressions between the SC qubit and acoustic modes. The probability amplitude of population transfer to each acoustic mode from an excited SC state becomes

$$\langle \sigma_{sc,k} \rangle = \frac{4(g_{sc,p;k})^2}{4(g_{sc,p;k}^2) + \left| \Delta_{p,k} + i\left(\frac{\kappa_{sc}+\kappa_{p,k}}{2}\right)\right|^2} \sin^2\left(\frac{\sqrt{4\left(g_{sc,p;k}\right)^2 + \left| \Delta_{p,k} + i\left(\frac{\kappa_{sc}+\kappa_{p,k}}{2}\right)\right|^2}}{2} t \right). \tag{3.39}$$

This gives us a SC qubit probability of being in the excited state as a function of time is then

$$\hat{\sigma}_{sc} = \sum_k \langle \sigma_{sc,k} \rangle = \sum_k \frac{4(g_{sc,p;k})^2}{4\left(g_{sc,p;k}\right)^2 + \left(\Delta_{p,k} + i\left(\frac{\kappa_{sc}+\kappa_{p,k}}{2}\right)\right)^2} \sin^2\left(\frac{\sqrt{4\left(g_{sc,p;k}\right)^2 + \left| \Delta_{p,k} + i\left(\frac{\kappa_{sc}+\kappa_{p,k}}{2}\right)\right|^2}}{2} t \right). \tag{3.40}$$

The sum over all $\langle \sigma_{sc,k} \rangle$ with $k \neq k_0$ is a worst-case bound on the probability amplitude that could escape the computational basis into undesired acoustic modes, limiting state fidelity. If the ratio of $\langle \sigma_{sc,k_0} \rangle / \sum_{k \neq k_0} \langle \sigma_{sc,k} \rangle \gg 1$, then we can effectively treat our system as having only one acoustic mode coupled to a SC qubit. The same physics governs the spin-phonon dynamics, replacing the appropriate couplings in equation (3.39) and (3.40).

Assuming that the conditions for mode isolation laid out above are met, the

tripartite coupled system can be simplified to the Hamiltonian

$$\begin{aligned}\frac{\hat{H}}{\hbar} &= \frac{\omega_{sc}}{2}\hat{\sigma}_{sc}^{z} + \omega_p \hat{a}_p^{\dagger}\hat{a}_p + \frac{\omega_e}{2}\hat{\sigma}_e^{z} \\ &\quad + g_{sc,p}\left(\hat{\sigma}_{sc}^{+}\hat{a}_p + \hat{\sigma}_{sc}^{-}\hat{a}_p^{\dagger}\right) + g_{p,e}\left(\hat{\sigma}_e^{+}\hat{a}_p + \hat{\sigma}_e^{-}\hat{a}_p^{\dagger}\right).\end{aligned} \tag{3.41}$$

As explained in the previous subsections, the first three terms of this equation describe the energies of the uncoupled modes of the devices (Fig. 3-2(a-c)) while the fourth and fifth terms describe the interaction dynamics.

3.3 Transducer Design

To implement the device in Fig.3-2, we require a platform with (i) superconductivity, (ii) piezoelectricity, (iii) acoustic cavities, and (iv) strain transfer to diamond emitters. To address (i-ii), we propose a silicon-on-insulator (SOI) platform with a thin-film deposition of scandium-doped aluminum nitride (ScAlN). This material system allows for superconducting qubits and piezoelectrics to co-inhabit one chip [66, 67]. To answer (iii-iv), we co-design a Nb-on-$Sc_{0.32}Al_{0.68}N$-on-SOI piezoelectric resonator with a heterogeneously integrated diamond thin membrane. We propose Niobium (Nb) as a well-characterized superconductor with high $H_{c1} = 0.18$ T and $H_{c2} = 2$ T [133, 69, 44], as required for operation with the spin. We are mostly interested in the regime $0 < |B| \leq 0.18$ T, as this regime lies below the H_{c_1} of Nb. Above the critical field of 0.18 T, we would incur additional losses in the coupled system due to the presence of normal currents in the superconducting circuit. As higher H_{c_1} superconductors are explored as SC qubit materials, higher $|B|$ regimes will become accessible to this scheme. Since $g_{p,e}$ monotonically increases with magnetic field (Fig. 3-1), we will assume a static magnetic field of 0.18 T for the purposes of this work. SOI platforms have previously been used for piezoelectric resonators [89, 90], and diamond-AlN interfaces have been used to acoustically drive emitters in diamond [51, 49, 50]. ScAlN further boosts the piezoelectric coefficient of AlN, allowing us to achieve a stronger

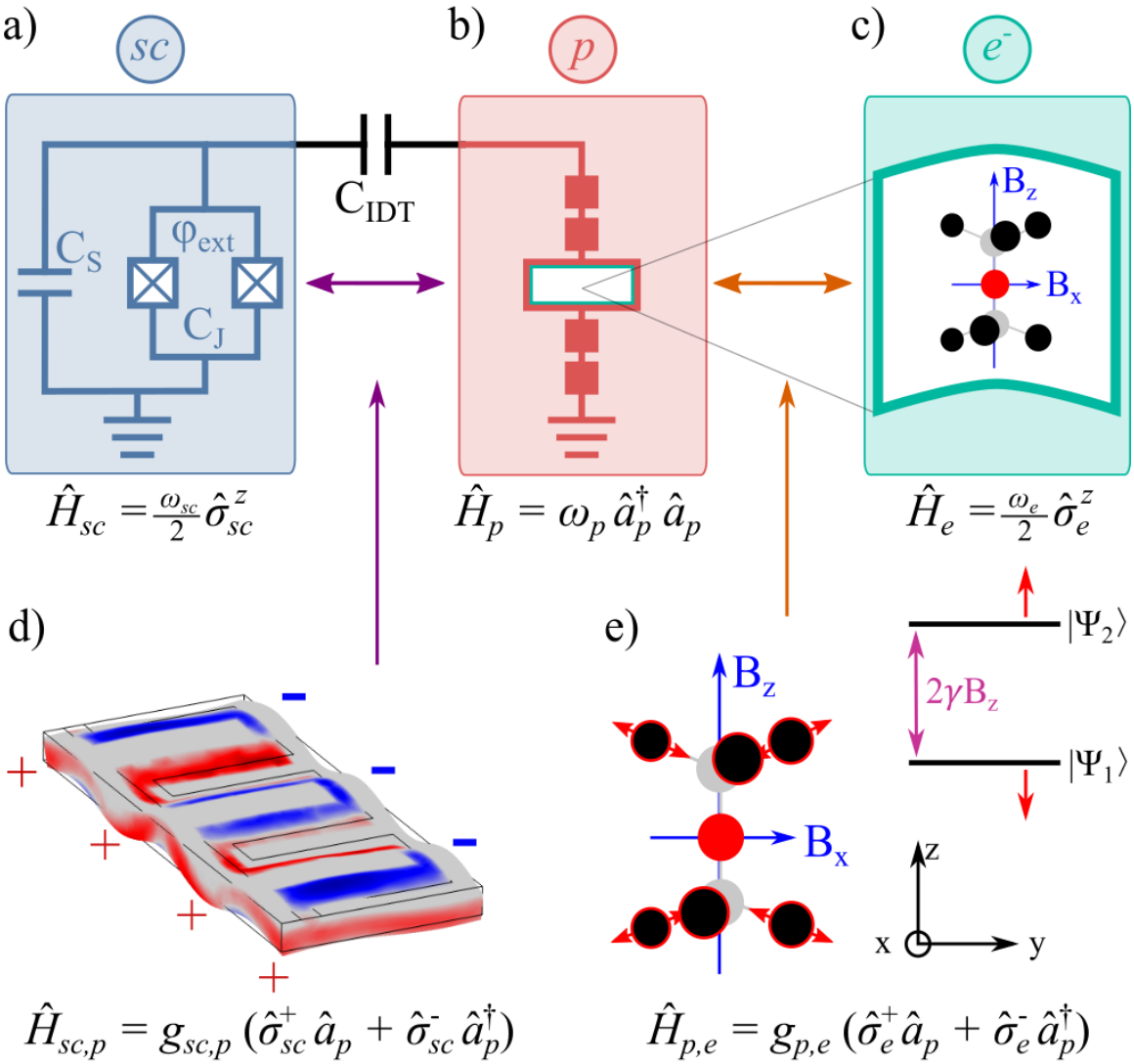

Figure 3-2: Coupled SC-phonon-spin quantum system. (a-c) depict the uncoupled modes of the (a) superconducting qubit with Josephson capacitance C_J, shunt capacitance C_S, and external flux bias ϕ_{ext}; (b) acoustic mode capacitively coupled by C_{IDT}; and (c) diamond quantum emitter. (d) Piezoelectric interaction, where the color indicates the electric field profile under mechanical displacement. (e) Spin-strain coupling resulting from modulating the interatomic distance of the quantum emitter via mechanical strain under an external B field $\mathbf{B} = B_x\hat{\mathbf{x}} + B_z\hat{\mathbf{z}}$ with spin-gyromagnetic ratio γ.

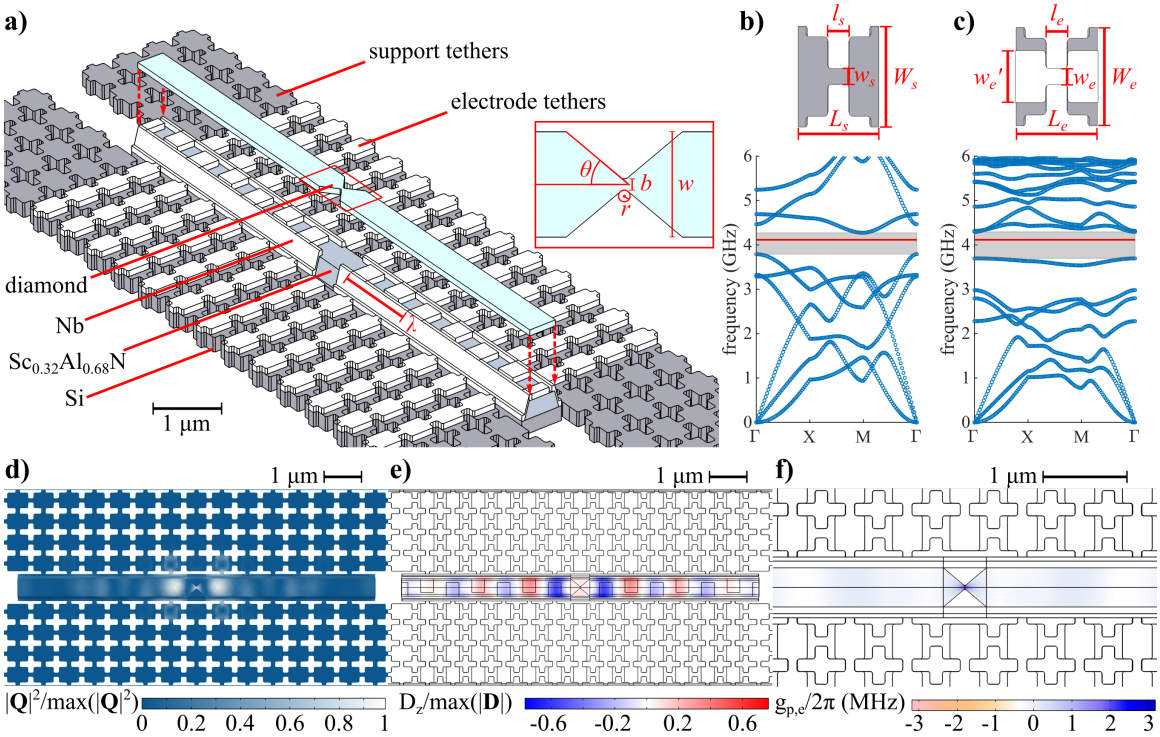

Figure 3-3: Electromechanical transducer design. (a) Lamb wave resonator and relevant design parameters. In this Letter, the resonator geometry is parametrized by $(\lambda, w, t_d, t_{Al}, t_{ScAlN}, t_{Si}) = (1370, 465, 100, 100, 300, 250)$[nm] ($t_i$ is the thickness of layer i), with the diamond taper defined by $(b, r, \theta) = (40\text{ nm}, 25\text{ nm}, 50°)$. The support tethers are defined by $(W_s, L_s, w_s, l_s) = (705, 565, 110, 150)$[nm] and electrode tethers by $(W_e, L_e, w_e, l_e) = (685, 565, 110, 150)$[nm]. (b,c) Phononic band structure of the support (c: electrode) tethers, with a 500 MHz band gap indicated in gray shading and the resonant frequency indicated by the red line. (d) Normalized mechanical displacement of the resonator. (e) Induced piezoelectric displacement field at the central slice of the ScAlN layer. (f) Spatial profile of $g_{p,e}$ at the center slice of the diamond layer, assuming a magnetic field of 0.18 T.

interaction [3, 80].

We present the resonator design in Fig. 3-3. Our device is based on Lamb wave resonators, which produce standing acoustic waves dependent on interdigital transducer (IDT) electrode periodicity λ and material thickness [20, 88, 73]. We localize the strain in the diamond thin film using a fabrication-limited central taper (Fig. 3-3a inset) [134]. To maintain high quality factors, we tether the Lamb wave resonator via phononic crystal tethers placed at displacement nodes of the box. [106]. We further propose an angled ScAlN sidewall in the transducer (15° from normal)

that allows the electrodes to "climb" on top of the ScAlN film, rather than requiring a continuous piezoelectric layer over the phononic tethers. The selected ScAlN and phononic tether parameters outlined in Fig. 3-3, facilitate the design of wide-bandgap phononic tethers and are compatible with current fabrication techniques and tolerances [42, 29, 23, 128, 106].

3.4 Numerical Simulations

We simulate device performance using the finite element method (FEM) in COMSOL Multiphysics, utilizing the Electrostatics and Structural Mechanics modules. We used Stationary electrostatic simulations to determine the electrostatic field applied to the piezoelectric transducer from a microwave source and Eigenfrequency simulations to determine the transducer's resonant acoustic modes. Phononic tether band structures and mode profiles were also found using Eigenfrequency simulations of phononic tether unit cells (Fig. 3-3b-e). The tether band structure exhibits a 500 MHz bandgap around the device's ≈ 4.11 GHz resonant mode. This frequency is desirable as it falls near the central operating range of most superconducting qubits [74].

The coupling parameters $g_{sc,p}$ and $g_{p,e}$ were then calculated using the combination of these two simulations (see Eqs. (3.26) and (3.30)). The parameter set with the best mode isolation (see Fig. 3-5 featured $\lambda = 1370$ nm and $w_{res} = 465$ nm. This device was then tethered using the phononic tethers shown in Fig. 3-3 and the number of tethers were varied to calculate mechanical clamping quality factor Q_c as a function of number of tether periods, shown in Fig. 3-4(b).

Importantly, we demonstrated that the 4.11 GHz resonant mode is itself isolated from other acoustic modes of the system by $\sim$56 MHz, which is enough to neglect parasitic couplings and treat the transducer in the single-mode approximation (Fig. 3-5). Fig. 3-3(d-e) shows the mechanical and electrical displacement fields of this mode, from which we derive $\mathbf{e}_{sc}(\mathbf{r})$ and $\mathbf{t}_p(\mathbf{r})$, respectively. We calculate a $g_{sc,p} \approx 7.0 - 20.5$ MHz (for a shunt capacitance of 65-190 fF, corresponding to 100 MHz $< E_C/h <$ 300 MHz[74]) and a maximum $g_{p,e} \approx 3.2$ MHz according to Equations (3.26) and

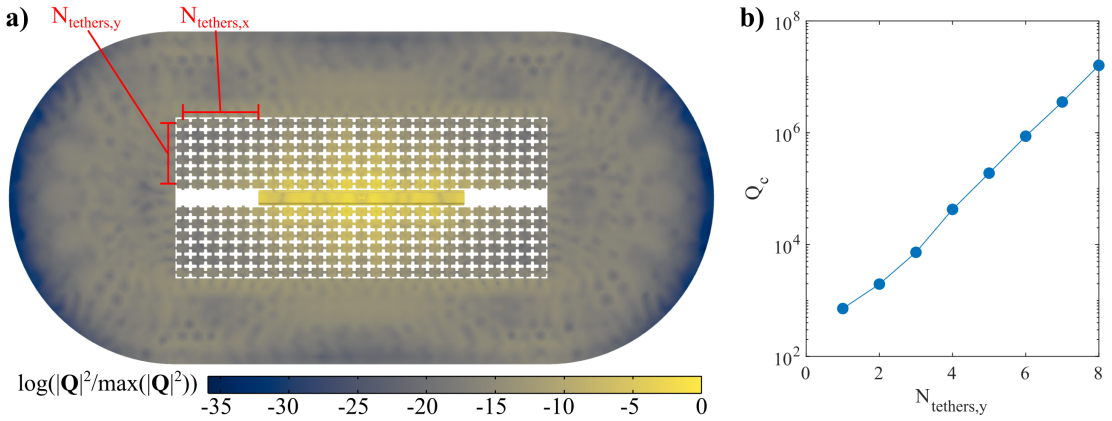

Figure 3-4: FEM simulation of the piezoelectric transducer with phononic tethers and surrounding bulk treated as perfectly matched layers (PML) to simulate clamping quality factor Q_c. (a) Simulated mechanical mode profile with $\log\left(|\mathbf{Q}|^2/\max(|\mathbf{Q}|^2)\right)$ plotted to show energy concentration in the resonator, since energy goes with the square of mechanical displacement. In this simulation, the free parameter $N_{tethers,y} = N_{tethers,x}$, where $N_{tethers,y}$ and $N_{tethers,x}$ indicate the number of phononic mode tether periods normal and parallel to the resonator edge from the resonator to the bulk Si layer, respectively. (b) plot of Q_c vs $N_{tethers,y}$ for the 4.11 GHz resonator mode of interest.

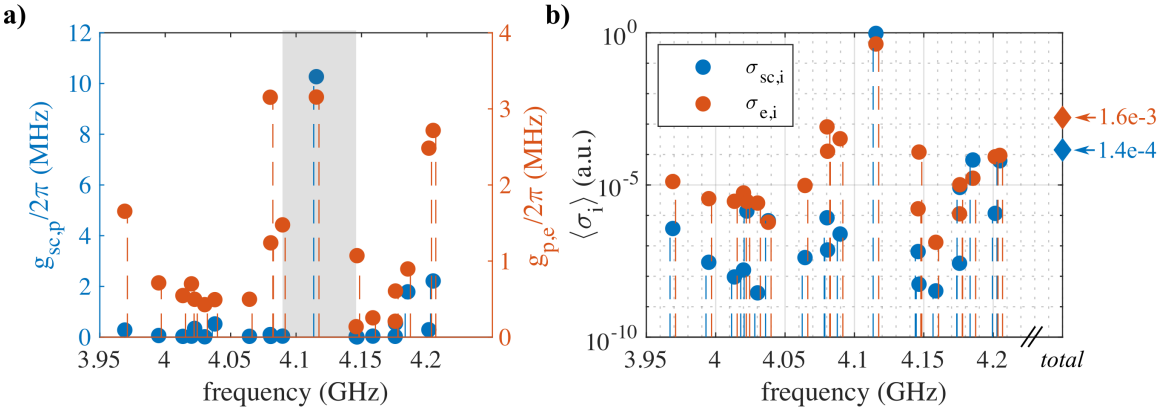

Figure 3-5: Electromechanical and spin-mechanical couplings and population transfer to each acoustic mode. (a) demonstrates a ~ 56 MHz frequency window (grey shaded region) in which our mode of interest (~ 4.115 GHz) lies. The couplings g_{sc,p_i} and g_{p,e_i} are plotted for each mode, assuming a shunt capacitance $C_S \sim 130$ fF and a magnetic field of 0.18 T. (b) displays the Rabi population transfer probability from the superconducting circuit and electron spin to each acoustic mode (see Eq. (3.39)), showing a combined mode suppression (diamond markers) of at least three orders of magnitude

(3.30). The strain maximum occurs at the edges of the central diamond taper, which maximizes $g_{p,e}$ (Fig. 3-3f).

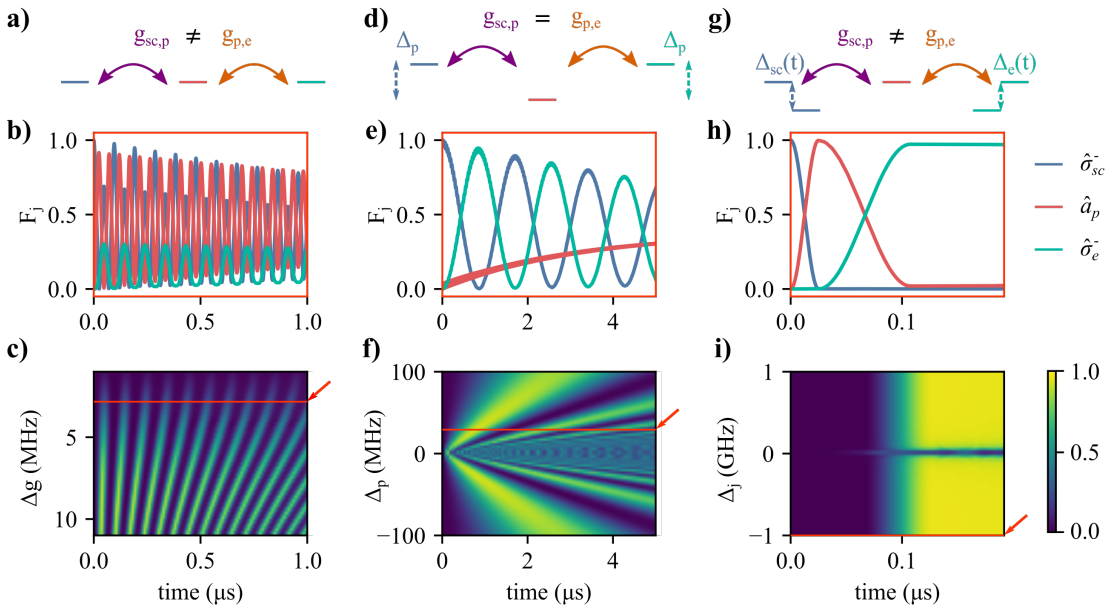

Figure 3-6: Analysis of the coupled SC-phonon-spin system under different protocols: (a-c) uncontrolled time evolution, when all modes are on resonance and coupling rates are maximized; (d-f) time evolution detuned from the acoustic resonance, which allows for state transfer through virtual phonon excitation; and (g-h) time evolution under detuning control, which allows for controlled Rabi flops across the modes. Plots (b,e,h) depict the population dynamics of each mode for the above protocols. Plots (c,f,i) show the spin population over time for the variable parameter of the procedure, with operational points for plots (b,e,h) indicated with orange lines. (c) shows population for a given Δg, (f) shows population for achievable phonon detuning Δ_p, and (i) shows performance for unused mode detuning Δ_i during each Rabi swap.

3.5 Transduction Protocols

In Fig. 3-6, we explore different protocols for quantum transduction from an initialized SC to a spin. The time evolution of the system when initialized in the $\rho_0 = |100\rangle\langle 100|$ state (where the indices consecutively refer to the state of the SC, the Fock state of the phonon, and the z-projection of the spin) is calculated using the Lindblad master

equation,

$$\begin{aligned}\frac{d}{dt}\rho = -\frac{i}{\hbar}[\rho, \hat{H}(t)] + \kappa_p \left(\hat{a}_p^\dagger \rho \hat{a}_p - \hat{a}_p^\dagger \hat{a}_p \rho - \rho \hat{a}_p^\dagger \hat{a}_p\right) \\ + \kappa_{sc} \left(\hat{\sigma}_{sc}^- \rho \hat{\sigma}_{sc}^+ - \hat{\sigma}_{sc}^+ \hat{\sigma}_{sc}^- \rho - \rho \hat{\sigma}_{sc}^+ \hat{\sigma}_{sc}^-\right) \\ + \kappa_e \left(\hat{\sigma}_e^- \rho \hat{\sigma}_e^+ - \hat{\sigma}_e^+ \hat{\sigma}_e^- \rho - \rho \hat{\sigma}_e^+ \hat{\sigma}_e^-\right).\end{aligned} \tag{3.42}$$

where the Hamiltonian in a frame rotating at rate ω_p is

$$\begin{aligned}\frac{\hat{H}(t)}{\hbar} = \frac{\Delta_{sc}(t)}{2}\hat{\sigma}_{sc}^z + \frac{\Delta_e(t)}{2}\hat{\sigma}_e^z \\ + g_{sc,p}\left(\hat{\sigma}_{sc}^+ \hat{a}_p + \hat{\sigma}_{sc}^- \hat{a}_p^\dagger\right) + g_{p,e}\left(\hat{\sigma}_e^+ \hat{a}_p + \hat{\sigma}_e^- \hat{a}_p^\dagger\right).\end{aligned} \tag{3.43}$$

Here, $\Delta_{sc}(t) \equiv \omega_{sc}(t) - \omega_p$ is the superconducting qubit detuning and $\Delta_e(t) \equiv \omega_e(t) - \omega_p$ is the spin detuning at time t. The use of time-varying detuning can be easily implemented, e.g. via on-chip flux bias lines [139, 144, 99], unlike time-varying coupling rates explored in previous works [111]. We account for dephasing in each mode with conservative estimates on decoherence rates $\frac{\kappa_{sc}}{2\pi} = 100$ kHz, $\frac{\kappa_p}{2\pi} = \frac{\omega_p}{2\pi Q} \approx 40$ kHz, and $\frac{\kappa_e}{2\pi} = 1$ MHz [37, 71, 120, 145, 116]. As cryogenic operation of ScAlN-on-SOI acoustic resonators–as well as diamond hybrid integration on said devices–has not been previously explored, we further discuss prospects for Q_{mech} below.

Fig. 3-6(b,e,h) plot the state transfer fidelity $F_j \equiv \langle\psi_j| \rho(t) |\psi_j\rangle$ to the target state $|\psi_j\rangle = |1_j\rangle$ under different conditions. In Fig. 3-6a where the modes are all resonant ($\omega_{sc} = \omega_p = \omega_e = 4.11$ GHz), and $g_{sc,p}/2\pi = 10$ MHz, F_e is poor due to the mismatch $\Delta g(g_{p,e}) = g_{sc,p} - g_{p,e}$ (Fig. 3-6c). Assuming one reduces $g_{sc,p}$ or $g_{p,e}$, for example by increase the qubit shunt capacitance C_S or reducing the transverse magnetic field, F_e may increase at the cost of maximum coupling rates.

In Fig. 3-6b we detune the phonon mode by $\Delta_p \equiv \omega_p - \omega_{sc}$ where $\omega_{sc} = \omega_e$ and keep the coupling rates matched at 3.0 MHz. In this case, $F_e \sim 0.95$ via virtual excitation of the phonon mode, if the phonon mode is detuned by 30 MHz. This protocol generates a very low population in the phonon mode, primarily exchanging states between the superconducting qubit and spin. If the phonon mode is lossy, this transduction method is then preferred. However, while this protocol features wider efficiency peaks in time, which may require less stringent pulse control (see Fig. 3-6e),

it does not overcome the issue of coupling imbalance and additionally suffers from decoherence of the superconducting qubit and spin modes over a longer protocol time (Fig. 3-6f).

Fig. 3-6g shows the optimal solution, assuming control over $\Delta_{sc}(t)$ and $\Delta_e(t)$, in a double Rabi-flop protocol. During this protocol, it is assumed that $g_{sc,p}/2\pi = 10$ MHz (which overcomes losses during the Rabi flop while still allowing mode isolation during the next flop) and $g_{p,e}/2\pi = 3.0$ MHz. We also assume $\Delta_{sc}(t) = 0$ and 0 MHz $\leq \Delta_e(t) \leq 1$ GHz for $t \in \{0, \pi/(2g_{sc,p})\}$–the duration of a Rabi flop between the SC and phonon. Then, $\Delta_{sc}(t) = \Delta_e(t = 0)$ MHz and $\Delta_e(t) = 0$ for $t \in \{\pi/(2g_{sc,p}), \pi/(2g_{sc,p}) + \pi/(2g_{p,e})\}$–the duration of a Rabi flop between the phonon and spin. This sequentially transfers states between the modes (Fig. 3-6h), and for $\Delta_e(t = 0) > 500$ MHz, can achieve $F_e > 0.97$ (Fig. 3-6i; for $\Delta_j = 1.0$ GHz, $F_e = 0.971$). In this protocol, we have neglected the losses that can occur when varying Δ_{sc} and Δ_e. In reality, one has to select a pair of Δ_{sc} and Δ_e that do not fall on resonance with another acoustic mode of the system to prevent Rabi oscillations between the SC qubit or electron spin and an undesired acoustic mode (see SI for more details).

Each of these scenarios achieves transduction to the spin with high fidelity. The third scenario allows the quantum state to persist in the spin without continued interaction with the acoustic or SC modes. While in this state, the electron spin can access other degrees of freedom (e.g. ^{13}C spins [104, 94]).

Since acoustic losses and therefore the total mechanical quality factor Q_{mech} are difficult to predict from first principles, we evaluate the transduction fidelity F_e of each protocol in different regimes of Q_{mech} in Fig. 4. Here, protocol 1 is the resonant protocol with $g_{sc,p} = g_{p,e} = 3$ MHz; protocol 2 is the virtual excitation protocol with identical $g_{sc,p}$ at a detuning of 30 MHz; and protocol 3 is the Rabi protocol with $g_{sc,p} = 10$ MHz, $g_{p,e} = 3$ MHz, and $\Delta_e(t = 0) = 1$ GHz. Q_{mech} is the inverse sum of three components,

$$Q_{mech} = \left(Q_c^{-1} + \sum_l p_i \left(Q_{TLS,l} \right)^{-1} + Q_A^{-1} \right)^{-1}. \tag{3.44}$$

We can engineer Q_c to be non-limiting (Fig. 3-4). Additionally, Q_A–the Akhiezer loss-related Q–is negligible at millikelvin temperatures[27]. These two losses are well-described for analogous systems; in contrast, $Q_{TLS,l}$–the lth material's dielectric loss-related Q–is harder to predict. These Qs depends on the number of quasi-particles or TLSs trapped in each of the device's material interfaces and are weighted by the electric field participation p_i in each interface. We note that Q_{TLS} likely limits F far more than fabrication imperfections (which fall under Q_c) or errors due to heating at milliKelvin temperatures. Given this uncertainty in Q_{TLS_i}, we lay out the protocol hierarchy as a function of the overall Q_{mech}:

- If $Q_{mech} \lesssim 2 \times 10^3$, protocol 2 is superior.
- If $2 \times 10^3 \lesssim Q_{mech} \lesssim 5 \times 10^5$, protocol 1 is superior.
- If $5 \times 10^5 \lesssim Q_{mech}$, protocol 3 is superior.

In existing hardware, the largest challenge to reach the high-fidelity regime ($F \gtrsim 0.99$) is reducing dielectric loss in the thin-film piezoelectric, as indicated by published intrinsic quality factors of, e.g., monolithic aluminum nitride or lithium niobate resonators [43, 157]. So, while current hardware may encourage us to utilize the virtual coupling protocol for coupling through a lossy intermediary phononic mode, future iterations of this scheme with improved materials and interfaces can expect to break the 0.99 transduction fidelity barrier using a resonant protocol. At this fidelity, SC-spin transduction would surpass the 1% error correction thresholds of common codes and thus be compatible with scalable quantum information processing schemes [70, 125, 152].

An open question remains in the bonding strength between the diamond thin film and underlying resonator, which, if poor, can incur additional losses. However, for single-phonon occupation, the Van der Waals static frictional force exceeds the strain-generated force on the resonator.

Ultimately, we have proposed a resonator architecture capable of simultaneously coupling a microwave photonic mode from a superconducting circuit and an electronic

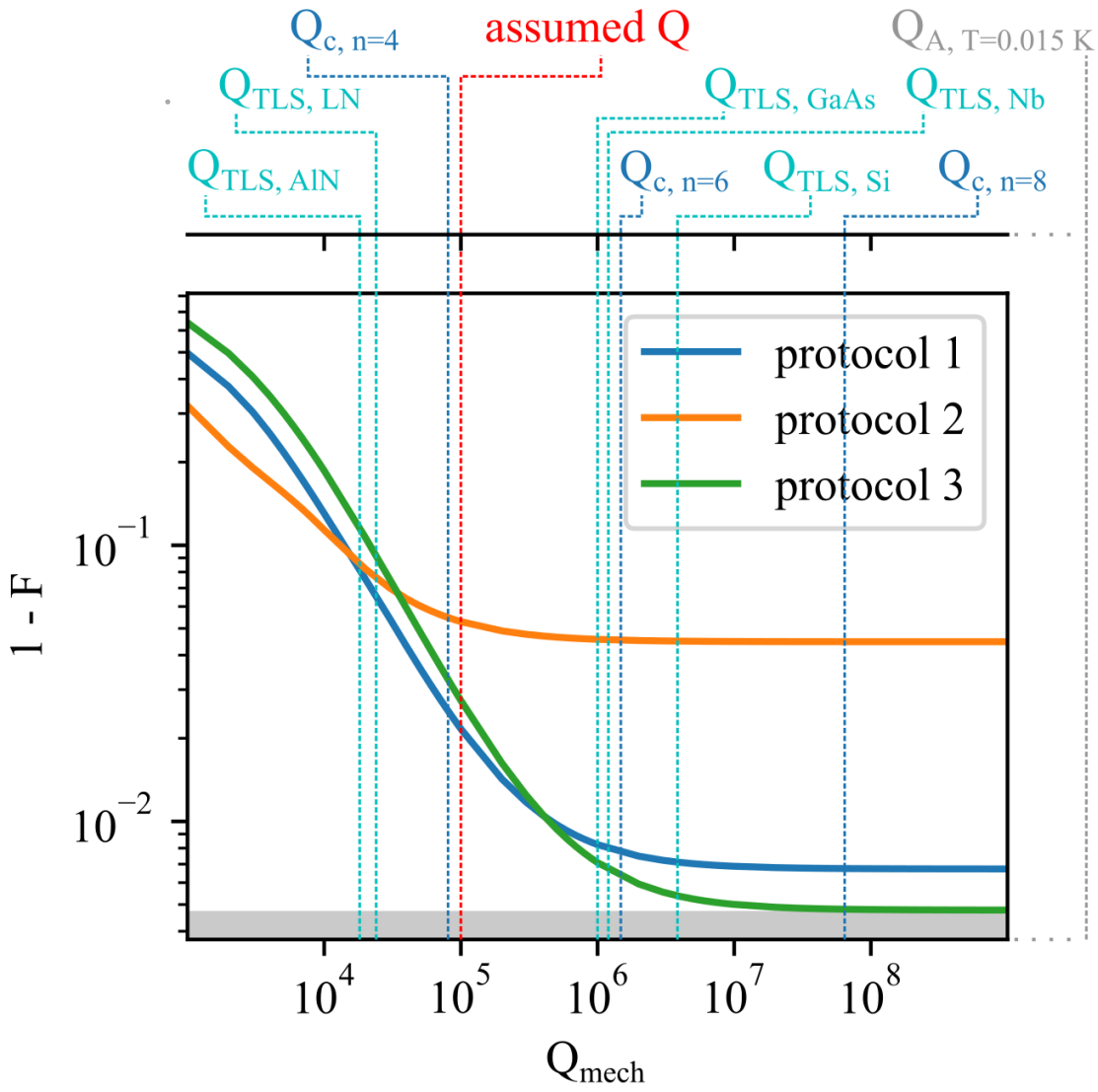

Figure 3-7: Sweep of protocol performance as a function of the total quality factor of the mechanical resonator. TLS-limited Qs–which are inherent to the materials used in the pizeoelectric nanocavity–for Si [103, 160], AlN [43], Nb [100], and alternatives in GaAs [100] and LN [157] are in cyan. The device's clamping-limited Qs as a function of tether number–which determines the phononic mode isolation from the bulk chip–are listed in blue. Akhiezer losses (gray) are non-dominant at $T = 0.015$ K. Finally, our assumed $Q \approx 10^5$ for simulations in Fig. 3-6 is in red. The $F > 0.995$ regime (dark gray) requires better SCs and spins to achieve.

spin from a solid state color center to a single phonon. For our calculated coupling parameters and conservatively assumed Qs across the three modes, we expect SC-phonon cooperativity $C_{sc,p} = \frac{4g_{sc,p}^2}{\kappa_{sc}\kappa_p} \sim 4 \times 10^3$ and similarly, spin-phonon cooperativity $C_{p,e} = \frac{4g_{p,e}^2}{\kappa_p\kappa_e} \sim 10^2$. This doubly strongly-coupled architecture has a number of uses. Firstly, it can provide superconducting circuit qubits access to a long-lived quantum memory in the form of a nuclear spin register surrounding the electron spin. Secondly, this resonator can grant superconducting circuit qubits a spin-photon interface for efficient coupling to fiber optical quantum networks. Finally, by multiplexing each SC with several acoustic resonators and each acoustic resonator with several spins, this architecture can yield a memory bank of quantum memories for computational superconducting circuits.

3.6 Analysis of Spin Register System

In Figure 3-8, we present a roadmap to scaling this architecture to form a memory register for superconducting circuits. Since the shunt capacitance far exceeds the capacitance of a single IDT, additional electromechanical resonators in parallel to a single transmon qubit do not significantly change the coupling rates to each resonator. Individual control over each resonator can be obtained with (i.e. cryo-MEMS) electrical switching of contacts to each resonator [21]. If this is not possible, controls can still be obtained in the frequency domain if each resonator frequency is sufficiently detuned from all others and within the tunability range of the transmon. This gives two constraints on the number of parallel resonators we can add: the maximum number of resonators before $g_{sc,p}$ for each resonator drops below a desired value, and the maximum number of resonators before the frequency spectrum becomes overcrowded.

From electrostatic simulations in COMSOL, $C_S \approx 70 C_{IDT}$, allowing us to add around 10 resonators in parallel without decreasing the coupling to each resonator by more than 15%. Additionally, each resonator can house several quantum emitters, which themselves will be operating at different frequencies $\omega_{e,ij}$ due to differing magnetic field and strain environments creating a unique Zeeman effect for each color

center. Assuming one implants n emitters in each resonator, this creates an easily accessible $m \times n$ register of ancillas for a single transmon.

We would like to evaluate overcrowding of the frequency spectrum in this picture. In an ideal case, when we tune the superconducting circuit on resonance with a mechanical mode ω_m, we would like the circuit to be approximately coupled *only* to that acoustic mode. This is the same condition as we presented in Appendix A to assume that we can simplify the dynamics of the SC-phonon-spin system to that of coupling via a single acoustic mode. Thus, when the condition for every mode j, then we can suppose that we individually couple to one piezoelectric resonator out of a number of resonators (see Fig. 3-8). Similarly, we would like to determine the condition where we can assume each piezoelectric resonator can individually couple to a single spin. This complicates the second stage of the system in Appendix A. Assuming that the conditions in Appendix A already holds for each of m resonators coupled to the SC qubit, the full Hamiltonian describing the m resonator, $m \times n$ spin system is

$$H_{\sum} = \frac{\omega_{sc}}{2}\hat{\sigma}_{sc}^{z} + \sum_{i=1}^{m}\sum_{j=1}^{n}\left[\omega_{p,i}\hat{a}_{p,i}^{\dagger}\hat{a}_{p,i} + \frac{\omega_{e_{ij}}}{2}\hat{\sigma}_{e_{ij}}^{z} + g_{sc,p_i}\left(\hat{\sigma}_{sc}^{+}\hat{a}_{p,i} + \hat{\sigma}_{sc}^{-}\hat{a}_{p,i}^{\dagger}\right) + g_{p,e_{ij}}\left(\hat{\sigma}_{e_{ij}}^{+}\hat{a}_{p,i} + \hat{\sigma}_{e_{ij}}^{-}\hat{a}_{p,i}^{\dagger}\right)\right]. \tag{3.45}$$

Following exactly from Eqs. 3.39 and 3.40, the required condition for assuming electromechanical coupling to just the i_0th of m resonators is that

$$\sum_{i\neq i_0}^{m}\langle\sigma_{sc,i}\rangle = \sum_{i\neq i_0}^{m}\frac{4(g_{sc,p;i})^2}{4(g_{sc,p;i}^2) + \left|\Delta_{p,i} + i\left(\frac{\kappa_{sc}+\kappa_{p,i}}{2}\right)\right|^2}\sin^2\left(\frac{\sqrt{4\left(g_{sc,p;i}\right)^2 + \left|\Delta_{p,i} + i\left(\frac{\kappa_{sc}+\kappa_{p,i}}{2}\right)\right|^2}}{2}t\right) \ll \langle\sigma_{sc,i_0}\rangle. \tag{3.46}$$

Similarly, after swapping population into one of the resonator modes, the condition

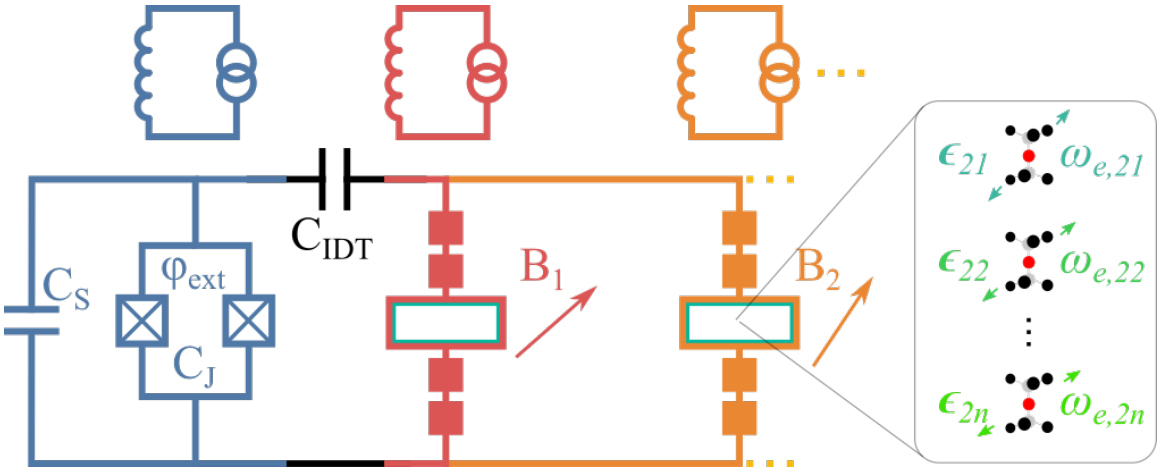

Figure 3-8: Scaling the schematic to a quantum memory register. By implanting n emitters in each of m detuned mechanical resonators in parallel with the superconducting qubit of interest, one can create an efficient interface to an $m \times n$ optically addressable ancilla register.

for assuming spin-mechanical coupling to just the j_0th of n electron spins is that

$$\sum_{j\neq j_0}^{n}\langle\sigma_{e,j}\rangle = \sum_{j\neq j_0}^{n}\frac{4(g_{p,e;j})^2}{4(g_{p,e;j}^2)+\left|\Delta_{p,j}+i\left(\frac{\kappa_e+\kappa_{p,j}}{2}\right)\right|^2}\sin^2\left(\frac{\sqrt{4\left(g_{p,e;j}\right)^2+\left|\Delta_{p,j}+i\left(\frac{\kappa_e+\kappa_{p,j}}{2}\right)\right|^2}}{2}t\right) \ll \langle\sigma_{e,j_0}\rangle. \tag{3.47}$$

We can see from the spin-phonon coupling points in Fig. 3-5 that frequency crowding can begin to promote Rabi oscillations with populations on the order of 10^-3 of the desired mode when within a 100 MHz frequency window. So parallelization of spins in one resonator would require changing the local magnetic field for each resonator and intelligent spacing of the emitters to promote a wide distribution of resonant frequencies, or sacrificing state transfer fidelity to a single spin by overcrowding the simulated frequency window of operation. This is not as much of a problem given the order-of-magnitude superior mode suppression on the electromechanical side of the system. Thus, we can comfortably parallelize around 10 piezoelectric resonators to a single SC qubit and 1-3 emitters per resonator. When accounting for the surrounding

^{13}C nuclear spins, we envision that this scaling method can provide a SC qubit with a 10+ nuclear spin memory register.

3.7 Implementing Quantum Protocols on a Tripartite System

In Fig. 3-9, we describe the SWAP gate between a superconducting transmon and SiV^- electron spin implemented by our transduction protocols (specifically Protocol 3 in the main text). This consists of two SWAP gates between first the transmon and transducer's phonon mode and next between the phonon mode and electron spin. We propose that the first SWAP is initiated by tuning the flux bias of the transmon SQUID loop to tune the transmon in and out of resonance with the phononic mode (Eq. (3.1)) [74]. Similarly, an external magnetic field can be varied to tune the electron spin transition in and out of resonance with the phonon to initiate the second SWAP gate (Eq. (3.10)-(3.13)). Once an excitation is transferred to the electron spin, then optical readout can be carried out using a free space laser tuned to the electron spin transition frequency. Note that the diffraction limited spot size of a $\lambda = 620$ nm laser entering a high numerical aperture (NA) microscope–for example, an NA of 0.9–is around $d = \frac{\lambda}{2NA} = 344$ nm, which is smaller than the distance between two electrodes in our device. Therefore, we expect that a free space laser shouldn't cause excessive scattering.

Fig. 3-10 shows how to use the transducer in a quantum computation scheme that combines distilled entanglement with computation and memory storage. First, one can initialize two systems in different dilution fridges featuring our transducer to the ground state and carry out a distilled entanglement scheme using the SiV^- electron spins and coupled ^{13}C nuclear spins in each transducer (Fig. 3-10a) [64]. Next, one can implement a SWAP gate between the nuclear and electron spin qubits in each fridge via laser addressing, followed by a SWAP to each coupled transmon to transfer entanglement to the superconducting circuit. Computation can be carried out on an

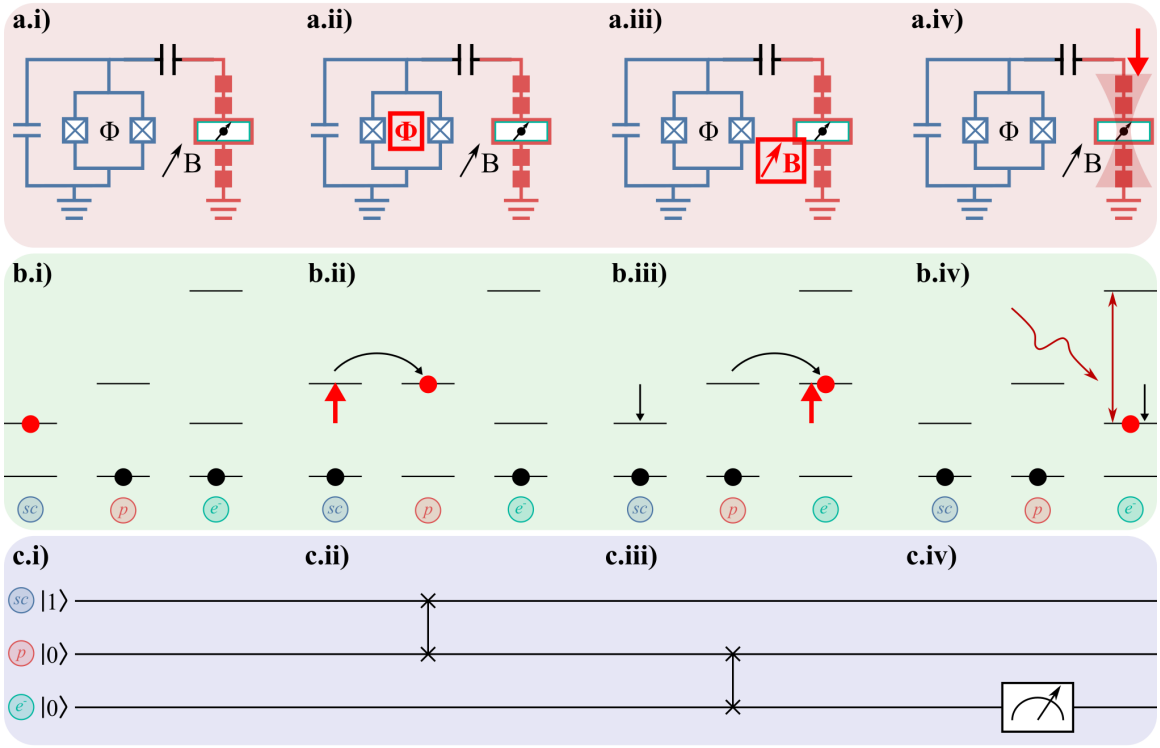

Figure 3-9: Transduction protocol for optical readout of the coupled system. (a) Diagram of the active control elements at each step, (b) energy level diagram charting the physical movement of an excitation through the tripartite-coupled system, and (c) equivalent quantum gates on the three qubits. (i) indicates an initialized state with the superconducting qubit in the excited state $|1\rangle$ and the phonon and electron spin initialized to the ground state $|0\rangle$. (ii) First SWAP operation initiated by tuning the superconducting circuit flux to be on resonance with the phonon mode for half a Rabi oscillation cycle. (iii) Second SWAP operation initiated by tuning the electron spin on resonance with the phonon mode via changing the external DC magnetic field. (iv) Laser addressing of the electron spin, which can be accomplished using a free space microscope or other means, allowing for optical readout of the system [18].

arbitrarily sized superconducting circuit to which each transmon is coupled (Fig. 3-10b). Finally, a SWAP gate can be implemented between the coupled transmons and each nuclear spin to store the excited state in each fridge (Fig. 3-10c). This proposal, when combined with that in Appendix C, provides a network interface and memory bank to superconducting quantum circuits.

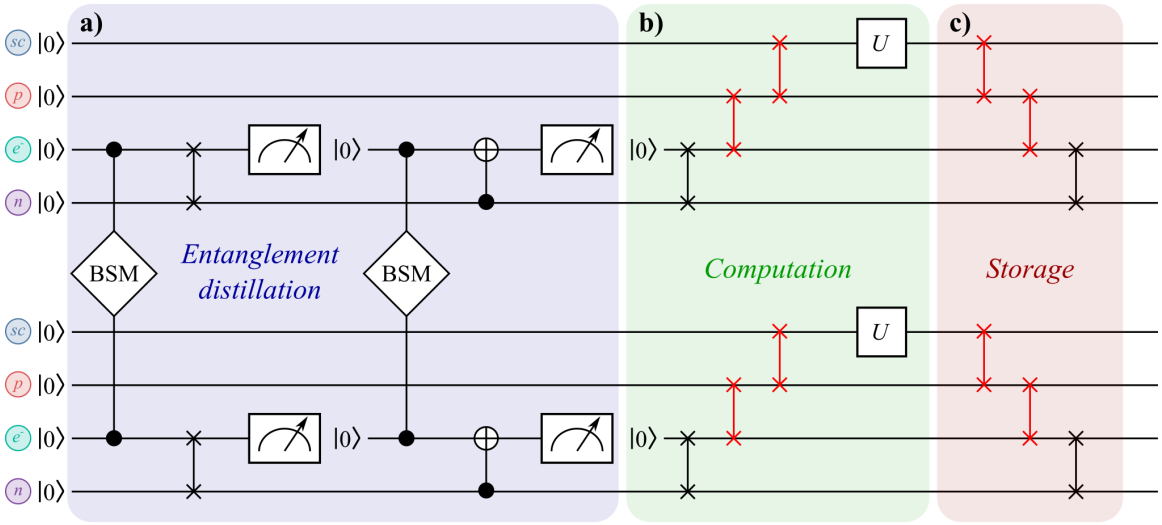

Figure 3-10: Implementing the transducer in a quantum entanglement and computation protocol. (a) Entanglement distillation using a coupled ^{13}C nuclear spin [64]. Here, "BSM" indicates a Bell-state measurement, the cross symbol represents a SWAP gate, the arrow represents a measurement operation, and the white-and-black dot symbol represents a CNOT operation. (b) Use of SWAP gates to conduct computational operations using the superconducting qubit and any other superconducting qubits interacting with the one in the schematic (not shown). Here, our transducer would be used to implement the otherwise missing SWAP gates, shown in red. The U operation represents an arbitrary computation carried out with the superconducting qubit. (c) Information storage in a coupled ^{13}C coupled nuclear spin, where our transducer would again be used to implement the otherwise missing SWAP gates (shown in red).

Chapter 4

Outlook

In this work, we have outlined the design and implementation of two acoustic interfaces with quantum emitters in diamond. First, we discussed the use of optomechanics to couple flying photons from a quantum network to Group IV vacancies in diamond independent of their optical transitions. This spin-optomechanical interface leverages a central taper to feature ultrasmall optical and mechanical mode volumes, driving up the spin-phonon coupling to levels where single emitter-phonon interactions are viable. We discuss the deployment of this spin-optomechanical interface in heralded entanglement protocols for quantum networking.

Next, we discuss the design, simulation, and applications of an spin-embedded electromechanical transducer that generates strong superconducting circuit-to-phonon and phonon-to-spin coupling. We motivate our transducer design with FEM simulations and discuss its use in single quantum transduction from a superconducting transmon to a SiV^- electron spin. Finally, we propose a physical architecture for parallelizing spin memories to a single transmon using an array of spin-electromechanical transducers as well as computing protocols that leverage our transducer for entanglement distillation and computing with spin memories.

Several steps are required before ultimately achieving spin-phonon coupling in our proposed spin-optomechanical cavities or spin-electromechanical transducers. We delineate these steps below.

1. Cryogenic operation of Group IV centers.

2. Fabrication and ambient characterization of optomechanical (electromechanical) resonators.

3. Heterogeneous integration of diamond optomechanical (thin film patterned) structures with embedded spins in on-chip architectures.

4. Cryogenic characterization of optomechanical (electromechanical) resonators.

5. Implementation of transduction protocols in cryogenic environments.

We report our experimental progress on these steps in the following sections.

4.1 Cryogenic Operation of Quantum Emitters

Silicon vacancy centers in diamond must be operated at millikelvin temperatures in order to have sufficiently narrow bandwidth spin transitions for quantum spin control [145]. As such, spin-mechanical devices must also operate in this regime. However, tin vacancy (SnV^-) centers, which have an analogous structure to the SiV^- center, can operate at temperatures as high as 1 Kelvin. This is due to the fact that the spin-orbit splitting between ground and excited spin manifolds is around 850 GHz as opposed to the 46 GHz splitting of strain-free SiV^- centers [56, 148]. Because the Boltzmann phonon occupancy of 850 GHz modes in bulk diamond are around 2×10^{-17} times lower than that of 46 GHz phonons at a 1 K, SnV^- spin transition linewidths are sufficiently narrow at 1 K for quantum information protocols.

We demonstrate the initial detection and characterization of SnV^- centers in diamond microchiplets below. Diamond microchiplets, which have also been used in other heterogeneous integration studies involving NV^- and SiV^- centers [151, 108], were fabricated in electronic grade diamond procured from Element Six using a quasi-isotropic etch [109]. Microchiplets were placed in a Montana CryoCore cryostation operating with a base stage temperature of 4.2 K. A 515 nm Cobolt green laser was

used to excite SnV^- centers via free-space addressing, and a M Squared laser operating at approximately 619 nm with a spectral range of 30 GHz was used to resonantly excite the SnV^- optical transition. This allowed for photoluminescence excitation (PLE) of SnV^- centers at 4 K. A wide-field lens was used to simultaneously conduct PLE on all emitters within a $\sim$30 GHz range from 484.118 THz to 484.147 THz (Fig. 4-1).

PLE of SnV^- at 4 K represents the first step of characterizing Group IV emitters for heterogeneous integration at cryogenic temperatures. An ICE Oxford AttoDry cryostat will be used to operate the spin transition of SnV^- centers in these pre-characterized microchiplets at a sample temperature of 1.3 K, at which the spin energy levels of SnV^- centers become distinguishable.

4.2 Towards Fabrication of Spin-Optomechanical Interfaces

Nanoscale photonic crystals have been demonstrated in diamond using a quasi-isotropic etch [109]. However, this fabrication is limited for one-dimensional nanobeams and long membranes that approach widths of 1 μm since the underside of the resonator is not flat, limiting the achievable quality factors of fabricated cavities and preventing the flat placement of heterogeneously integrated nanobeams on-chip. The main limitation preventing a longer etch to achieve a flat membrane is the selectivity of ZEP 520A hard masks used in the anisotropic etch step (Fig. 4-2a.ii); for longer etches, the hard mask protecting the nanobeam surface degrades.

To compensate for this limitation, we have pursued a quasi-isotropic etch with a 220 nm silicon hard mask fabricated by Applied Nanotools, Inc (ANT). The diamond:Si selectivity is expected to be higher than that of Si:ZEP 520A, allowing us to etch quasi-isotropically for longer and smooth the nanobeam underside. This concept is illustrated in Fig. 4-2b.i-vii.

Fig. 4-3 displays the ANT hard masks for 1D diamond spin-optomechanical in-

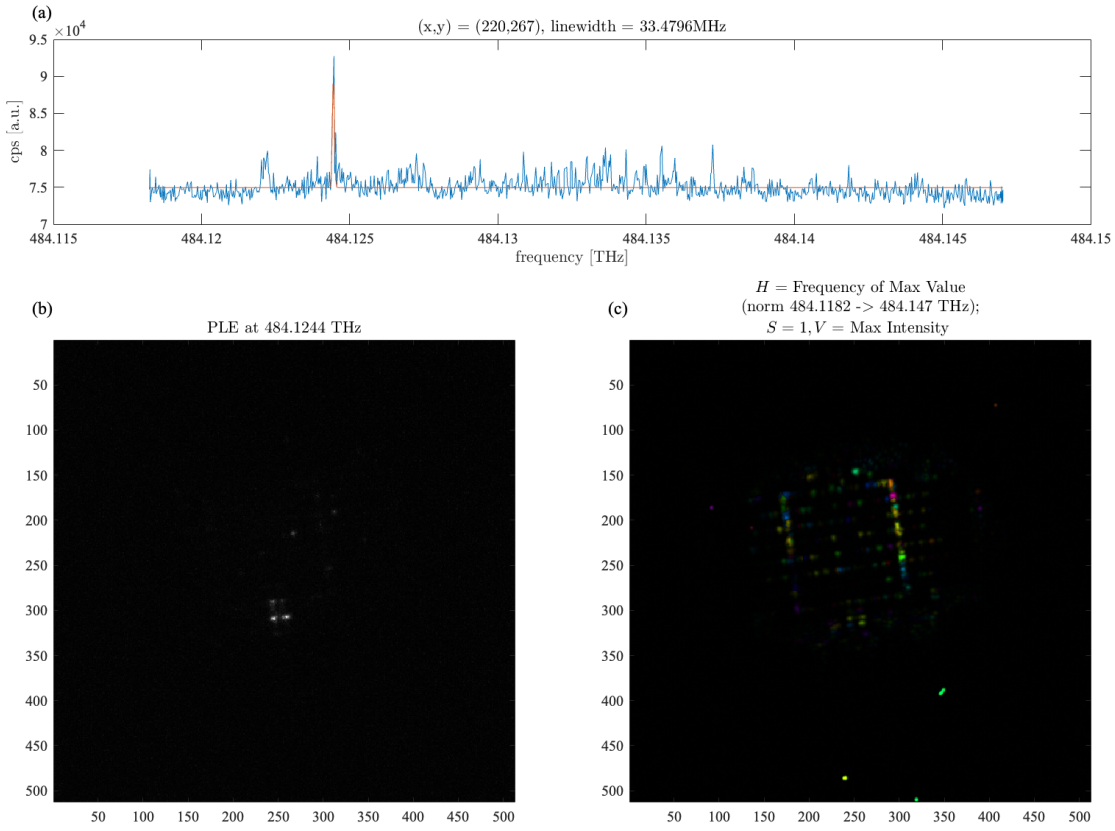

Figure 4-1: Interactive interface for microchiplet wide field PLE analysis, written with collaborators in MATLAB (see Acknowledgments). (a) Depicts the PLE spectrum around a single emitter in the microchiplet depicted in (b) and (c). (b) depicts the PLE scan at the emitter's resonant frequency. (c) HSV plot of all emitters in the microchiplet, where H is the frequency of the maximum value in the wide field scan (in this case, 484.147 THz), S is saturated at 1, and V is the maximum emitter intensity in arbitrary units.

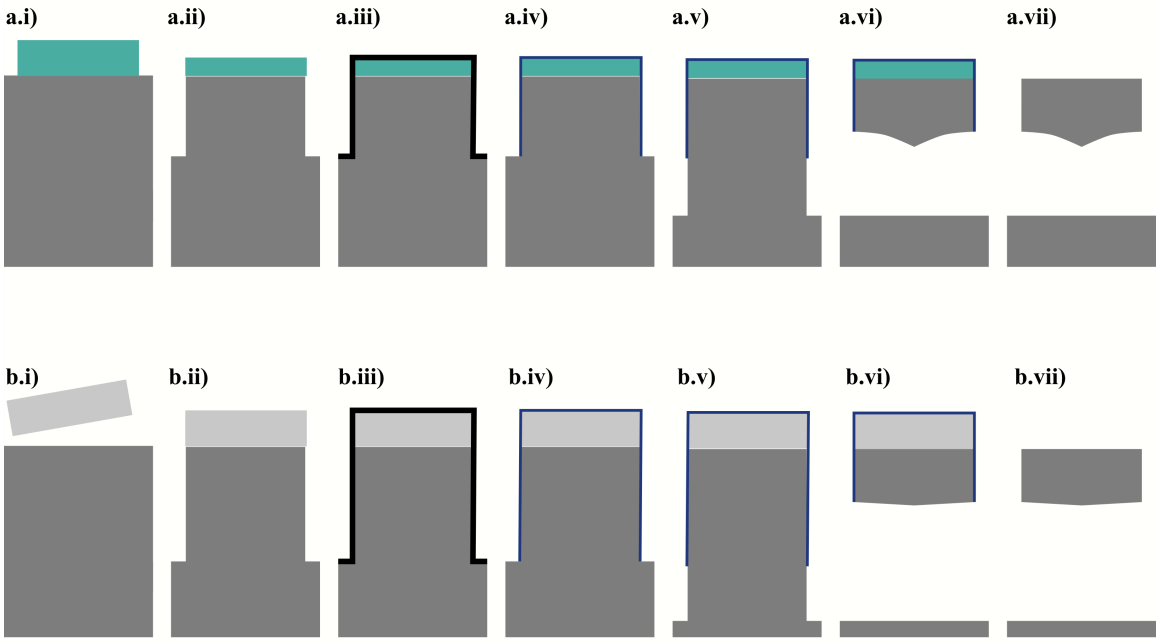

Figure 4-2: Conceptual comparison of diamond etch using (a) ZEP 520A and (b) Si hard masks. (i) Deposition of the hard mask (or in the case of Si, float-down placement). (ii) Anisotropic etching of the diamond. Conceptually, the Si hard mask degrades less due to higher selectivity, allowing for a deeper etch. (iii) Deposition of Al_2O_3. (iv) Selective removal of Al_2O_3 top layer. (v) Anisotropic etch of diamond. (vi) Quasi-isotropic plasma etch of nanobeam (in the case of a deeper anisotropic etch in (b), this quasi-isotropic etch can continue for a longer time, allowing for a smoother underside). (vi) Removal of hard mask.

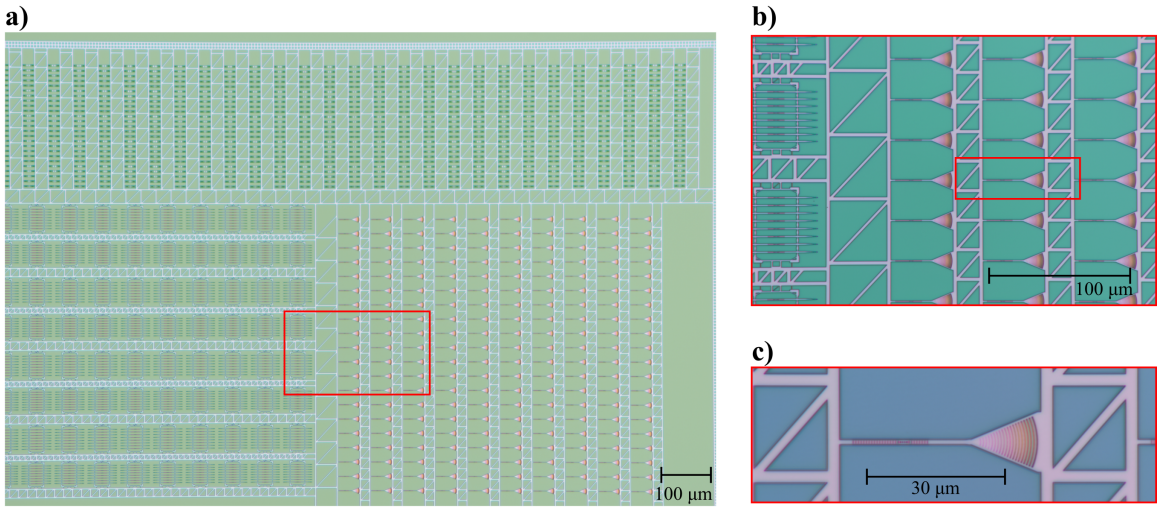

Figure 4-3: Silicon hard mask for diamond spin-optomechanical crystal interfaces from ANT. (a) image of the full mask including spin-optomechanical interfaces in a microchiplet frame (bottom left), individual nanobeams coupled to grating couplers (bottom right), and test structures for taper fabrication (top). (b) Close-up image of microchiplet and grating-coupled optomechanical crystals. (c) Hard mask image of a single nanobeam coupled to a grating coupler. Images were taken courtesy of collaborators (see Acknowledgements).

terfaces. We will proceed with diamond etching using these hard masks by floating down hard masks onto diamond substrates, followed by the etch recipe laid out in [109].

4.3 Towards Fabrication of Spin-Electromechanical Transducers

Our proposed spin-electromechanical transducer requires the deposition of thin film ScAlN as well as heterogeneous integration of diamond. We show the proposed device fabrication in Fig. 4-4. The bulk of the fabrication proposal follows that of a similar microwave photon-to-optical photon transducer [106] but features a modification accommodating the heterogeneous integration of a diamond thin film (Fig. 4-4e).

Currently, test structures for fabrication are being prepared at Sandia National Laboratories. Since the deposition of Nb electrodes requires further fabrication de-

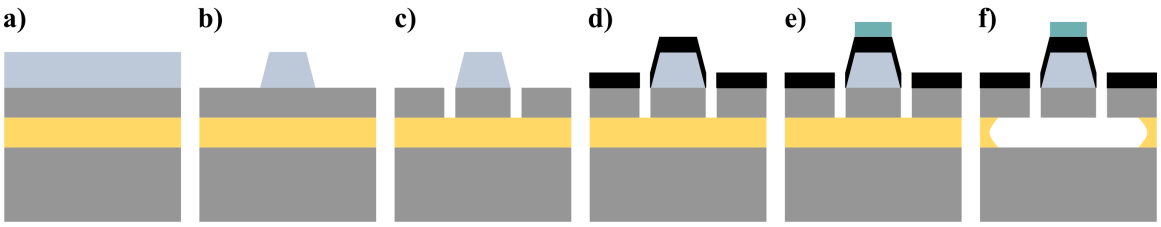

Figure 4-4: Proposed fabrication of spin-elecromechanical transducer with heterogeneously integrated diamond. (a) Deposition of thin film ScAlN on a silicon-on-insulator (SOI) substrate. (b) Dry anisotropic etching of the ScAlN layer to define the resonator box. (c) Plasma etching of the Si layer to pattern the resonator box Si layer and phononic tethers. (d) Evaporation of resonator electrodes. (e) Heterogeneous integration of diamond thin film on resonator box. (f) HF vapor etch of underlying oxide layer to release the resonator from the substrate. In these schematics, the light blue layer is ScAlN, the grey layers are Si, the yellow layer is SiO_2, the black layer defines the electrodes, and the turquoise layer is diamond.

velopment, early test samples are being prepared with Al for room temperature characterization and driving of Group IV spins.

4.4 Next Steps

As described above, we are pursuing the fabrication of spin-phonon interfaces (namely, spin-embedded optomechanical crystals and spin-embedded electromechanical transducers) and are operating Group IV vacancies in 4 K environments. Following these demonstrations, we aim to proceed with spectral characterization of our optomechanical crystals in an ambient environment; SiV^- implantation and recharacterization in a 10-50 mK dilution fridge; and demonstration of an optomechanically driven heralded entanglement protocol. We also aim to demonstrate coherent control and then quantum transduction using our electromechanical transducers at 10-50 mK.

We anticipate that the spin-phonon interfaces described in this work will find a myriad of applications in quantum networking and computing. We hope that these devices drive forward and motivate similar works in hybrid quantum information platforms that leverage the best of many quantum modalities to realize fully deployed quantum computers.

Bibliography

[1] Nitzan Akerman, Nir Navon, Shlomi Kotler, Yinnon Glickman, and Roee Ozeri. Universal gate-set for trapped-ion qubits using a narrow linewidth diode laser. *New Journal of Physics*, 17(11):113060, 2015.

[2] A. Akhiezer. On the absorption of sound in solids. *Journal of Physics (Moscow)*, 1:277–287, 1961.

[3] Morito Akiyama, Kazuhiko Kano, and Akihiko Teshigahara. Influence of growth temperature and scandium concentration on piezoelectric response of scandium aluminum nitride alloy thin films. *Applied Physics Letters*, 95(16):162107, 2009.

[4] Uzma Akram, Warwick P Bowen, and Gerard J Milburn. Entangled mechanical cat states via conditional single photon optomechanics. *New Journal of Physics*, 15(9):093007, 2013.

[5] Andreas Angerer, Kirill Streltsov, Thomas Astner, Stefan Putz, Hitoshi Sumiya, Shinobu Onoda, Junichi Isoya, William J Munro, Kae Nemoto, Jörg Schmiedmayer, et al. Superradiant emission from colour centres in diamond. *Nature Physics*, 14(12):1168–1172, 2018.

[6] Patricio Arrangoiz-Arriola and Amir H Safavi-Naeini. Engineering interactions between superconducting qubits and phononic nanostructures. *Physical Review A*, 94(6):063864, 2016.

[7] Patricio Arrangoiz-Arriola, Alex Wollack, Marek Pechal, Zhaoyou Wang, Wentao Jiang, Timothy McKenna, and Amir Safavi-Naeini. Strong coupling of a transmon qubit and a phononic crystal cavity array. In *APS March Meeting Abstracts*, volume 2019, pages S29–011, 2019.

[8] Patricio Arrangoiz-Arriola, E Alex Wollack, Marek Pechal, Jeremy D Witmer, Jeff T Hill, and Amir H Safavi-Naeini. Coupling a superconducting quantum circuit to a phononic crystal defect cavity. *Physical Review X*, 8(3):031007, 2018.

[9] Frank Arute, Kunal Arya, Ryan Babbush, Dave Bacon, Joseph C Bardin, Rami Barends, Sergio Boixo, Michael Broughton, Bob B Buckley, David A Buell, et al. Hartree-fock on a superconducting qubit quantum computer. *Science*, 369(6507):1084–1089, 2020.

[10] Arthur Ashkin. Trapping of atoms by resonance radiation pressure. *Physical Review Letters*, 40(12):729, 1978.

[11] Arthur Ashkin, James M Dziedzic, John E Bjorkholm, and Steven Chu. Observation of a single-beam gradient force optical trap for dielectric particles. *Optics letters*, 11(5):288–290, 1986.

[12] Markus Aspelmeyer, Tobias J Kippenberg, and Florian Marquardt. *Cavity optomechanics: nano-and micromechanical resonators interacting with light*. Springer, 2014.

[13] Nir Bar-Gill, Linh M Pham, Andrejs Jarmola, Dmitry Budker, and Ronald L Walsworth. Solid-state electronic spin coherence time approaching one second. *Nature communications*, 4(1):1–6, 2013.

[14] Saswati Barman and GP Srivastava. Temperature dependence of the thermal conductivity of different forms of diamond. *Journal of Applied Physics*, 101(12):123507, 2007.

[15] Jonas N. Becker, Benjamin Pingault, David Groß, Mustafa Gündoğan, Nadezhda Kukharchyk, Matthew Markham, Andrew Edmonds, Mete Atatüre, Pavel Bushev, and Christoph Becher. All-optical control of the silicon-vacancy spin in diamond at millikelvin temperatures. *Phys. Rev. Lett.*, 120:053603, Jan 2018.

[16] L. Bergeron, C. Chartrand, A. T. K. Kurkjian, K. J. Morse, H. Riemann, N. V. Abrosimov, P. Becker, H.-J. Pohl, M. L. W. Thewalt, and S. Simmons. Silicon-integrated telecommunications photon-spin interface. *PRX Quantum*, 1:020301, Oct 2020.

[17] R Berman, Franz Eugen Simon, and John Michael Ziman. The thermal conductivity of diamond at low temperatures. *Proceedings of the Royal Society of London. Series A. Mathematical and Physical Sciences*, 220(1141):171–183, 1953.

[18] Hannes Bernien, Bas Hensen, Wolfgang Pfaff, Gerwin Koolstra, Machiel S Blok, Lucio Robledo, TH Taminiau, Matthew Markham, Daniel J Twitchen, Lilian Childress, et al. Heralded entanglement between solid-state qubits separated by three metres. *Nature*, 497(7447):86–90, 2013.

[19] Mihir K Bhaskar, Ralf Riedinger, Bartholomeus Machielse, David S Levonian, Christian T Nguyen, Erik N Knall, Hongkun Park, Dirk Englund, Marko Lončar, Denis D Sukachev, et al. Experimental demonstration of memory-enhanced quantum communication. *Nature*, 580(7801):60–64, 2020.

[20] Johan Bjurström, Ilia Katardjiev, and Ventsislav Yantchev. Lateral-field-excited thin-film lamb wave resonator. *Applied Physics Letters*, 86(15):154103, 2005.

[21] Chris Brown, Arthur S. Morris, Angus I. Kingon, and Jacqueline Krim. Cryogenic performance of rf mems switch contacts. *Journal of Microelectromechanical Systems*, 17(6):1460–1467, 2008.

[22] Benjamin M Brubaker, Jonathan M Kindem, Maxwell D Urmey, Sarang Mittal, Robert D Delaney, Peter S Burns, Michael R Vissers, Konrad W Lehnert, and Cindy A Regal. Optomechanical ground-state cooling in a continuous and efficient electro-optic transducer. *Physical Review X*, 12(2):021062, 2022.

[23] Michael J Burek, Justin D Cohen, Seán M Meenehan, Nayera El-Sawah, Cleaven Chia, Thibaud Ruelle, Srujan Meesala, Jake Rochman, Haig A Atikian, Matthew Markham, et al. Diamond optomechanical crystals. *Optica*, 3(12):1404–1411, 2016.

[24] Jeffrey V Cady, Ohad Michel, Kenneth W Lee, Rishi N Patel, Christopher J Sarabalis, Amir H Safavi-Naeini, and Ania C Bleszynski Jayich. Diamond optomechanical crystals with embedded nitrogen-vacancy centers. *Quantum Science and Technology*, 4(2):024009, 2019.

[25] J.J. Campbell and W.R. Jones. A method for estimating optimal crystal cuts and propagation directions for excitation of piezoelectric surface waves. *IEEE Transactions on Sonics and Ultrasonics*, 15(4):209–217, 1968.

[26] S. G. Carter, Ö. O. Soykal, Pratibha Dev, Sophia E. Economou, and E. R. Glaser. Spin coherence and echo modulation of the silicon vacancy in $4h-$SiC at room temperature. *Phys. Rev. B*, 92:161202, Oct 2015.

[27] Jasper Chan. *Laser cooling of an optomechanical crystal resonator to its quantum ground state of motion*. California Institute of Technology, 2012.

[28] Jasper Chan, TP Mayer Alegre, Amir H Safavi-Naeini, Jeff T Hill, Alex Krause, Simon Gröblacher, Markus Aspelmeyer, and Oskar Painter. Laser cooling of a nanomechanical oscillator into its quantum ground state. *Nature*, 478(7367):89–92, 2011.

[29] Jasper Chan, Amir H Safavi-Naeini, Jeff T Hill, Seán Meenehan, and Oskar Painter. Optimized optomechanical crystal cavity with acoustic radiation shield. *Applied Physics Letters*, 101(8):081115, 2012.

[30] Lilian Isabel Childress. *Coherent manipulation of single quantum systems in the solid state*. Harvard University, 2007.

[31] Hyeongrak Choi, Mikkel Heuck, and Dirk Englund. Self-similar nanocavity design with ultrasmall mode volume for single-photon nonlinearities. *Phys. Rev. Lett.*, 118:223605, May 2017.

[32] Juan I Cirac and Peter Zoller. Quantum computations with cold trapped ions. *Physical review letters*, 74(20):4091, 1995.

[33] Robert Joseph Corruccini and John J Gniewek. *Specific Heats and Enthalpies of Technical Solids at Low Temperatures: A Compilation from the Literature*, volume 21. US Government Printing Office, 1960.

[34] BD Cuthbertson, ME Tobar, EN Ivanov, and DG Blair. Parametric back-action effects in a high-q cyrogenic sapphire transducer. *Review of Scientific Instruments*, 67(7):2435–2442, 1996.

[35] Gordon Davies. Vibronic spectra in diamond. *Journal of Physics C: Solid State Physics*, 7(20):3797, 1974.

[36] Romain Debroux, Cathryn P. Michaels, Carola M. Purser, Noel Wan, Matthew E. Trusheim, Jesús Arjona Martínez, Ryan A. Parker, Alexander M. Stramma, Kevin C. Chen, Lorenzo de Santis, Evgeny M. Alexeev, Andrea C. Ferrari, Dirk Englund, Dorian A. Gangloff, and Mete Atatüre. Quantum control of the tin-vacancy spin qubit in diamond. *Phys. Rev. X*, 11:041041, Nov 2021.

[37] Michel H Devoret and Robert J Schoelkopf. Superconducting circuits for quantum information: an outlook. *Science*, 339(6124):1169–1174, 2013.

[38] Gavin Dold, Christoph W Zollitsch, James O'sullivan, Sacha Welinski, Alban Ferrier, Philippe Goldner, SE de Graaf, Tobias Lindström, and John JL Morton. High-cooperativity coupling of a rare-earth spin ensemble to a superconducting resonator using yttrium orthosilicate as a substrate. *Physical Review Applied*, 11(5):054082, 2019.

[39] L-M Duan, Mikhail D Lukin, J Ignacio Cirac, and Peter Zoller. Long-distance quantum communication with atomic ensembles and linear optics. *Nature*, 414(6862):413–418, 2001.

[40] Amy Duwel, Rob N Candler, Thomas W Kenny, and Mathew Varghese. Engineering mems resonators with low thermoelastic damping. *Journal of microelectromechanical systems*, 15(6):1437–1445, 2006.

[41] Matt Eichenfield, Ryan Camacho, Jasper Chan, Kerry J Vahala, and Oskar Painter. A picogram-and nanometre-scale photonic-crystal optomechanical cavity. *nature*, 459(7246):550–555, 2009.

[42] Matt Eichenfield, Jasper Chan, Ryan M Camacho, Kerry J Vahala, and Oskar Painter. Optomechanical crystals. *Nature*, 462(7269):78–82, 2009.

[43] Linran Fan, Xiankai Sun, Chi Xiong, Carsten Schuck, and Hong X Tang. Aluminum nitride piezo-acousto-photonic crystal nanocavity with high quality factors. *Applied Physics Letters*, 102(15):153507, 2013.

[44] D. K. Finnemore, T. F. Stromberg, and C. A. Swenson. Superconducting properties of high-purity niobium. *Phys. Rev.*, 149:231–243, Sep 1966.

[45] Moritz Forsch, Robert Stockill, Andreas Wallucks, Igor Marinković, Claus Gärtner, Richard A Norte, Frank van Otten, Andrea Fiore, Kartik Srinivasan, and Simon Gröblacher. Microwave-to-optics conversion using a mechanical oscillator in its quantum ground state. *Nature Physics*, 16(1):69–74, 2020.

[46] Kai-Mei C Fu, Charles Santori, Paul E Barclay, Lachlan J Rogers, Neil B Manson, and Raymond G Beausoleil. Observation of the dynamic jahn-teller effect in the excited states of nitrogen-vacancy centers in diamond. *Physical Review Letters*, 103(25):256404, 2009.

[47] Shirin Ghaffari, Saurabh A Chandorkar, Shasha Wang, Eldwin J Ng, Chae H Ahn, Vu Hong, Yushi Yang, and Thomas W Kenny. Quantum limit of quality factor in silicon micro and nano mechanical resonators. *Scientific reports*, 3(1):1–7, 2013.

[48] Roohollah Ghobadi, Stephen Wein, Hamidreza Kaviani, Paul Barclay, and Christoph Simon. Progress toward cryogen-free spin-photon interfaces based on nitrogen-vacancy centers and optomechanics. *Physical Review A*, 99(5):053825, 2019.

[49] D Andrew Golter, Thein Oo, Mayra Amezcua, Ignas Lekavicius, Kevin A Stewart, and Hailin Wang. Coupling a surface acoustic wave to an electron spin in diamond via a dark state. *Physical Review X*, 6(4):041060, 2016.

[50] D Andrew Golter, Thein Oo, Mayra Amezcua, Kevin A Stewart, and Hailin Wang. Optomechanical quantum control of a nitrogen-vacancy center in diamond. *Physical review letters*, 116(14):143602, 2016.

[51] D Andrew Golter and Hailin Wang. Optically driven rabi oscillations and adiabatic passage of single electron spins in diamond. *Physical review letters*, 112(11):116403, 2014.

[52] JE Graebner and JA Herb. Dominance of intrinsic phonon scattering. *Diamond Films and Technology*, 1(3), 1992.

[53] Cécile Grezes, Yuimaru Kubo, Brian Julsgaard, Takahide Umeda, Junichi Isoya, Hitoshi Sumiya, Hiroshi Abe, Shinobu Onoda, Takeshi Ohshima, Kazuo Nakamura, et al. Towards a spin-ensemble quantum memory for superconducting qubits. *Comptes Rendus Physique*, 17(7):693–704, 2016.

[54] PC Haljan, PJ Lee, KA Brickman, M Acton, L Deslauriers, and C Monroe. Entanglement of trapped-ion clock states. *Physical Review A*, 72(6):062316, 2005.

[55] Connor T. Hann, Chang-Ling Zou, Yaxing Zhang, Yiwen Chu, Robert J. Schoelkopf, S. M. Girvin, and Liang Jiang. Hardware-efficient quantum random access memory with hybrid quantum acoustic systems. *Phys. Rev. Lett.*, 123:250501, Dec 2019.

[56] Christian Hepp, Tina Müller, Victor Waselowski, Jonas N Becker, Benjamin Pingault, Hadwig Sternschulte, Doris Steinmüller-Nethl, Adam Gali, Jeronimo R Maze, Mete Atatüre, et al. Electronic structure of the silicon vacancy color center in diamond. *Physical Review Letters*, 112(3):036405, 2014.

[57] Yi-Wen Hu, Yun-Feng Xiao, Yong-Chun Liu, and Qihuang Gong. Optomechanical sensing with on-chip microcavities. *Frontiers of Physics*, 8(5):475–490, 2013.

[58] A. Jarmola, V. M. Acosta, K. Jensen, S. Chemerisov, and D. Budker. Temperature- and magnetic-field-dependent longitudinal spin relaxation in nitrogen-vacancy ensembles in diamond. *Phys. Rev. Lett.*, 108:197601, May 2012.

[59] Jia-Wei Ji, Yu-Feng Wu, Stephen C Wein, Faezeh Kimiaee Asadi, Roohollah Ghobadi, and Christoph Simon. Proposal for room-temperature quantum repeaters with nitrogen-vacancy centers and optomechanics. *arXiv preprint arXiv:2012.06687*, 2020.

[60] Wentao Jiang, Christopher J Sarabalis, Yanni D Dahmani, Rishi N Patel, Felix M Mayor, Timothy P McKenna, Raphaël Van Laer, and Amir H Safavi-Naeini. Efficient bidirectional piezo-optomechanical transduction between microwave and optical frequency. *Nature communications*, 11(1):1–7, 2020.

[61] Graham Joe, Cleaven Chia, Michelle Chalupnik, Benjamin Pingault, Srujan Meesala, Eliza Cornell, Daniel Assumpcao, Bartholomeus Machielse, and Marko Lončar. Diamond phononic crystals with silicon-vacancy centers at cryogenic temperatures. In *CLEO: QELS_Fundamental Science*, pages FTh4M–1. Optical Society of America, 2021.

[62] Steven G Johnson, Mihai Ibanescu, MA Skorobogatiy, Ori Weisberg, JD Joannopoulos, and Yoel Fink. Perturbation theory for maxwell's equations with shifting material boundaries. *Physical review E*, 65(6):066611, 2002.

[63] Petar Jurcevic, Ali Javadi-Abhari, Lev S Bishop, Isaac Lauer, Daniela F Bogorin, Markus Brink, Lauren Capelluto, Oktay Günlük, Toshinari Itoko, Naoki Kanazawa, et al. Demonstration of quantum volume 64 on a superconducting quantum computing system. *Quantum Science and Technology*, 6(2):025020, 2021.

[64] Norbert Kalb, Andreas A Reiserer, Peter C Humphreys, Jacob JW Bakermans, Sten J Kamerling, Naomi H Nickerson, Simon C Benjamin, Daniel J Twitchen, Matthew Markham, and Ronald Hanson. Entanglement distillation between solid-state quantum network nodes. *Science*, 356(6341):928–932, 2017.

[65] Adam M Kaufman, Brian J Lester, and Cindy A Regal. Cooling a single atom in an optical tweezer to its quantum ground state. *Physical Review X*, 2(4):041014, 2012.

[66] Andrew J Keller, Paul B Dieterle, Michael Fang, Brett Berger, Johannes M Fink, and Oskar Painter. Al transmon qubits on silicon-on-insulator for quantum device integration. *Applied Physics Letters*, 111(4):042603, 2017.

[67] Andrew J Keller, Paul B Dieterle, Michael Fang, Brett Berger, Johannes M Fink, and Oskar Painter. Superconducting qubits on silicon substrates for quantum device integration. *arXiv preprint arXiv:1703.10195*, 2017.

[68] Johannes Kepler. *De cometis libelli tres*. Typis Andre Apergeri, sumptibus Sebastiani Mylii, bibliopol Augustani, 1619.

[69] H. R. Kerchner, D. K. Christen, and S. T. Sekula. Critical fields H_c and H_{c2} of superconducting niobium. *Phys. Rev. B*, 24:1200–1204, Aug 1981.

[70] A.Yu. Kitaev. Fault-tolerant quantum computation by anyons. *Annals of Physics*, 303(1):2–30, 2003.

[71] Morten Kjaergaard, Mollie E Schwartz, Jochen Braumüller, Philip Krantz, Joel I-J Wang, Simon Gustavsson, and William D Oliver. Superconducting qubits: Current state of play. *Annual Review of Condensed Matter Physics*, 11:369–395, 2020.

[72] Takashi Kobayashi, Joseph Salfi, Cassandra Chua, Joost van der Heijden, Matthew G House, Dimitrie Culcer, Wayne D Hutchison, Brett C Johnson, Jeff C McCallum, Helge Riemann, et al. Engineering long spin coherence times of spin–orbit qubits in silicon. *Nature Materials*, 20(1):38–42, 2021.

[73] Akira Konno, Masahiro Sumisaka, Akihiko Teshigahara, Kazuhiko Kano, Kenya Hashimo, Hideki Hirano, Masayoshi Esashi, Michio Kadota, and Shuji Tanaka. Scaln lamb wave resonator in ghz range released by xef 2 etching. In *2013 IEEE International Ultrasonics Symposium (IUS)*, pages 1378–1381. IEEE, 2013.

[74] Philip Krantz, Morten Kjaergaard, Fei Yan, Terry P Orlando, Simon Gustavsson, and William D Oliver. A quantum engineer's guide to superconducting qubits. *Applied Physics Reviews*, 6(2):021318, 2019.

[75] Stefan Krastanov. Optomechanics two-mode squeezing and single phonon heralding, January 2022.

[76] Stefan Krastanov, Hamza Raniwala, Jeffrey Holzgrafe, Kurt Jacobs, Marko Lončar, Matthew J Reagor, and Dirk R Englund. Optically heralded entanglement of superconducting systems in quantum networks. *Physical Review Letters*, 127(4):040503, 2021.

[77] Stefan Krastanov, Hamza Raniwala, Jeffrey Holzgrafe, Kurt Jacobs, Marko Lončar, Matthew J. Reagor, and Dirk R. Englund. Optically-heralded entanglement of superconducting systems in quantum networks, 2021.

[78] Yuimaru Kubo, Cecile Grezes, Andreas Dewes, T Umeda, Junichi Isoya, H Sumiya, N Morishita, H Abe, S Onoda, T Ohshima, et al. Hybrid quantum circuit with a superconducting qubit coupled to a spin ensemble. *Physical review letters*, 107(22):220501, 2011.

[79] K Kunal and NR Aluru. Akhiezer damping in nanostructures. *Physical Review B*, 84(24):245450, 2011.

[80] Nicolas Kurz, Anli Ding, Daniel F Urban, Yuan Lu, Lutz Kirste, Niclas M Feil, Agnė Žukauskaitė, and Oliver Ambacher. Experimental determination of the electro-acoustic properties of thin film alscn using surface acoustic wave resonators. *Journal of Applied Physics*, 126(7):075106, 2019.

[81] Mark C Kuzyk and Hailin Wang. Scaling phononic quantum networks of solid-state spins with closed mechanical subsystems. *Physical Review X*, 8(4):041027, 2018.

[82] L. D. Landau and Y. B. Rumer. Absorption of sound in solids. *Phys. Z. Sowjetunion*, 11, 1937.

[83] AR Lang. The strain-optical constants of diamond: A brief history of measurements. *Diamond and related materials*, 18(1):1–5, 2009.

[84] Dietrich Leibfried, Brian DeMarco, Volker Meyer, David Lucas, Murray Barrett, Joe Britton, Wayne M Itano, B Jelenković, Chris Langer, Till Rosenband, et al. Experimental demonstration of a robust, high-fidelity geometric two ion-qubit phase gate. *Nature*, 422(6930):412–415, 2003.

[85] Ignas Lekavicius, Thein Oo, and Hailin Wang. Diamond lamb wave spin-mechanical resonators with optically coherent nitrogen vacancy centers. *Journal of Applied Physics*, 126(21):214301, 2019.

[86] Bei-Bei Li, Lingfeng Ou, Yuechen Lei, and Yong-Chun Liu. Cavity optomechanical sensing. *Nanophotonics*, 10(11):2799–2832, 2021.

[87] Xinzhu Li, Mark C Kuzyk, and Hailin Wang. Honeycomblike phononic networks of spins with closed mechanical subsystems. *Physical Review Applied*, 11(6):064037, 2019.

[88] Chih-Ming Lin, Ting-Ta Yen, Yun-Ju Lai, Valery V Felmetsger, Matthew A Hopcroft, Jan H Kuypers, and Albert P Pisano. Temperature-compensated aluminum nitride lamb wave resonators. *IEEE transactions on ultrasonics, ferroelectrics, and frequency control*, 57(3):524–532, 2010.

[89] HP Löbl, M Klee, R Milsom, R Dekker, C Metzmacher, W Brand, and P Lok. Materials for bulk acoustic wave (baw) resonators and filters. *Journal of the European Ceramic Society*, 21(15):2633–2640, 2001.

[90] HP Loebl, M Klee, C Metzmacher, W Brand, R Milsom, and P Lok. Piezoelectric thin aln films for bulk acoustic wave (baw) resonators. *Materials Chemistry and Physics*, 79(2-3):143–146, 2003.

[91] Xiyuan Lu, Jonathan Y Lee, and Qiang Lin. High-frequency and high-quality silicon carbide optomechanical microresonators. *Scientific reports*, 5(1):1–9, 2015.

[92] Xiyuan Lu, Jonathan Y Lee, and Qiang Lin. Silicon carbide zipper photonic crystal optomechanical cavities. *Applied physics letters*, 116(22):221104, 2020.

[93] Xiyuan Lu, Jonathan Y Lee, Steven D Rogers, and Qiang Lin. Silicon carbide double-microdisk resonator. *Optics letters*, 44(17):4295–4298, 2019.

[94] Smarak Maity, Benjamin Pingault, Graham Joe, Michelle Chalupnik, Daniel Assumpção, Eliza Cornell, Linbo Shao, and Marko Lončar. Coherent coupling of mechanics to a single nuclear spin. *arXiv preprint arXiv:2107.10961*, 2021.

[95] Smarak Maity, Linbo Shao, Stefan Bogdanović, Srujan Meesala, Young-Ik Sohn, Neil Sinclair, Benjamin Pingault, Michelle Chalupnik, Cleaven Chia, Lu Zheng, et al. Coherent acoustic control of a single silicon vacancy spin in diamond. *Nature communications*, 11(1):1–6, 2020.

[96] Riccardo Manenti, Anton F Kockum, Andrew Patterson, Tanja Behrle, Joseph Rahamim, Giovanna Tancredi, Franco Nori, and Peter J Leek. Circuit quantum acoustodynamics with surface acoustic waves. *Nature communications*, 8(1):1–6, 2017.

[97] Humphrey J Maris. Interaction of sound waves with thermal phonons in dielectric crystals. In *Physical Acoustics*, volume 8, pages 279–345. Elsevier, 1971.

[98] Michael J Martin, Yuan-Yu Jau, Jongmin Lee, Anupam Mitra, Ivan H Deutsch, and Grant W Biedermann. A mølmer-sørensen gate with rydberg-dressed atoms. *arXiv e-prints*, pages arXiv–2111, 2021.

[99] David C. McKay, Stefan Filipp, Antonio Mezzacapo, Easwar Magesan, Jerry M. Chow, and Jay M. Gambetta. Universal gate for fixed-frequency qubits via a tunable bus. *Phys. Rev. Applied*, 6:064007, Dec 2016.

[100] Corey Rae Harrington McRae, Haozhi Wang, Jiansong Gao, Michael R Vissers, Teresa Brecht, Andrew Dunsworth, David P Pappas, and Josh Mutus. Materials loss measurements using superconducting microwave resonators. *Review of Scientific Instruments*, 91(9):091101, 2020.

[101] Srujan Meesala, Young-Ik Sohn, Haig A Atikian, Samuel Kim, Michael J Burek, Jennifer T Choy, and Marko Lončar. Enhanced strain coupling of nitrogen-vacancy spins to nanoscale diamond cantilevers. *Physical Review Applied*, 5(3):034010, 2016.

[102] Srujan Meesala, Young-Ik Sohn, Benjamin Pingault, Linbo Shao, Haig A Atikian, Jeffrey Holzgrafe, Mustafa Gündoğan, Camille Stavrakas, Alp Sipahigil, Cleaven Chia, et al. Strain engineering of the silicon-vacancy center in diamond. *Physical Review B*, 97(20):205444, 2018.

[103] Alexander Melville, Greg Calusine, Wayne Woods, Kyle Serniak, Evan Golden, Bethany M Niedzielski, David K Kim, Arjan Sevi, Jonilyn L Yoder, Eric A Dauler, et al. Comparison of dielectric loss in titanium nitride and aluminum superconducting resonators. *Applied Physics Letters*, 117(12):124004, 2020.

[104] Mathias H. Metsch, Katharina Senkalla, Benedikt Tratzmiller, Jochen Scheuer, Michael Kern, Jocelyn Achard, Alexandre Tallaire, Martin B. Plenio, Petr Siyushev, and Fedor Jelezko. Initialization and readout of nuclear spins via a negatively charged silicon-vacancy center in diamond. *Phys. Rev. Lett.*, 122:190503, May 2019.

[105] Mohammad Mirhosseini, Alp Sipahigil, Mahmoud Kalaee, and Oskar Painter. Quantum transduction of optical photons from a superconducting qubit. *arXiv preprint arXiv:2004.04838*, 2020.

[106] Mohammad Mirhosseini, Alp Sipahigil, Mahmoud Kalaee, and Oskar Painter. Superconducting qubit to optical photon transduction. *Nature*, 588(7839):599–603, 2020.

[107] Anupam Mitra, Michael J Martin, Grant W Biedermann, Alberto M Marino, Pablo M Poggi, and Ivan H Deutsch. Robust mølmer-sørensen gate for neutral atoms using rapid adiabatic rydberg dressing. *Physical Review A*, 101(3):030301, 2020.

[108] Sara Mouradian, Tim Schröder, Carl Poitras, Luozhou Li, Jamie Cardenas, Jordan Goldstein, Rishi Patel, Edward Chen, Matthew Trusheim, Igal Bayn, et al. Efficient integration of high-purity diamond nanostructures into silicon nitride photonic circuits. In *CLEO: QELS_ Fundamental Science*, pages FW1B–7. Optica Publishing Group, 2014.

[109] Sara Mouradian, Noel H Wan, Tim Schröder, and Dirk Englund. Rectangular photonic crystal nanobeam cavities in bulk diamond. *Applied Physics Letters*, 111(2):021103, 2017.

[110] Roland Nagy, Matthias Niethammer, Matthias Widmann, Yu-Chen Chen, Péter Udvarhelyi, Cristian Bonato, Jawad Ul Hassan, Robin Karhu, Ivan G Ivanov, Nguyen Tien Son, et al. High-fidelity spin and optical control of single silicon-vacancy centres in silicon carbide. *Nature communications*, 10(1):1–8, 2019.

[111] Tomas Neuman, Matt Eichenfield, Matthew Trusheim, Lisa Hackett, Prineha Narang, and Dirk Englund. A phononic bus for coherent interfaces between a superconducting quantum processor, spin memory, and photonic quantum networks. *arXiv preprint arXiv:2003.08383*, 2020.

[112] Aaron D O'Connell, Max Hofheinz, Markus Ansmann, Radoslaw C Bialczak, Mike Lenander, Erik Lucero, Matthew Neeley, Daniel Sank, H Wang, Ms Weides, et al. Quantum ground state and single-phonon control of a mechanical resonator. *Nature*, 464(7289):697–703, 2010.

[113] Lawrence S Pan and Don R Kania. *Diamond: Electronic Properties and Applications: Electronic Properties and Applications*, volume 294. Springer Science & Business Media, 1994.

[114] Marek Pechal, Patricio Arrangoiz-Arriola, and Amir H Safavi-Naeini. Superconducting circuit quantum computing with nanomechanical resonators as storage. *Quantum Science and Technology*, 4(1):015006, 2018.

[115] GA Peterson, S Kotler, F Lecocq, K Cicak, XY Jin, RW Simmonds, J Aumentado, and JD Teufel. Ultrastrong parametric coupling between a superconducting cavity and a mechanical resonator. *Physical review letters*, 123(24):247701, 2019.

[116] Benjamin Pingault, David-Dominik Jarausch, Christian Hepp, Lina Klintberg, Jonas N Becker, Matthew Markham, Christoph Becher, and Mete Atatüre. Coherent control of the silicon-vacancy spin in diamond. *Nature communications*, 8(1):1–7, 2017.

[117] Jarryd J Pla, Kuan Y Tan, Juan P Dehollain, Wee H Lim, John JL Morton, Floris A Zwanenburg, David N Jamieson, Andrew S Dzurak, and Andrea Morello. High-fidelity readout and control of a nuclear spin qubit in silicon. *Nature*, 496(7445):334–338, 2013.

[118] Taras Plakhotnik, Marcus W Doherty, and Neil B Manson. Electron-phonon processes of the nitrogen-vacancy center in diamond. *Physical Review B*, 92(8):081203, 2015.

[119] RO Pohl. The applicability of the debye model to thermal conductivity. *Zeitschrift für Physik*, 176(4):358–369, 1963.

[120] Anjali Premkumar, Conan Weiland, Sooyeon Hwang, Berthold Jäck, Alexander PM Place, Iradwikanari Waluyo, Adrian Hunt, Valentina Bisogni, Jonathan Pelliciari, Andi Barbour, et al. Microscopic relaxation channels in materials for superconducting qubits. *Communications Materials*, 2(1):1–9, 2021.

[121] Peter Rabl, P Cappellaro, MV Gurudev Dutt, Liang Jiang, JR Maze, and Mikhail D Lukin. Strong magnetic coupling between an electronic spin qubit and a mechanical resonator. *Physical Review B*, 79(4):041302, 2009.

[122] Peter Rabl, Shimon Jacob Kolkowitz, FHL Koppens, JGE Harris, P Zoller, and Mikhail D Lukin. A quantum spin transducer based on nanoelectromechanical resonator arrays. *Nature Physics*, 6(8):602–608, 2010.

[123] Hamza Raniwala, Stefan Krastanov, Matt Eichenfield, and Dirk Englund. A spin-optomechanical quantum interface enabled by an ultrasmall mechanical and optical mode volume cavity. *arXiv preprint arXiv:2202.06999*, 2022.

[124] V Ranjan, G De Lange, R Schutjens, T Debelhoir, JP Groen, D Szombati, DJ Thoen, TM Klapwijk, Ronald Hanson, and L DiCarlo. Probing dynamics of an electron-spin ensemble via a superconducting resonator. *Physical review letters*, 110(6):067004, 2013.

[125] Robert Raussendorf, Jim Harrington, and Kovid Goyal. Topological fault-tolerance in cluster state quantum computation. *New Journal of Physics*, 9(6):199, 2007.

[126] Lord Rayleigh. On waves propagated along the plane surface of an elastic solid. *Proceedings of the London mathematical Society*, 1(1):4–11, 1885.

[127] Robert R Reeber and Kai Wang. Thermal expansion, molar volume and specific heat of diamond from 0 to 3000k. *Journal of Electronic Materials*, 25(1):63–67, 1996.

[128] Hengjiang Ren, Matthew H Matheny, Gregory S MacCabe, Jie Luo, Hannes Pfeifer, Mohammad Mirhosseini, and Oskar Painter. Two-dimensional optomechanical crystal cavity with high quantum cooperativity. *Nature communications*, 11(1):1–10, 2020.

[129] Ralf Riedinger, Andreas Wallucks, Igor Marinković, Clemens Löschnauer, Markus Aspelmeyer, Sungkun Hong, and Simon Gröblacher. Remote quantum entanglement between two micromechanical oscillators. *Nature*, 556(7702):473–477, 2018.

[130] Lachlan J. Rogers, Kay D. Jahnke, Mathias H. Metsch, Alp Sipahigil, Jan M. Binder, Tokuyuki Teraji, Hitoshi Sumiya, Junichi Isoya, Mikhail D. Lukin, Philip Hemmer, and Fedor Jelezko. All-optical initialization, readout, and coherent preparation of single silicon-vacancy spins in diamond. *Phys. Rev. Lett.*, 113:263602, Dec 2014.

[131] Rusko Ruskov and Charles Tahan. On-chip cavity quantum phonodynamics with an acceptor qubit in silicon. *Phys. Rev. B*, 88:064308, Aug 2013.

[132] Amir H Safavi-Naeini and Oskar Painter. Optomechanical crystal devices. In *Cavity Optomechanics*, pages 195–231. Springer, 2014.

[133] Kenji Saito et al. Critical field limitation of the niobium superconducting rf cavity. In *Proceedings of the 10th International Conference on RF Superconductivity, Tsukuba, Japan*, 2001.

[134] Mikołaj K Schmidt, Christopher G Poulton, and Michael J Steel. Acoustic diamond resonators with ultrasmall mode volumes. *Physical Review Research*, 2(3):033153, 2020.

[135] M. J. A. Schuetz, E. M. Kessler, G. Giedke, L. M. K. Vandersypen, M. D. Lukin, and J. I. Cirac. Universal quantum transducers based on surface acoustic waves. *Phys. Rev. X*, 5:031031, Sep 2015.

[136] Prasoon K Shandilya, David P Lake, Matthew J Mitchell, Denis D Sukachev, and Paul E Barclay. Optomechanical interface between telecom photons and spin quantum memory, 2021.

[137] Yotam Shapira, Ravid Shaniv, Tom Manovitz, Nitzan Akerman, and Roee Ozeri. Robust entanglement gates for trapped-ion qubits. *Physical review letters*, 121(18):180502, 2018.

[138] Anthony J Sigillito, Hans Malissa, Alexei M Tyryshkin, Helge Riemann, Nikolai V Abrosimov, Peter Becker, H-J Pohl, Mike LW Thewalt, Kohei M Itoh, John JL Morton, et al. Fast, low-power manipulation of spin ensembles in superconducting microresonators. *Applied Physics Letters*, 104(22):222407, 2014.

[139] Mika A Sillanpää, Jae I Park, and Raymond W Simmonds. Coherent quantum state storage and transfer between two phase qubits via a resonant cavity. *Nature*, 449(7161):438–442, 2007.

[140] D. Simin, H. Kraus, A. Sperlich, T. Ohshima, G. V. Astakhov, and V. Dyakonov. Locking of electron spin coherence above 20 ms in natural silicon carbide. *Phys. Rev. B*, 95:161201, Apr 2017.

[141] Anders Sørensen and Klaus Mølmer. Quantum computation with ions in thermal motion. *Physical review letters*, 82(9):1971, 1999.

[142] Ö. O. Soykal, Rusko Ruskov, and Charles Tahan. Sound-based analogue of cavity quantum electrodynamics in silicon. *Phys. Rev. Lett.*, 107:235502, Nov 2011.

[143] M. Steiner, P. Neumann, J. Beck, F. Jelezko, and J. Wrachtrup. Universal enhancement of the optical readout fidelity of single electron spins at nitrogen-vacancy centers in diamond. *Phys. Rev. B*, 81:035205, Jan 2010.

[144] J. D. Strand, Matthew Ware, Félix Beaudoin, T. A. Ohki, B. R. Johnson, Alexandre Blais, and B. L. T. Plourde. First-order sideband transitions with flux-driven asymmetric transmon qubits. *Phys. Rev. B*, 87:220505, Jun 2013.

[145] D. D. Sukachev, A. Sipahigil, C. T. Nguyen, M. K. Bhaskar, R. E. Evans, F. Jelezko, and M. D. Lukin. Silicon-vacancy spin qubit in diamond: A quantum memory exceeding 10 ms with single-shot state readout. *Phys. Rev. Lett.*, 119:223602, Nov 2017.

[146] R. Tabrizian, M. Rais-Zadeh, and F. Ayazi. Effect of phonon interactions on limiting the f.q product of micromechanical resonators. In *TRANSDUCERS 2009 - 2009 International Solid-State Sensors, Actuators and Microsystems Conference*, pages 2131–2134, 2009.

[147] Diamond Materials: Advanced Diamond Technology. *The CVD diamond booklet*. Diamond Materials: Advanced Diamond Technology, 2021.

[148] Matthew E Trusheim, Benjamin Pingault, Noel H Wan, Mustafa Gündoğan, Lorenzo De Santis, Romain Debroux, Dorian Gangloff, Carola Purser, Kevin C Chen, Michael Walsh, et al. Transform-limited photons from a coherent tin-vacancy spin in diamond. *Physical review letters*, 124(2):023602, 2020.

[149] A. M. Tyryshkin, S. A. Lyon, A. V. Astashkin, and A. M. Raitsimring. Electron spin relaxation times of phosphorus donors in silicon. *Phys. Rev. B*, 68:193207, Nov 2003.

[150] Amit Vainsencher, KJ Satzinger, GA Peairs, and AN Cleland. Bi-directional conversion between microwave and optical frequencies in a piezoelectric optomechanical device. *Applied Physics Letters*, 109(3):033107, 2016.

[151] Noel H Wan, Tsung-Ju Lu, Kevin C Chen, Michael P Walsh, Matthew E Trusheim, Lorenzo De Santis, Eric A Bersin, Isaac B Harris, Sara L Mouradian, Ian R Christen, et al. Large-scale integration of artificial atoms in hybrid photonic circuits. *Nature*, 583(7815):226–231, 2020.

[152] D. S. Wang, A. G. Fowler, A. M. Stephens, and L. C. L. Hollenberg. Threshold error rates for the toric and surface codes, 2009.

[153] Hailin Wang and Ignas Lekavicius. Coupling spins to nanomechanical resonators: Toward quantum spin-mechanics. *Applied Physics Letters*, 117(23):230501, 2020.

[154] David S Weiss and Mark Saffman. Quantum computing with neutral atoms. *Physics Today*, 70(7), 2017.

[155] Samuel J Whiteley, Gary Wolfowicz, Christopher P Anderson, Alexandre Bourassa, He Ma, Meng Ye, Gerwin Koolstra, Kevin J Satzinger, Martin V Holt, F Joseph Heremans, et al. Spin–phonon interactions in silicon carbide addressed by gaussian acoustics. *Nature Physics*, 15(5):490–495, 2019.

[156] Ignacio Wilson-Rae, Nima Nooshi, W Zwerger, and Tobias J Kippenberg. Theory of ground state cooling of a mechanical oscillator using dynamical backaction. *Physical Review Letters*, 99(9):093901, 2007.

[157] E. Alex Wollack, Agnetta Y. Cleland, Patricio Arrangoiz-Arriola, Timothy P. McKenna, Rachel G. Gruenke, Rishi N. Patel, Wentao Jiang, Christopher J. Sarabalis, and Amir H. Safavi-Naeini. Loss channels affecting lithium niobate phononic crystal resonators at cryogenic temperature. *Applied Physics Letters*, 118(12):123501, Mar 2021.

[158] E Alex Wollack, Agnetta Y Cleland, Rachel G Gruenke, Zhaoyou Wang, Patricio Arrangoiz-Arriola, and Amir H Safavi-Naeini. Quantum state preparation

and tomography of entangled mechanical resonators. *Nature*, 604(7906):463–467, 2022.

[159] T. O. Woodruff and H. Ehrenreich. Absorption of sound in insulators. *Phys. Rev.*, 123:1553–1559, Sep 1961.

[160] W. Woods, G. Calusine, A. Melville, A. Sevi, E. Golden, D.K. Kim, D. Rosenberg, J.L. Yoder, and W.D. Oliver. Determining interface dielectric losses in superconducting coplanar-waveguide resonators. *Phys. Rev. Applied*, 12:014012, Jul 2019.

[161] Marcelo Wu, Emil Zeuthen, Krishna Coimbatore Balram, and Kartik Srinivasan. Microwave-to-optical transduction using a mechanical supermode for coupling piezoelectric and optomechanical resonators. *Physical Review Applied*, 13(1):014027, 2020.

[162] Ze-Liang Xiang, Xin-You Lü, Tie-Fu Li, J. Q. You, and Franco Nori. Hybrid quantum circuit consisting of a superconducting flux qubit coupled to a spin ensemble and a transmission-line resonator. *Phys. Rev. B*, 87:144516, Apr 2013.

[163] Xin-Biao Xu, Weiting Wang, Luyan Sun, and Chang-Ling Zou. Hybrid superconducting-photonic-phononic chip for quantum information processing. *Chip*, page 100016, 2022.

[164] Kazuhiko Yamanouchi and Kimio Shibayama. Propagation and amplification of rayleigh waves and piezoelectric leaky surface waves in linbo3. *Journal of Applied Physics*, 43(3):856–862, 1972.

[165] Changchun Zhong, Xu Han, Hong X Tang, and Liang Jiang. Entanglement of microwave-optical modes in a strongly coupled electro-optomechanical system. *Physical Review A*, 101(3):032345, 2020.

[166] Xiaobo Zhu, Shiro Saito, Alexander Kemp, Kosuke Kakuyanagi, Shin-ichi Karimoto, Hayato Nakano, William J Munro, Yasuhiro Tokura, Mark S Everitt, Kae Nemoto, et al. Coherent coupling of a superconducting flux qubit to an electron spin ensemble in diamond. *Nature*, 478(7368):221–224, 2011.

[167] Chang-Ling Zou, Xu Han, Liang Jiang, and Hong X. Tang. Cavity piezomechanical strong coupling and frequency conversion on an aluminum nitride chip. *Phys. Rev. A*, 94:013812, Jul 2016.